Title
FCC Ti

Author
Traylor, Rachel Elizabeth

Publication Date
2017

Peer reviewed|Thesis/dissertation

FCC Ti

By

Rachel E. Traylor

A dissertation submitted in partial satisfaction of the

requirements for the degree of

Doctor of Philosophy

in

Engineering – Materials Science and Engineering

in the

Graduate Division

of the

University of California, Berkeley

Committee in charge:

Professor Andrew M. Minor, Chair
Professor Peter Hosemann
Professor Mark Asta

Fall 2017

Abstract

Investigation of FCC Ti in TEM Foils Formed Under Three Separate Conditions

by

Rachel E. Traylor

Doctor of Philosophy in Materials Science and Engineering

University of California, Berkeley

Professor Andrew M. Minor, Chair

A hexagonal-close packed (HCP) to face-centered cubic (FCC) phase transition has been observed in freestanding alpha-titanium thin foils under three separate conditions: Type I – upon focused ion beam (FIB) irradiation, Type II – during *in situ* heating in a transmission electron microscope (TEM), and Type III – during *in situ* TEM straining. FCC Ti has not been anticipated based on the equilibrium phase diagram, however, all FCC Ti phases were found to be stable after formation under ambient conditions. Investigations into the chemical nature of these anomalous FCC Ti phases have revealed that FIB-induced FCC Ti is actually a form of titanium hydride while thermally-induced is more closely related to oxygen contamination. Strain-induced FCC Ti is neither a hydride nor an oxide and readily undergoes FCC deformation twinning under an applied load. *In situ* TEM experimentation coupled with high-resolution nanobeam diffraction of titanium foils has suggested that this anomalous phase transformation is facilitated by HCP **a**-type dislocation ($\vec{\mathbf{b}}=1/3\langle 11\bar{2}0\rangle_{HCP}$) nucleation, dissociation into partials, and propagation. For different reasons (primarily due to hydrogen, oxygen, and aluminum solutes for the type I, II, and III FCC investigations, respectively) it was suspected that HCP (not FCC) deformation twinning was suppressed in all samples where an HCP to FCC transformation was initiated. In addition, all TEM samples containing FCC Ti precipitates experienced stresses along the $\langle 0001\rangle_{HCP}$ in some form. Therefore, it is proposed that the series of transformations observed in the strain induced FCC Ti; HCP-to-FCC, and FCC-to-FCC twin help accommodate strains along the $\langle 0001\rangle_{HCP}$ when deformation twinning and (**c**+**a**) dislocation slip are not available.

To Hampton

Thank you for making me a good human

Contents

1. Introduction, Phases and Crystal Structure of Titanium..... 1
1.1. Primary Ti Phases – α and β..... 2
1.2. Martensite Ti Phases – α', α", and ω..... 5
1.3. FCC Titanium..... 7
1.3.1. FCC Ti in Evaporated Films..... 8
1.3.2. FCC Ti in Cross-Sectioned Multilayers..... 8
1.3.3. FCC Ti in Ball-Milled Powders..... 9
1.3.4. FCC Ti in TEM Foils..... 10

2. FCC Ti Type I, The FIB Induced Case..... 14
2.1. Specimen Preparation and Characterization..... 14
2.2. Results and Discussion..... 17
2.3. Conclusion..... 26

3. FCC Ti Type II, The Thermally Induced Case..... 27
3.1. Specimen Preparation and Characterization..... 27
3.2. Results and Discussion..... 29
3.3. Conclusion..... 38

4. FCC Ti Type III, The Strain Induced Case..... 39
4.1. Specimen Preparation and Characterization..... 39
4.2. Results and Discussion..... 41
4.3. Conclusion..... 55

5. The HCP - FCC Transformation, Background & Transformation Mechanisms..... 56
5.1. Related Transformations in the Literature..... 56
5.1.1. HCP – FCC Transformations in Cobalt..... 56
5.1.2. HCP – FCC Transformations in Titanium..... 60
5.2. Proposed HCP to FCC Transformation Mechanisms..... 62
5.2.1. Mechanism I – Alignment of the Close-Packed Planes..... 63
5.2.2. Mechanism II – Alignment of the Close-Packed Directions..... 66
5.3. Summary..... 67

6. References..... 69

7. Appendix A..... 78
A.1. A.1. HCP Crystallography..... 78
A.2. Dislocations in HCP Metals..... 82
A.2.1. $\vec{a}$ Type Dislocation Slip Systems in HCP Metals..... 83
A.2.2. $\vec{c}+\vec{a}$ Type Dislocation Slip Systems in HCP Metals..... 87
A.2.3. $\vec{c}$ Type Dislocation Slip Systems in HCP Metals..... 90

Acknowledgements

I have read many theses and dissertations during my tenure as a Ph.D. gradate student at UC Berkeley and have found that the literature review and experimental methods sections were instrumental to my research. The latter in particular since the formation of FCC Ti was largely an artifact of TEM sample preparation. In an effort to pay-it-forward, a comprehensive background and very detailed experimental methods is provided in this dissertation. The title was intentionally made to be simplistic for easy accessibility to others investigating FCC Ti or to those simply trying to prepare a TEM foil free of FCC artifacts. All of the work published within this dissertation was only made possible with the help and support of many people. Though many of you will likely never read this, I still would like to say yet again, thank you.

I wish to first acknowledge my advisor, Andy Minor. Your guidance, encouragement, patience, and clear passion for materials science have taught me to persevere when faced with the unknown and to strive to answer that fundamental "why" anything does what it does. You have been a vital role model and mentor to me over the past six years and have helped shape me both professionally and personally. I am forever grateful for your shared wisdom and for having the privilege to learn at your side. Though my time at Berkeley is drawing to an end, I hope to continue collaborating and discussing ideas with you in the future, preferably over pizza and beer at La Vals.

Next, to my family, though we are a continent apart, you have been with me every step these past years. Words cannot express how thankful I am for your unconditional love, support, and understanding. I would never have gotten through this without y'all. Sarah, Daddy, Momma, Rosemary, Hank, Meagan, Michelle, Matt, Aerin, Grandma, Mimi, and uncle Johnny, you were always there whenever I needed to talk and help me put everything back into perspective whenever work became too overwhelming. I am truly blessed to have you all in my life and know you will be right there with me while I start this next chapter. Clan Taylor!

To my fellow Minor group members old and new and my colleagues at UC Berkeley, NCEM, and the Molecular Foundry, you all were instrumental to my success. I am so fortunate to have been surrounded by so many great minds while pursuing this degree. You have helped me develop my critical thinking and technical skills by challenging me with alternative viewpoints and through countless training sessions. Thank you for all of your time, insight, shared wisdom, and general interest and willingness to help someone with a problem that was unrelated to your work. That kind of selflessness is hard to come by and I will truly miss interacting with you all on a regular basis.

Finally, to my closest friends, it is hard to believe that it has only been six years since I first met most of you upon arriving at Berkeley. Getting to know you all has been one of the brightest highlights of graduate school. Claire and Jon, thank you for all of the late night conversations and for helping me make it through the tough times. Dom, having you as a roommate for the past six years has been an adventure. Thank you for making the Dogfort a home. And last but certainly not least, Jake, you welcomed Hampton and me into your life with open arms. Your love and support throughout this Ph.D. endeavor has made me feel like I can accomplish anything if I set my mind to it. You and me, together, we can do anything.

Chapter 1. Introduction

Phases and Crystal Structure of Titanium

Titanium (Ti) and Ti-alloys have garnered much attention over the past century largely due to their popularity as base materials for high performance structural applications. Titanium's high strength, low density, good creep resistance, and, most importantly, superior corrosion resistance are ideal for land and jet gas turbine engines, biomedical devices, and components in chemical processing equipment [1]. Since these applications dramatically differ in their Ti performance needs, there is motivation to design and develop Ti alloys for specific usage. The ability to manipulate the structural properties of Ti and its alloys depends on alloy content, microstructure, and stability of the combined and individual solid phases of interest. As a consequence, there have been a considerable number of phase stability and phase transformation studies conducted on Ti and Ti-alloys.

The known stable phases of bulk pure Ti are; the low temperature hexagonal close packed (HCP) alpha phase (α-Ti), the high temperature body centered cubic (BCC) beta phase (β-Ti), and the high pressure hexagonal omega phase (ω-Ti). Figure 1.1 presents the crystal structures and lattice parameters of the α-, β-, and ω-Ti phases. The single component Ti phase diagram acquired from Henning *et al*. [2] is also presented in Figure 1.2.

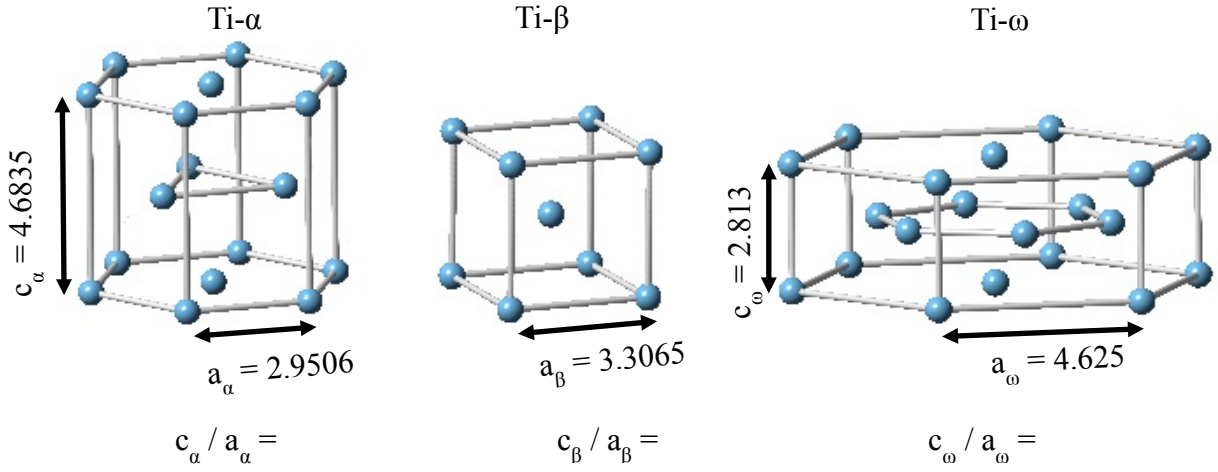

Figure 1.1: Schematics of the α-Ti HCP, β -Ti BCC, ω -Ti hexagonal crystal structures. Lattice parameters were acquired from Lutjering *et al*. (2007) [1].

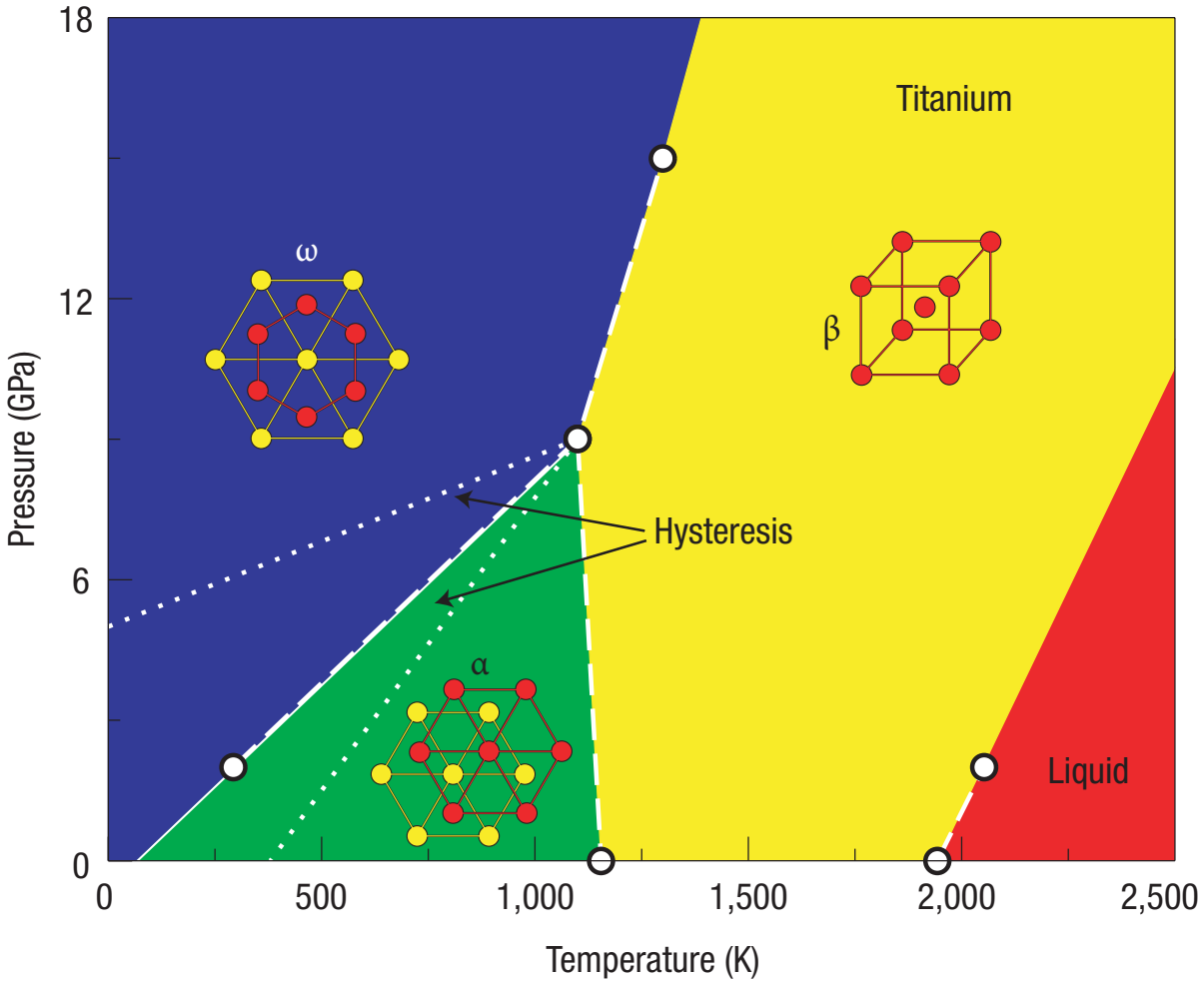

Figure 1.2: Taken from R.G. Hennig et al. (2005). *Nat. Mater.*, **4**, p. 129. Single component Ti phase diagram [2].

1.1. Primary Ti Phases – α and β

Molten pure Ti solidifies into the β phase and transforms into α-Ti when cooled below the α/β-transus temperature, which is approximately 882°C for pure Ti at standard pressure [1]. Alloying elements in Ti are usually classified as either α or β stabilizers depending on whether they increase or decrease the α/β-transus temperature, respectively. A diagram dividing a few known α and β stabilizers according to the type of binary phase diagram they create with Ti was taken from S. Banerjee *et al*. [3] and is presented in Figure 1.3.

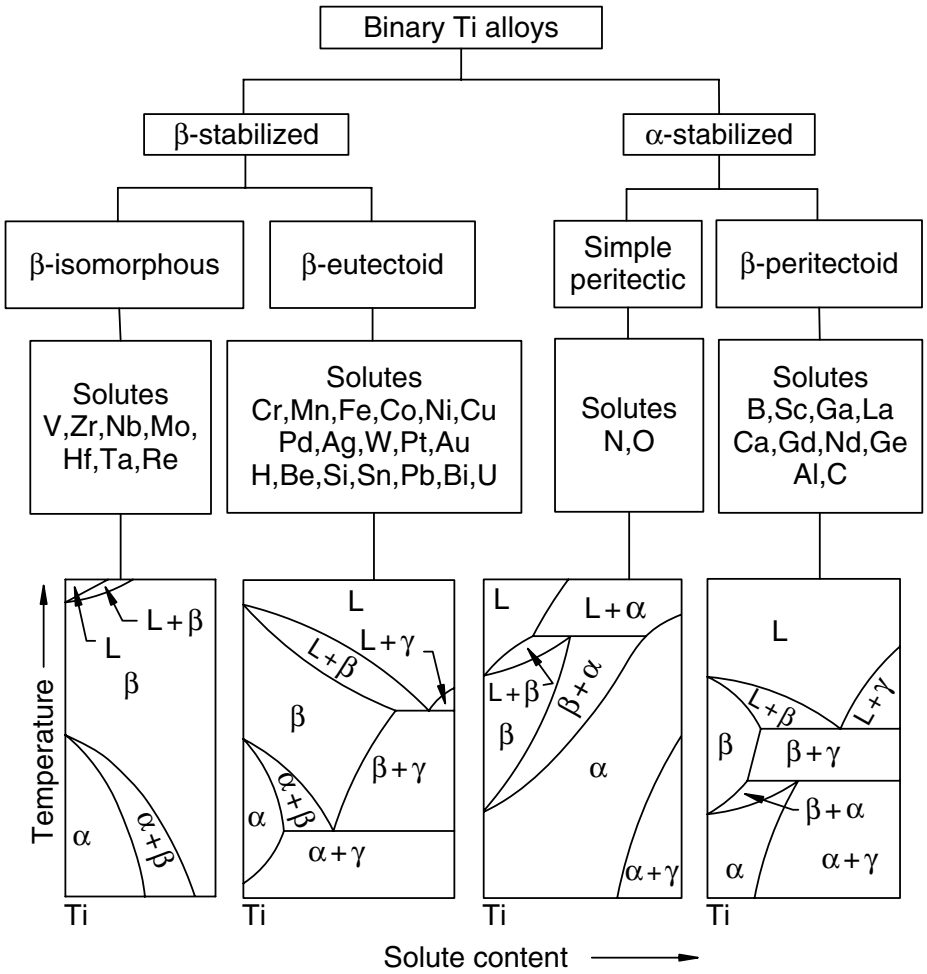

Figure 1.3: Taken from S. Banerjee et al. (2007). *Phase Transformations: Examples from Titanium and Zirconium Alloys, First Ed*. p. 28. A classification scheme for α and β stabilizers in Ti based on their binary Ti–X equilibrium phase diagrams. The legends α, β, and γ stand, respectively, for the α-Ti phase, the β-Ti phase, and the intermetallic phase (γ) [3].

The substitutional element aluminum (Al) and the interstitial elements oxygen (O), nitrogen (N), and carbon (C) are all strong α stabilizers and increase the α/β-transus temperature with increasing solute content. Due to its extensive solubility in Ti, high concentrations of O (≥ 27 at.%) can promote α-phase nucleation directly from the melt as an intermediate disordered phase [4]. A few other known α stabilizers are boron (B), gallium (Ga), germanium (Ge), and the rare earth elements. However, these elements have much lower solid solubility in Ti than the strong α stabilizers and are generally not incorporated during alloy production. The β stabilizers are divided into two groups according to the type of binary Ti-solute phase diagram produced, i.e. β isomorphous and β eutectoid forming elements [3]. Vanadium (V), molybdenum (Mo), and niobium (Nb) are the most commonly used β isomorphous stabilizers, whereas chromium (Cr), iron (Fe), and silicon (Si) are the preferred β eutectic forming stabilizers. Hydrogen (H) is also a β eutectic forming stabilizer with a very low eutectoid temperature of 300°C. However, due to hydrogen embrittlement and the potential for titanium hydride formation, the H content in Ti is strictly limited to about 125-150 parts per million (ppm) [1].

Pure α-Ti is more ductile and corrosion resistant than any Ti-alloy. However, due to Ti's high reactivity with O and intensive refining processes, nominally pure Ti is quite difficult and costly to produce [1]. As such, commercially pure (CP) α-Ti alloys are more commonly used in lieu of high purity α-Ti for industrial applications, which are categorized into different grades according to their O content [1]. Alloying pure Ti with α stabilizers reduces the ductility and increases the strength of the alloy. These alloys are classified as α- or near α- Ti alloys and are prized for their superior corrosion resistance. Alloying with β stabilizers also leads to dramatic increases in strength at the cost of reduced ductility. Since β-Ti is unstable under ambient conditions, β-Ti alloys are metastable in nature and are heavily doped with β stabilizers. Therefore, α- and near α-Ti alloys tend to be more ductile than metastable β-Ti alloys.

Dual phase (α+β)-Ti alloys can exhibit a variety of microstructural permutations and combinations that offer a range of strength, toughness, and high temperature properties. Interestingly, some of these binary phase (α+β)-Ti alloys have higher strengths and are more ductile than single phase α- and β- Ti alloys despite their high alloy contents. Although deformation twinning is nearly fully suppressed in (α+β)-Ti alloys, it is believed that small phase dimensions are responsible for the increased ductility [1]. This demonstrates that the ability to control and manipulate the (α+β) microstructure, i.e. α phase size, morphology and distribution within the β-matrix, is critical for the successful design and development of Ti alloys with desired materials properties. The (α+β) phase morphology is strongly dependent on the β-to-α phase transformation(s) during cooling, which can occur martensitically or by diffusion controlled nucleation and growth processes. Regardless of the transformation mechanism, the orientation relationship $\{110\}_\beta \parallel (0002)_\alpha$, $[1\bar{1}1]_\beta \parallel [11\bar{2}0]_\alpha$, known as the Burgers orientation relationship (BOR), is strictly obeyed. By this relationship, up to twelve crystallographic variants, i.e. twelve possible daughter α orientation relationships from a single parent β crystal, are possible [4]. A schematic of the crystallographic relationship between α and β plates within a colony was taken from Lutjering *et al*. [1] and is presented in Figure 1.4.

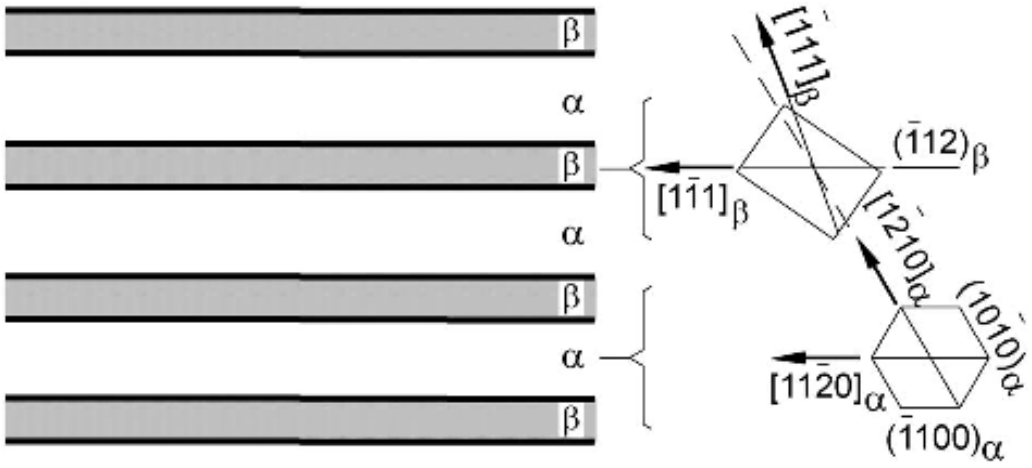

Figure 1.4: Taken from G. Lutjering *et al*. (2007). *Titanium, Second Ed*. p. 33. Representation of the crystallographic relationship between α plates and β matrix in α colonies [1].

The diffusion-based β-to-α phase transformation mechanism is dominant for alloys that are slowly cooled from the β phase field to the (α+β) phase field. Initially, α nucleates at β grain boundaries, which are semicoherent with one another, until a continuous α phase forms along β grain boundaries. Upon further cooling, plate-shaped α nucleates at the α/β interface and grows into the β grain in parallel plates (or colonies), and all α plates within an α colony have the same BOR. These α colonies continue to grow into the β grain interior until they encounter other α colonies (with different BOR variants) that nucleated elsewhere within the same β grain. This results in a lamellar (α+β) microstructure where the flat surface of the α plates align parallel to the $\{\bar{1}100\}_\alpha$ and $\{\bar{1}12\}_\beta$ planes. As cooling rate increases the thickness of the α plates, as well as the size of the α colonies, decreases. This is primarily due to secondary α colony nucleation at primary α colony boundaries, thereby resulting in a "basket weave" characteristic microstructure that has a more uniform distribution of the twelve BOR variants [1].

1.2. Martensite Ti Phases – α', α", and ω

At sufficiently high cooling rates, i.e. quenching from the β phase field, and depending on the alloying content and atmospheric conditions, one of three types of martensitic phase transformations can occur as the β phase stability increases: 1) α' (HCP structure), 2) α" (orthorhombic structure), and 3) ω (simple hexagonal structure) [3]. Since ω-Ti can also form directly from the α phase, it will be discussed separately from the α' and α" martensitic phases. The β-to-α' and -α" martensitic transition is a shear transformation and involves three distinct and sequential processes. First, a Bain distortion transforms the BCC lattice into a hexagonal or orthorhombic lattice. Second, a lattice invariant shear (LIS), i.e. dislocation slip or twinning, occurs to minimize the strain energy produced by the Bain distortion. This minimization is achieved by making all the resultant Bain strains a homogeneous invariant plane strain (IPS), i.e. the LIS produces a continuous, undistorted, and unrotated (invariant) habit plane between the martensite phase and the β matrix. This IPS condition is characteristic of martensitic phase transformations [3]. Third, an organized atomic shuffle, also known as a "military shift", on every alternate $(110)_\beta$ plane in the $[1\bar{1}0]_\beta$ direction moves the atoms to their proper positions within the hexagonal or orthorhombic martensitic structures [3–4]. The entire shear transformation process involves the activation of the shear systems: $<111>_\beta \{11\bar{2}\}_\beta$ and $<111>_\beta \{\bar{1}01\}_\beta$ or in hexagonal notation: $<2\bar{1}\bar{1}3>_\alpha \{\bar{2}112\}_\alpha$ and $<2\bar{1}\bar{1}3>_\alpha \{\bar{1}011\}_\alpha$. The transformed volume is generally disk shaped and the β/α' and β/α" orientation relationships also obey the BOR discussed previously [1].

The α' phase tends to form in β stabilizer lean Ti alloys and can be found in two morphologies, massive martensite (or lath or packet martensite) and acicular martensite. Massive martensite occurs in pure Ti, very dilute Ti alloys, and Ti alloys with high martensitic transformation temperatures. It is commonly observed in 50-100μm sized α' colonies with parallel 0.5-1μm thick α' lathes of the same BOR [1]. Acicular martensite occurs in Ti alloys with higher solute content (i.e. lower martensitic transformation temperature) and is composed of α' lathes with a mixture of BORs. The α' lathes in both morphologies generally have high dislocation density and occasional twins. These defect can act as β phase nucleation sites during annealing for α' martensites that are supersaturated in β stabilizers [1]. Since orthorhombic α" forms in β stabilizer rich alloys, it is considered to be a distorted hexagonal phase, where the distortion is a

result of the alloying elements hindering the atomic shuffle. Recently, α" was also reported to isothermally nucleate from the β phase as an intermediate step before transforming to the stable α phase, i.e. β-to-α"-to-α, and was proposed to be connected to the local chemical content at the nucleation site and the diffusivity of the solutes [4].

For Ti alloys where the "military shift" martensitic reaction is suppressed, the ω phase can form athermally through a diffusionless transformation upon quenching from the β phase field. This athermal ω phase (ω_{ath}) forms as dispersed 2-4nm sized particles, and is suggested to precede the transformation to α" since its transformation involves a $<111>_\beta$ shear displacement in the β lattice. The β-to-ω_{ath} transformation mechanism involves the collapse of alternating $(111)_\beta$ plane pairs. Collapsing two out of every three of the $(111)_\beta$ planes towards each other can be described by a displacive wave with a wavelength and amplitude of $3d_{222}$ and $½d_{222}$, respectively [4]. This mechanism is depicted in Figure 1.5 and results in a final $(111)_\beta \parallel (0001)_\omega$ orientation relationship [5].

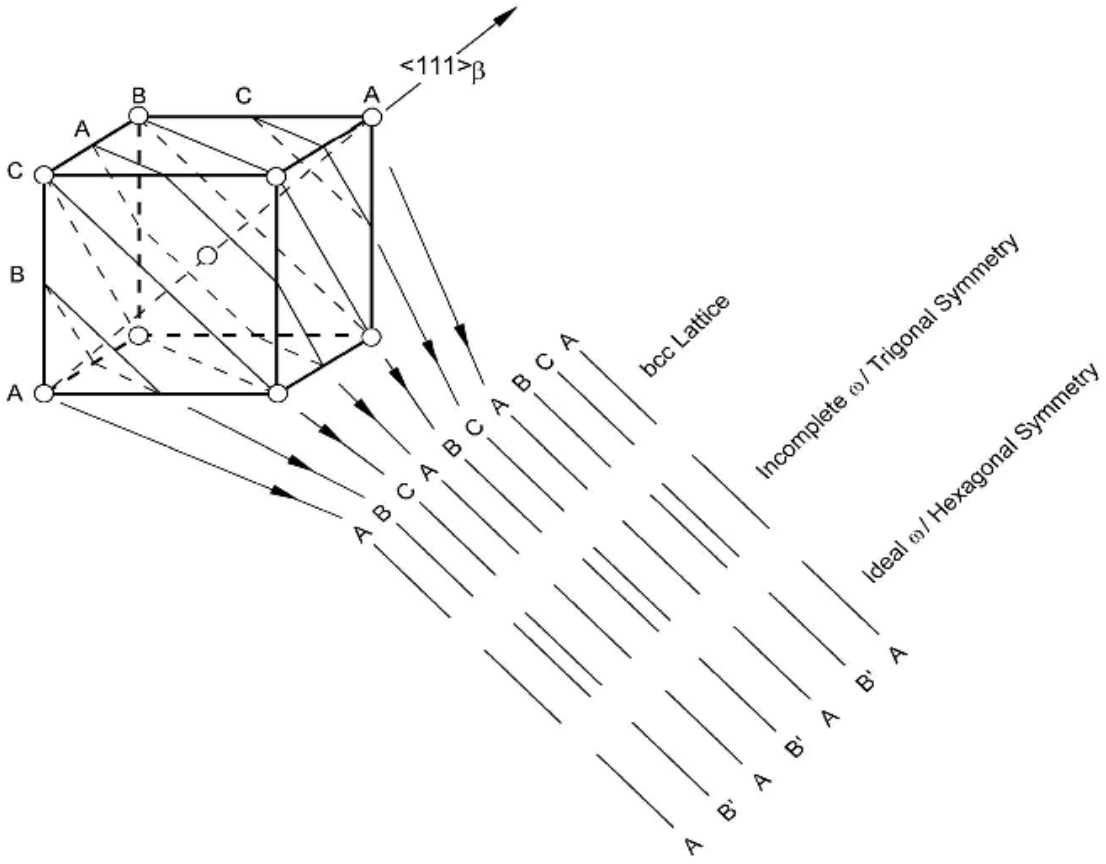

Figure 1.5: Taken from G. Lutjering *et al*. (2007). *Titanium, Second Ed*. p. 31. Representation of the β to ω transformation showing the $(222)_\beta$ planes of the BCC lattice.

The degree of the $(111)_\beta$ collapse decreases with increasing β stabilizer content and the symmetry of the ω structure reduces from hexagonal to trigonal. When Ti alloys containing ω_{ath}

particles are isothermally aged, the ω_{ath} phase will rapidly grow, which involves the diffusional rejection of β stabilizer elements in the ω phase. The ω is then classified as isothermal ω (ω_{iso}), which has the same crystallographic symmetry as ω_{ath} but is solute lean with respect to the β phase [1].

The ω phase also forms under high pressures directly from the α phase by diffusionless athermal martensitic transformation mechanisms and is morphologically similar to the ω phase formed in quenched β-phase alloys when induced in pure Ti [4]. However, the α/ω phase boundary is difficult to ascertain due to a hysteresis in the α-ω transformation, i.e. the initial ω phase nucleation in α (formed by applying pressure) partially reverts back to the α phase when the applied pressure is removed. This retained metastable ω remains within the α phase until the alloy is heated to about 100°C for several hours at ambient pressure. This α/ω hysteresis occurs for both static loading (slowly increasing to and holding at high pressure for an extended period of time) and dynamic loading (shock loading at high pressure pulses). Interestingly, the α/ω phase boundary hysteresis is observed to be more extensive for shock loading experiments [3]. Pure α-Ti will transform into ω-Ti at 9 GPa. However, a range of α-to-ω transformation pressures is reported (2 to 9 GPa) for various Ti alloys and is assumed to be related to the degree of purity [2]. The initial pressure required for the α-to-ω is minimized at a critical β stabilizer content and is a function of the solute type. Strong α stabilizers are shown to dramatically increase the α-to-ω transformation pressure, which suggests that the transformation pressure is affected by the stability of the α and β phases [4].

1.3. FCC Titanium

Despite its absence in the single component equilibrium phase diagram [2], a face-centered cubic (FCC) phase of Ti has also been reported to nucleate, in addition to α", during rapid quenching in Ti-20Zr-6.5Al-4V ingots [6–7] and sintered compacted discs of pure Ti powders [8]. Interestingly, it was found that thermal aging reduced the overall volume of the α" and FCC phases in the Ti-20Zr-6.5Al-4V system, which were presumed to completely transform into the stable HCP α phase upon aging at 450°C and 700°C, respectively [7]. However, the disappearance of the FCC phase in the pure Ti compacted discs occurred after stress relief annealing at 400°C. FCC Ti has also been observed at α/β interfaces in Ti-6Al-4V and is said to nucleate during slow cooling from elevated temperatures, i.e. above the β transus, until about 650°C [9–11]. While these findings appear contradictory, it can be inferred that FCC Ti stability is affected by temperatures 350°C–700°C. The onset of FCC Ti nucleation in high purity Ti TEM foils (~600°C) recently reported by Yu *et al*. [12] also falls within this temperature range, and this thermally induced FCC phase, termed 'thermal FCC Ti', is one of two FCC Ti variants chemically investigated in the current study. The other FCC Ti variant discussed, termed focused ion beam (FIB) FCC Ti, was observed to disappear upon heating to 350°C *in situ* TEM, as discussed later, and therefore is distinct from the thermal FCC Ti. These dramatically differing responses to heating, in addition to the wide range of reported lattice parameters and high variability between samples, suggest that multiple FCC Ti phases are possible and likely differ from one another in chemical composition. Table 1.1 (presented at the end of this chapter) organizes a majority of FCC Ti investigations according to the reported FCC Ti lattice parameter for reference. Elucidating the chemical nature and the environmental conditions that promote the

formation of these FCC Ti phases is of great importance since their presence is known to alter the mechanical deformation behavior of the alloy [6–12, 55–58].

1.3.1. FCC Ti in Evaporated Films

FCC Ti has been observed on numerous occasions ever since its discovery by Wawner *et al*. [13] in 1969 vacuum evaporated/deposited thin films. They found that Ti initially deposited with an FCC structure and grew epitaxially on textured NaCl substrates with continued deposition. The FCC films grew in thickness until the onset of a FCC to HCP transformation. This critical film thickness, above which no FCC Ti was detected, was shown to be highly dependent on the substrate orientation and temperature and was maximized for the $(110)_{NaCl}$ grown films at 500°C [13]. Interestingly, both of the HCP to FCC transformations observed in the present study; 1) FIB FCC Ti and 2) thermal FCC Ti, obeyed similar film orientation and temperature restrictions (but for the parent HCP phase), and FCC Ti nucleation was limited to prism oriented thin films exclusively, i.e. films with surface plane normal directions near and between $\langle 01\bar{1}0\rangle_{HCP}$ and $\langle 2\bar{1}\bar{1}0\rangle_{HCP}$. The relationship between FCC Ti film thickness and substrate orientation and temperature has been observed repeatedly in vacuum deposited Ti films for various substrates and under varying deposition conditions [13–33]. However, the conclusions drawn from many of these investigations conflict with one another, typically in regard to the chemical make-up of FCC Ti. For example, several reports claim that FCC Ti is a stable phase in ultra thin films, and due to the film orientation-thickness dependence and formation under high vacuum (supplemented occasionally with a brief chemical analysis), it is chemically identical to the neighboring HCP α phase and cannot be one of the frequently suspected Ti impurity compounds presented in Table 1.2 [13–22]. Conversely, several other reports argue that Ti forms FCC-like compounds upon the diffusion of certain atomic species in the substrate into the film [23–26], or that it is actually TiH_x and/or TiO_y crystallites, which readily form during the earliest stages of deposition due to the high reactivity of Ti [27–33].

Table 1.2: Lattice parameters for a few Ti compounds that form FCC-like structures [20, 27]

Ti Compound [TiX]	Composition [at.% X]	Prototype Phase	Lattice Parameters [Å]
TiC	~32−48.8	NaCl	$a_{TiC} = 4.33$
TiN	28 to > 50	NaCl	$a_{TiN} = 4.24$
γ TiO	34.9−55.5	NaCl	$a_{TiO} = 4.29$
TiGa*	40.5−50	AuCu	$a_{TiGa} = 3.97$
δ hydride	60−66.7	CaF_2	$a_{\delta H} = 4.45$
ε hydride	> 66.7	ThH_2	$a_{\varepsilon H} = 4.5$ | $c_{\varepsilon H} = 4.3$ | $c_{\varepsilon H}/a_{\varepsilon H} = 0.96$
γ hydride*	44−50	…	$a_{\gamma H} = 4.2$ | $c_{\gamma H} = 4.6$ | $c_{\gamma H}/a_{\gamma H} = 1.09$

1.3.2. FCC Ti in Cross-Sectioned Multilayers

FCC Ti has also been widely observed in vacuum deposited Ti –Ni [34–36], –Al [37–46], –Ag [47], –Zr [48], and –Cu [49] multilayers, and, as was the case for the single deposited Ti films, a consensus on the chemical identity of the FCC Ti phase has yet to be achieved. However, a vast

majority of the FCC Ti multilayer studies do agree that the HCP to FCC transformation occurred during cross-sectional TEM sample preparation, i.e. for microstructural assessment of the Ti –Ni, –Al, –Ag, –Zr, or –Cu interfaces. However, the Ti layers remained HCP during plane view milling. It can be assumed that all FCC Ti multilayer investigations were similarly oriented, as the as-deposited HCP Ti and FCC –Ni, –Al, –Ag, –Zr, and –Cu layers preferentially aligned their respective close packed planes, i.e. the $\{0001\}_{HCP}$ and $\{111\}_{FCC}$, to be parallel in the plane with the film. This resulted in prism oriented Ti layers upon cross-sectional thinning. However, it is unclear if this observed orientation dependency is a consequence of film surface orientation, beam damage induced by $[0001]_{HCP}$ directional ion bombardment, or a combination of the two. The orientation requirements on nucleation, in addition to the transformation occurring at high vacuum and at low temperatures, was a common argument against the identification of FCC Ti as an impurity based FCC-like compound [34–40, 45–48]. The investigations into FCC Ti nucleation in Ti–Al multilayers conducted by R. Banerjee *et al*. [37, 40, 42–44] initially adopt this argument against an impurity driven HCP to FCC transformation but later concedes that a significant amount of hydrogen is available and is absorbed by the HCP α-Ti phase during ion milling. They go on to point out the distinction that FCC Ti in multilayers with lattice parameters around 4.4Å are likely Ti-hydrides (namely δ-TiH_2 and γ-TiH), while FCC Ti crystallites with relatively small FCC lattice parameters (~4.03Å) may be a legitimate metastable FCC phase of Ti that is stabilized (both structurally and chemically) by the surrounding FCC Al layers [44]. The formation of Ti-hydrides due to ion milling is supported by the authors, as the preferential crystal and ion beam orientation and milling conditions that resulted in FCC Ti nucleation in Ti-multilayers (as well as the reported FCC Ti lattice parameters) were highly similar to those governing the FIB induced HCP to FCC transformation currently under investigation. It is hypothesized that heavy amounts of deformation and the accumulation of defects, due to $[0001]_{HCP}$ directional ion bombardment for example, destabilizes the HCP α-Ti phase and promotes the HCP to FCC transformation through stacking faults and the ordered glide of Shockley partial dislocations. This deformation, or strain, induced explanation is commonly put forward to rationalize the HCP to FCC transformation observed in ball milled Ti microparticles [50–53] and in TEM foils prepared from deformed Ti alloys [54–58].

1.3.3. FCC Ti in Ball-Milled Powders

FCC Ti observations in ball milling studies have shown that the extent of FCC formation was dependent on the ball milling intensity and duration. Consequentially, it was concluded that high strains, defect accumulation, and grain refinement promoted the FCC phase [50–53]. Zhang *et al*. [50] also claims that the heat generated during ball milling thermally activated the HCP to FCC transformation, which, according to their differential scanning calorimetry (DSC) results, was endothermic and initiated at 321°C. Around 439°C an exothermic reaction was initiated, i.e. the assumed onset of FCC Ti decomposition, and the XRD peaks corresponding to FCC Ti disappeared at 550°C. These temperatures and endothermic nature of the HCP to FCC reaction led to the conclusion that ball milled FCC Ti could not be a hydride nor an oxide as these reactions are exothermic. However, this was later contradicted by Vullum *et al*. [53] who claimed that ball milling led to the formation of TiH_x ($x<0.67$) crystallites that were unstable under a TEM electron beam and decreased in lattice parameter (4.22Å to 4.10Å) with continued exposure. This resulting "pure" FCC Ti phase was stable under ambient conditions and it was suspected that both hydrogen and the small crystallite size (10-20nm) contributed to FCC Ti

stabilization. The formation of FCC impurity compounds instead of a potentially "pure" FCC Ti phase during ball milling was too easily dismissed by Manna *et al*. [52]. They attempted to address the contamination issue by; 1) referencing conclusions made from earlier studies [46–47, 51], 2) comparing their experimentally measured FCC lattice parameter with the known lattice parameters of FCC-like Ti impurity compounds (see Table 1.2), 3) performing energy dispersive spectroscopy (EDS), 4) assumed that toluene (i.e. the added lubricant to prevent clogging and agglomeration during ball milling) was the only possible source of impurities and the HCP to FCC transformation was observed during dry mechanical attrition (i.e. without toluene), and 5) conducting resistivity measurements. The first argument was inherently biased since they did not include any FCC Ti references that disagreed with their conclusions and the second did not account for the estimated range of error around their lattice parameter measurement nor for the possibility that a strained Ti-impurity compounds may not be identical to what is reported in the literature. The fourth argument is of course ludicrous as the ball milling process was not performed under vacuum and air is a ready source of H_2, N_2, CO_2, H_2O, etc. Their EDS and resistivity measurements appear to be the only sincere attempt at chemically identifying this FCC phase, which do suggest that FCC Ti is not TiC, TiO, nor TiN. However, the γ-TiH_x ($x < 0.67$) and δ-TiH_2 hydrides cannot be detected with EDS and are known to have similar electrical conductivity as Ti metal [59]. Therefore it remains a distinct possibility that the FCC Ti phase formed due to prolonged ball milling is a form of Ti hydride.

1.3.4. FCC Ti in TEM Foils

It is well known that hydrides can form in Ti alloys during thin foil preparations for TEM [60], which raises the suspicion that the FCC Ti phase observed in TEM samples are actually Ti hydrides. However, phase transitions in Ti foils due to "spontaneous relaxations" of the film has also been recognized for some time, particularly in metastable β alloys containing martensitic phases (HCP α', orthorhombic α", and hexagonal ω) [61]. FCC Ti observations in these alloys typically suggest that the FCC phase forms as an intermediate structure when the metastable BCC phase attempts to transform into the stable HCP phase. This transformation is thought to be driven by local gradients in solute content near α-β interfaces and/or once the constriction of the bulk lattice is removed, i.e. thinning into a film [9–11, 62]. Rhodes *et al.* [9–11] observed an FCC Ti phase at α/β interfaces in Ti-Ti-6Al-4V, which was said to nucleate during slow cooling from elevated temperatures. However, this was later disputed by D. Banerjee *et al*. [62] who concluded that the FCC "interface phase" was a hydride, which was induced through hydrogen absorption during sample thinning and may be accompanied by stress relaxation effects. More recently, Sarkar *et al*. (2014) [54] reported that an FCC Ti structure formed during two TEM sample preparation methods, ion milling and electro-polishing, but only within the α-phase of the metastable β-Ti alloy, Ti-15V-3Sn-3Cr-3Al, i.e. not an interface FCC Ti phase. Unlike D. Banerjee *et al*. [62], this FCC Ti phase was concluded to not be a form of Ti hydride, though it similarly suggested that the HCP to FCC transformation occurred during TEM sample preparation as a means to reduce the intrinsic stresses formed during alloy processing.

Most recently, a deformation induced HCP to FCC transformation has been reported several times in larger samples of CP Ti [55–57] and Ti-6Al-4V [58], and they suggest that the transformation is strongly related to deformation twinning and/or partial dislocation slip. Interestingly most found that the HCP-FCC phases were not oriented to one another in the

conventional close-packed arrangement, i.e. $\{0002\}_{HCP} \parallel \{11\bar{1}\}_{FCC}$, but instead adopted a $\{0002\}_{HCP} \parallel \{002\}_{FCC}$ configuration. However, the metastable γ-TiH_x ($x<0.67$) hydride is also known to exhibit this non-close packed arrangement with the HCP phase [63–67] and all of these investigations neglect to address the possibility of hydride contamination during TEM sample preparation. Niu *et al*. [57] was the only one of the aforementioned studies that supported their TEM results with an additional method for identifying the FCC phase, and their XRD results indicated that the transformation occurred during uniaxial tensile loading to high strains and at high strain rates. Their tensile samples had a 3μm average grain size and were only 20μm in thickness, which is in line the reoccurring theme in the literature that the phase dimensions/grain sizes and overall sample thickness have an effect on FCC Ti nucleation. More details on the HCP to FCC transformation mechanism proposed in these FCC Ti investigations are presented in chapter 5.

It can be inferred that sample size, microstructure, temperature, stress state/degree of defect accumulation, and chemical makeup all play a role in the HCP to FCC transformation in Ti. Several computational reports have attempted to define the conditions that promote FCC Ti nucleation [68–74]. However, the large discrepancy in the experimentally reported lattice parameter and combinations of conditions under which it occurs strongly suggest that not all FCC Ti phases are one and the same. Three independent FCC Ti phases were experimentally observed; Type I – upon focused ion beam (FIB) irradiation, Type II – during *in situ* heating in a transmission electron microscope (TEM), and Type III – during *in situ* TEM straining. FIB FCC Ti is concluded to be Ti hydride and most closely resembles the HCP to FCC transition found in Ti multilayers [34–49], while thermal FCC Ti appears to be strongly linked to oxygen contamination and builds on the recent findings of Q. Yu *et al*. (2017) [12]. Strain-induced FCC Ti was neither hydride nor oxide and readily underwent FCC deformation twinning under the applied strain. The greatest insight into the HCP to FCC in Ti transformation mechanism was generated from the strain-induced case and it is proposed that this anomalous phase transformation was facilitated by HCP **a**-type dislocation ($\vec{\mathbf{b}}=1/3\langle 11\bar{2}0\rangle_{HCP}$) nucleation, dissociation, and propagation.

Table 1.1: A list of FCC Ti references ordered by increasing reported FCC Ti lattice parameter. *Continues onto next page*.

FCC Ti Lattice Parameter [Å]	Ref. [#]	FCC Ti References with Reported FCC Lattice Parameters
4.01	35	R. Banerjee *et al*. (1995). *Acta Mater*., **47**(15), p. 4225-4231.
4.0197	13	L.P. Yue *et al*. (1994). *Nanostruct. Mater.,* **4**(4), p. 451-456.
4.03, 4.4	42	R. Banerjee (2014). *Thin Films: Structural Transitions, 3rd ed.*, p. 4920-4930.
4.05	21	A.A. Saleh *et al*. (1993). *J. Vac. Sci. Technol., A*, **11**, p. 1982-1986.
4.055	17	N. Arshi *et al*. (2013). *Bull. Mater. Sci.,* **36**(5), p. 807-812.
4.06	4	R. Jing *et al*. (2013). *Mater. Sci. Eng. A*, **559**(1), p. 474-479.
4.06	24	L. Wang *et al*. (2007). *J. Appl. Phys.*, **101**, id. 24370, p. 1-11.
4.09	53	H.C. Wu *et al*. (2016). *Sci. Rep.*, **6**(1), id. 24370, p. 1-8.
4.1	6	A.S. Bolokang *et al*. (2014).*Mater. Lett*., **132**(1), p. 157-161.
4.10 to 4.22	51	P.E. Vullum *et al*. (2009). *Appl. Phys. A*, **94**(4), p. 787-793.
4.11	66	A. Aguayo *et al.* (2002). *Phys. Rev. B*., **65**, p. 1-4.
4.12 ± 0.03	10	Q. Yu *et al*. (2017). *Scripta Mater.,* **140**, p. 9-12.
4.146 ± 0.025	14	S.K. Kim *et al*. (1996). *J. Phys. Condens. Matter.,* **8**, p. 25-36.
4.158	56	Y.G. Liu *et al*. (2016). *Scripta Mater.*, **119**, p. 5-8.
4.1638	15	J. Chakraborty *et al*. (2011). *Acta Mater.,* **59**(7), p. 2615-2623.
4.18 to 4.38	26	T. Harada *et al*. (1997). *J. Cryst. Growth.*, **171**(1-2), p. 433-441.
	27	T. Harada *et al*. (1997). *J. Cryst. Growth.*, **173**(1-2), p. 109-116.
4.18 to 4.6	28	Y. Yamada *et al*. (1990). *Jpn. J. Appl. Phys*., **29**, p. 706-709.
	29	Y. Yamada *et al*. (1990). *Jpn. J. Appl. Phys*., **29**, p. L1888-L1891.
	30	Y. Kasukabe *et al*. (1990). *Jpn. J. Appl. Phys*., **29**, p. L1904-L1906.
4.2	7	C.G. Rhodes *et al*. (1975). *Metall. Trans. A.,* **6A**, p. 1670-1671.
4.2	23	A. Saleh *et al*. (1997). *Phys. Rev. B: Condens. Matter*, **56**(15), p. 9841-9847.
4.200 ± 0.006	16	M. Fazio *et al*. (2015). *Thin Solid Films,* **593**, p. 110-115.
4.23	22	A. Saleh *et al*. (1994). *Phys. Rev. B: Condens. Matter*, **49**(7), p. 4908-4914.
4.23, 4.42	25	C.J. Lu *et al*. (2003). *J. Appl. Phys.*, **94**(1), p. 245-253.
4.237	49	P. Chatterjee *et al*. (2001). *Appl. Surf. Sci.,* **182**(3-4), p. 372-376.
4.25	31	T. Kado. (2000). *Surf. Sci*., **454-456**, p. 783-789.
4.25	52	R. Sarkar *et al*. (2014). *Phil. Mag. Lett.,* **94**(5), p. 311-318.
4.26	8	C.G. Rhodes *et al*. (1979). *Metall. Trans. A.,* **10A**, p. 1753-1758.
	9	C.G. Rhodes *et al*. (1979). *Metall. Trans. A.,* **10A**, p. 209-216.
	59	R.A. Spurling *et al*. (1974). *Metall. Trans.*, **5**, p. 2597-2600.
	60	D. Banerjee *et al*. (1988). *Acta Metall.,* **36**(1), p. 121-141.
4.26, 4.37	12	Y. Yamada *et al*. (1988). *Appl. Surf. Sci.* **33/34**, p. 465-471.
4.3	55	L. Niu *et al*. (2017). *Mater. Sci. Eng. A*, **707**, p. 435-442.

Table 1.1: *Continued*.

FCC Ti Lattice Parameter [Å]	Ref. [#]	FCC Ti References with Reported FCC Lattice Parameters *continued*
4.302	54	D.H. Hong *et al*. (2013). *Scripta Mater.*, **69**, p. 405-408.
4.3 ± 0.1	45	T. Tepper *et al*. (1997). *Mater. Lett.,* **33**, p. 181-184.
	46	T. Tepper *et al*. (1998). *Mater. Lett*., **35**(1-2), p. 100-107.
4.32, 4.4	32	A.F. Jankowski *et al*. (1994). *J. Mater. Res.,* **9**(1), p. 31-38.
	33	A.F. Jankowski *et al*. (1996). *Nanostruct. Mater.,* **7**(1/2), p. 89-94.
4.33	11	F.E. Wawner, Jr. *et al*. (1969). *J. Vac. Sci. Technol.,* **6**, p. 588-590.
4.33	38	R. Banerjee *et al*. (1996). *Phys. Rev. Lett*., **76**(20), p. 3778-3781.
	40	J. Bonevich *et al*. (1999). *Phys. Rev. Lett.*, **82**(9), p. 2002. Comment
	41	R. Banerjee *et al*. (1999). *Phys. Rev. Lett*., **82**(9), p. 2002. Reply
4.356	50	I. Manna *et al*. (2003). *J. Appl. Phys.,* **93**(3), p. 1520-1524.
4.36	36	R. Ahuja *et al*. (1994). *J. Electron. Mater.,* **23**(10), p. 1027-1034.
	37	R. Ahuja. (1994). *The Ohio State University*. (Doctoral dissertation).
4.38	19	Y. Sugawara *et al*. (2000). *J. Mater. Res*., **15**(10), p. 2121-2124.
4.385	5	R. Jing *et al*. (2013). *J. Alloys Compd.*, **552**, p. 202-207.
4.396	47	J.B. Lai *et al*. (1999). *Micron*, **30**(3), p. 205-211.
4.396	48	D.L. Zhang *et al*. (2002). *Mater. Lett.,* **52**(4-5), p. 329-333.
4.4	39	J. Bonevich *et al*. (1999). *J. Mater. Res*., **14**(5), p. 1977-1981.
4.40 ± 0.18	34	D. Josell *et al*. (1995). *Mater. Lett.,* **22**, p. 275-279.
4.42	43	D. Shechtman *et al*. (1994). *Mater. Lett.,* **20**, p. 329-334.
4.42	44	D. van Heerden *et al*. (1996). *Acta. Mater.,* **44**(1), p. 297-306.

Chapter 2. FCC Ti Type I
The FIB Induced Case

An HCP to FCC structural transformation was induced in high purity alpha-titanium (α-Ti) micropillars upon thinning to electron transparency for transmission electron microscopy (TEM) and transmission Kikuchi diffraction (TKD) experimentation. Originally, these pillars were prepared for *in situ* microcompression in the scanning electron microscopy (SEM) to investigate deformation twinning in α-Ti alloys of varying oxygen (O) contents. Multiple rounds of micropillars were made from Ti-0.1O, Ti-0.2O and Ti-0.3O alloys listed in Table 2.1, and were preferentially oriented for HCP c-axis compression, i.e. along the $[0001]_{HCP}$, in an effort to minimize $\vec{\mathbf{a}}$-type dislocation ($\vec{\mathbf{b}} = \frac{1}{3}\langle\bar{1}\bar{1}20\rangle_{HCP}$) mobility and promote deformation twinning. The FIB/thinning induced HCP to FCC transformation was observed in all three alloys, however, chemical investigations into this FCC Ti phase were only conducted on the Ti-0.1O system. As such, only the results from Ti-0.1O micropillars will be discussed.

Table 2.1: Bulk chemical compositions (in both wt.% and at.%) of all Ti-alloys use in this study, as provided by TIMET Inc. (alloy supplier).

		Al	V	Fe	C	N	O	Ti
Ti-0.1O	[wt.%]	0.005	0.003	0.005	0.003	0.007	0.114	99.9
	[at.%]	0.009	0.003	0.004	0.012	0.024	0.340	99.6
Ti-0.2O	[wt.%]	0.005	0.003	0.006	0.006	0.004	0.207	99.8
	[at.%]	0.009	0.003	0.005	0.024	0.014	0.617	99.3
Ti-0.3O	[wt.%]	0.005	0.003	0.004	0.009	0.001	0.292	99.7
	[at.%]	0.009	0.003	0.003	0.036	0.003	0.868	99.1

Since the appearance of FCC Ti is largely an artifact of sample preparation, detailed notes of all the sample preparation techniques used in this study are provided.

2.1. Specimen Preparation and Characterization

All micropillars were formed on finely polished cutouts of the Ti-0.1O melted bar ingot (~200g) listed in Table 2.1. Each micropillar was initially single crystalline and approximately 2-3μm x 2-3μm x 4-5μm in size prior to thinning. The bulk cutouts were manually polished with sequentially finer grit silicon carbide (SiC) papers and diamond suspensions for electron backscatter diffraction (EBSD) in the SEM. A 0.05μm colloidal silica suspension (OP-S) was used as the final polishing step. A dilute mixture of hydrofluoric acid (1-3mL), nitric acid (2-6mL), and water (100mL), also known as Kroll's Reagent, was occasionally applied to the sample during the final stages of polishing to periodically etch away the α case, i.e. an oxygen rich Ti surface layer that readily forms in high purity Ti alloys during mechanical polishing and becomes quite difficult to remove without the assistance of an etchant [75]. EBSD was then used to locate regions suitable for pillar fabrication, i.e. grains with the desired orientations for *in situ* SEM microcompression testing. The micropillars were formed using (and later thinned with) a

focused ion beam (FIB). Specifically, an FEI Quanta and an FEI Strata 235 dual beam SEM-FIB, both equipped with gallium ion (Ga^{+}) sources and EBSD capabilities.

Four rounds of Ti-0.1O micropillars, labeled R1, R2, R3, and R4, were fabricated, and each round contained between five and ten individual pillars. All pillars were formed at least 5μm away from any polished surface to avoid incorporating any residual damage or contamination due to mechanical polishing. To minimize ion beam damage, the FIB was operated at an accelerating voltage of 30kV and at progressively decreasing currents during fabrication, ranging from 7000nA for initial trench milling to 10pA for final shaping. The second (R2) and third (R3) rounds of micropillars were formed on the sharp edge of a polished bulk cutout, which then necessitated that each pillar within these sets be removed from the bulk and attached to a copper (Cu) 3mm half grid for TEM and TKD evaluation. This "liftout" procedure utilized a tungsten (W) retractable Omniprobe needle and ion deposited platinum (Pt). Pt was generously applied to all pillars, encasing each in a protective shell in an effort to minimize ion beam damage during liftout and thinning. The deposited Pt also acted as the adhesive between the pillars, the Omniprobe, and the Cu half-grid throughout the liftout process. Pt was not applied to the first (R1) and fourth (R4) set of pillars as they were intentionally fabricated to allow for post-thinning TKD and TEM observation while remaining affixed to their Ti-0.1O foundation, i.e. eliminating the need for pillar liftout. This distinction in foil preparation had no apparent influence on FCC nucleation, however, only the R1 and R4 transformed pillars reverted to the HCP phase when heated *in situ* TEM. The liftout transformed pillars (R2 and R3) did not revert back to the HCP phase when heated and it was suspected that this was due to inadequate heat transfer from the TEM holder through the Cu half grid through the Pt encasement to the micropillar. The attached R1 and R4 pillars were formed on polished bulk cutouts that were cut and shaped into a 100μm thick x 3mm diameter segmented disc via an abrasive slurry disc cutter (South Bay Technology Inc. Model 360) and manual polishing. The disc was then polished into a wedge, until one of the flat edges was ≤30μm thick. Micopillars were fabricated near the center of this thinner flat edge of the foil, protruding outward from, but in plane with, the Ti-0.1O foil. Laue diffraction was conducted on the pre-thinned R4 micropillars, both compressed and uncompressed (see Figure 2.1), using the Advanced Light Source (ALS) located at the Lawrence Berkeley National Laboratory (LBNL) to asses the crystal structure of the micropillars prior to thinning.

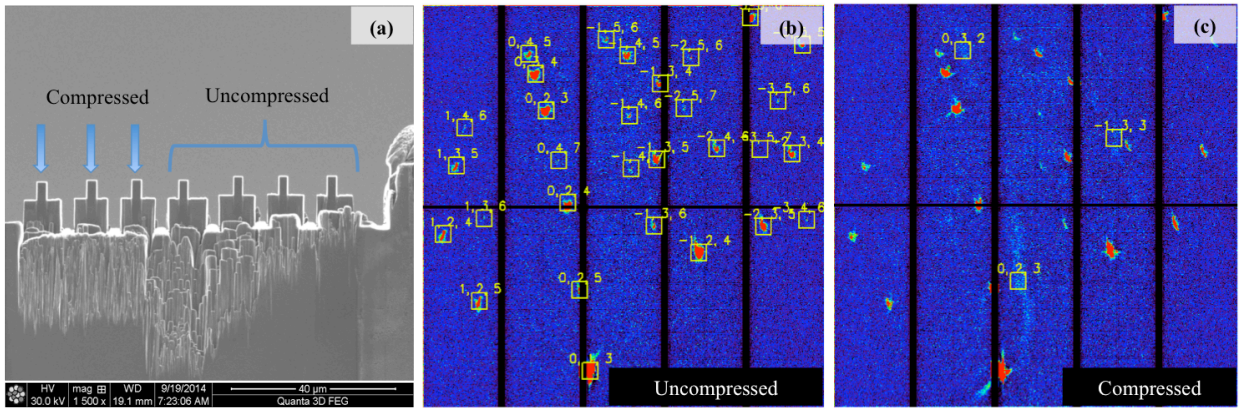

Figure 2.1: (a) The round 4 (R4) single crystalline high-purity α-Ti micropillars prior to any deformation. The pillars labeled "compressed" were compressed after (a) was acquired. (b) and (c) are microLaue diffraction patterns (acquired from the ALS, LBNL) of the uncompressed and compressed micropillars indicated in (a), respectively. The diffraction reflection spot smearing in (c) is a result of mechanical deformation. Note: There was no evidence of an FCC structure (within the detection limits) before or after deformation, i.e. all indices marked in (b) and (c) are from HCP reflections only.

The R2, R3, and R4 micropillars were oriented for $[0001]_{HCP}$ compression, and R1 pillars were compressed along an arbitrary *near* prism axis. Due to the large grain sizes of the ingots (~0.5mm on average), pillars within the same round had similar (assumed identical) orientations. However, these differed between micropillar rounds. After mechanical testing, and pillar liftout (when necessary), the pillars were thinned to electron transparency, via FIB, for TKD and TEM microstructural assessment. The ion beam was directed at a glancing angle very nearly parallel to the compression axis (±1-2°), and was operated at an accelerating voltage of 30kV and an initial current no more than 0.5nA (often less), which was decreased to 10pA in multiple steps. The accelerating voltage was dropped to 2kV for a final cleaning of the foil surface.

All TKD experiments followed the methodology proposed by Geiss *et al*. [76]. TKD maps were acquired using the FEI Quanta dual-beam FIB-SEM, located at the University of California Berkley (UCB). TEM selected area diffraction (SAD), and energy dispersive X-ray mapping (EDS) experiments were conducted using a 300kV JEOL 3010 TEM and a 300kV FEI TitanX TEM/STEM equipped with a Bruker windowless EDS detector, respectively. *In situ* TEM heating experiments on the R4 micropillars were also conducted in the JEOL 3010 to test for hydride contamination. All of the aforementioned TEMs were located at the Molecular Foundry, specifically the National Center for Electron Microscopy (NCEM), within LBNL.

Though atom probe tomography (APT) experimentation unexpectedly yielded results regarding FIB induced FCC Ti, these experiments were intended for investigations into thermally induced FCC Ti and, therefore, the APT sample preparation process will be discussed in relation to the *in situ* TEM heating experiments in the following section.

2.2. Results and Discussion

Ti-0.1O (see Table 2.1) single crystalline rectangular micropillars were fabricated using a FIB for *in situ* SEM compression testing on a Hysitron PI85 setup operated in displacement-controlled mode. Laue diffraction of the pre-thinned R4 micropillars, both compressed and uncompressed (see Figure 2.1), did not indicate the presence of an FCC phase (of detectable size) and all R4 pillars were shown to exhibit the expected α-Ti HCP structure regardless of mechanical testing. The pillars were then thinned to electron transparency (via FIB) for TKD and TEM, upon which an FCC structure was observed. Therefore, it was concluded that this particular FIB induced HCP to FCC transformation occurred as a consequence of FIB irradiation and was likely not dependent on c-axis compression, but rather the resulting orientation of the thin film.

The FIB induced FCC structure was first characterized with TKD by including the reference file for FCC aluminum (Al), in addition to HCP α-Ti, BCC β-Ti, γ-TiO, and TiO_2, during the data collection and analysis. These additional reference files were added as most of TKD maps could not be fully indexed as HCP α-Ti despite the detection of clear and well-defined Kikuchi band patterns. It was found that only HCP α-Ti and the FCC-Ti structure were detected with reasonable confidence, i.e. only data points with confidence indices ≥ 0.2 were included in all EBSD and TKD orientation and phase maps. TKD orientation and phase maps and TEM-SAD micrographs of a mechanically compressed and FIB-thinned R3 micropillar is presented in Figure 2.2.

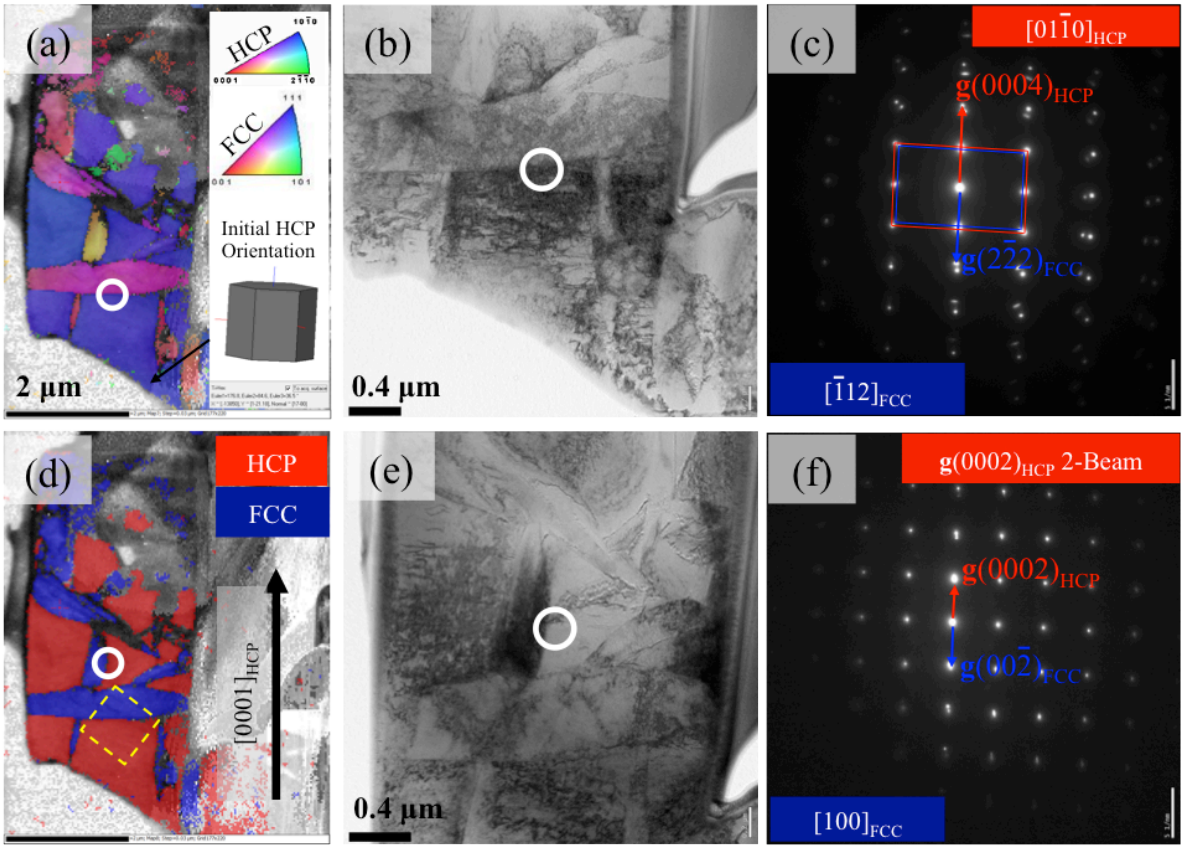

Figure 2.2: (a) and (d) are, respectively, TKD orientation and phase maps of a partially transformed $[0\ 0\ 0\ 1]_{HCP}$ oriented R3 pillar, thinned to electron transparency via FIB for TKD and TEM. (b) and (e) are brightfield TEM images corresponding to (c) and (f) SAD patterns, respectively. The white circles in (a) through (e) indicate the approximate size and location of the SAD aperture. The yellow dotted square in (d) indicates the approximate size and location of the EDS HAADF STEM image in Figure 2.4.

All R3 pillars, as well as all R2 and R4 pillars, were oriented for microcompression along the $[0001]_{HCP}$. This targeted orientation resulted in *near* prism surface normal directions for the FIB-thinned films. For example, the initial HCP direction normal to the surface of the thinned pillar shown in Figure 2.2 was indexed as $[17\bar{8}0]_{HCP}$, which is approximately ± 7° from the $[01\bar{1}0]_{HCP}$ about the $[0001]_{HCP}$. Two HCP-FCC orientation relationships were observed in the dual phase pillar presented in Figure 2.2:

1) $(002)_{FCC} \parallel (0002)_{HCP}$, $[1\bar{1}0]_{FCC} \parallel [01\bar{1}0]_{HCP}$
2) $(1\bar{1}1)_{FCC} \parallel (0002)_{HCP}$, $[\bar{1}12]_{FCC} \parallel [01\bar{1}0]_{HCP}$ (also $[110]_{FCC} \parallel [11\bar{2}0]_{HCP}$)

Interestingly, only the horizontal FCC lathes, i.e. long side nearly perpendicular to $[0001]_{HCP}$, demonstrated the conventional close-packed $(1\bar{1}1)_{FCC} \parallel (0002)_{HCP}$ relationship, while vertical lathes primarily exhibited the $(002)_{FCC} \parallel (0002)_{HCP}$ relationship. The stable FCC δ-TiH_2 hydride and the metastable FCT γ-TiH_x ($x<0.67$) hydride are also known to exhibit these $\{0002\}_{HCP} \parallel \{11\bar{1}\}_{FCC}$ and $\{0002\}_{HCP} \parallel \{002\}_{FCC}$ configurations [63–67], which suggests that the FIB induced FCC Ti phase are Ti hydrides. However, an orientation preference for the HCP to FCC

transformation was observed, which is the common argument against hydride nucleation for several FCC Ti investigations [34–40, 45–48]. It was discovered that all pillars oriented for c-axis compression had either fully or partially transformed from the parent HCP phase to an FCC structure upon FIB thinning to electron transparency. Conversely, little to no FCC Ti was detected in the R1 micropillars, which were oriented for *in situ* compression along a prism axis and exhibited a *near* basal surface normal direction. Figure 2.3 presents the orientation and phase TKD maps for a mechanically compressed and thinned R1 micropillar with a surface normal direction of $[01\bar{1}6]_{HCP}$, which is approximately ±10° from the $[0001]_{HCP}$ about the $[\bar{2}110]_{HCP}$.

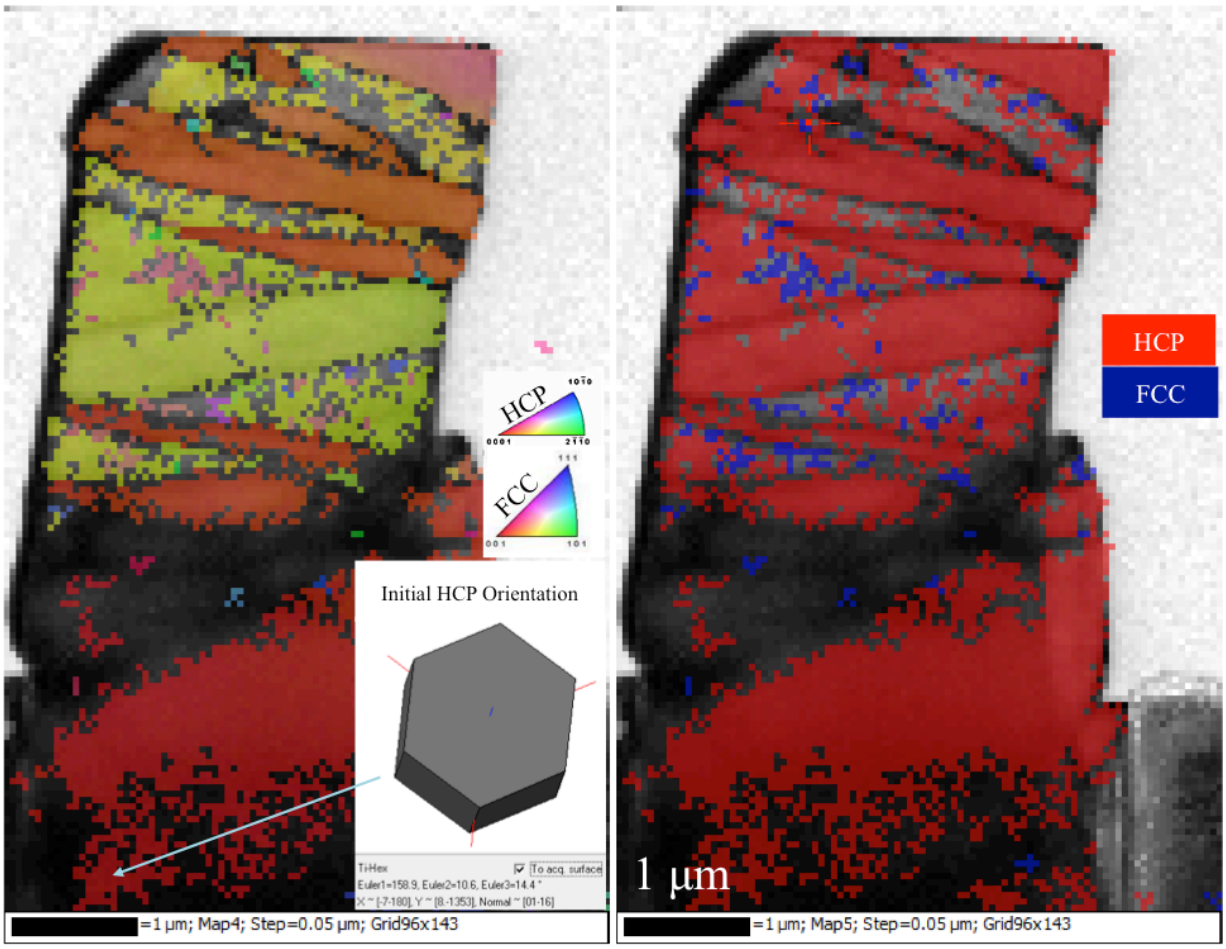

Figure 2.3: TKD orientation and phase maps of a round 1 (R1) pillar that was mechanically compressed *in situ* SEM and thinned to electron transparency with a FIB. This pillar was initially single crystalline and entirely HCP α-Ti prior to mechanical testing and thinning. The initial microstructure is indicated by the inset in (a) and shows a near basal surface plane orientation of the resulting thinned film. The blue regions in (b) were indexed as FCC Al indicating the presence of some FIB induced FCC Ti. Very little FCC structure was detected from the thinned S1 pillars (i.e. close packed surface plane oriented) relative to the thinned R2, R3, and R4 micropillars (i.e. prism surface plane oriented). This suggested that the formation of the FIB induced FCC Ti phase was preferential for prism film orientations and/or a $[0001]_{HCP}$ milling direction of the ion beam during thinning.

Unlike the R2, R3, and R4 micropillars, very little of the FCC structure was observed in the thinned R1 micropillars. This suggested that the FIB induced HCP to FCC transformation in α-Ti was influenced by either the surface plane orientation of the film, (i.e. more favorable for prism vs. basal (close-packed) oriented surfaces), or the direction of the ion beam relative to the initial HCP Ti single crystal orientation, (i.e. more favorable when aligned parallel to the $[0001]_{HCP}$ and incident to the basal plane), or a combination of the two. The dependence of thin film crystallographic orientation on the propensity for FCC Ti formation has been widely observed throughout the literature [13–26, 34–49]. Most notably, several accounts of an HCP to FCC transformation within α-Ti layers in Ti-Al, -Ag, and -Ni multilayers [34–49] have occurred under highly similar orientation and milling conditions and report comparable FCC lattice parameters as the current investigation.

The lattice parameter of the FIB induced FCC Ti structure ($a_{FIB\text{-}FCC}$) was determined from dual phase HCP + FCC thinned pillars, as shown in Figure 2.2, by measuring the distances of FCC SAD reflections relative to the known HCP SAD reflections of assumed HCP α-Ti lattice parameters a_{HCP} = 2.95Å and c_{HCP} = 4.68Å [1]. By this method, $a_{FIB\text{-}FCC}$ was found to be 4.40 ± 0.05Å, which is very similar to the lattice parameter of δ-TiH_2 ($a_{\delta TiH2}$ = 4.4Å) [77]. However, an FCC lattice parameter of this size corresponded to a 20% volume expansion from the initial HCP α-Ti matrix. An expansion of this magnitude was not expected to be energetically favorable and suggests the presence of additional atomic species within the FCC Ti lattice. Table 1.2 (presented again for convenience) lists several impurity-driven and FCC-like Ti-compounds that were suspected to be responsible for this anomalous FCC Ti phase.

Table 1.2: Lattice parameters for a few Ti compounds that form FCC-like structures [20, 27].

Ti Compound [TiX]	Composition [at.% X]	Prototype Phase	Lattice Parameters [Å]
TiC	~32−48.8	NaCl	a_{TiC} = 4.33
TiN	28 to > 50	NaCl	a_{TiN} = 4.24
γ TiO	34.9−55.5	NaCl	a_{TiO} = 4.29
TiGa*	40.5−50	AuCu	a_{TiGa} = 3.97
δ hydride	60−66.7	CaF_2	$a_{\delta H}$ = 4.45
ε hydride	> 66.7	ThH_2	$a_{\varepsilon H}$ = 4.5 | $c_{\varepsilon H}$ = 4.3 | $c_{\varepsilon H}/a_{\varepsilon H}$ = 0.96
γ hydride*	44−50	…	$a_{\gamma H}$ = 4.2 | $c_{\gamma H}$ = 4.6 | $c_{\gamma H}/a_{\gamma H}$ = 1.09

All of the Ti-compounds listed in Table 1.2 required a significant amount of the solute atomic species to stabilize under ambient conditions (nearly a 1:1 ratio for most). Therefore, EDS was conducted across the HCP-FCC boundary (see Figure 2.4 and Table 2.2) to qualitatively assess whether any suspect solutes (namely O, C, N, and Ga) demonstrated a clear preference for the FCC phase.

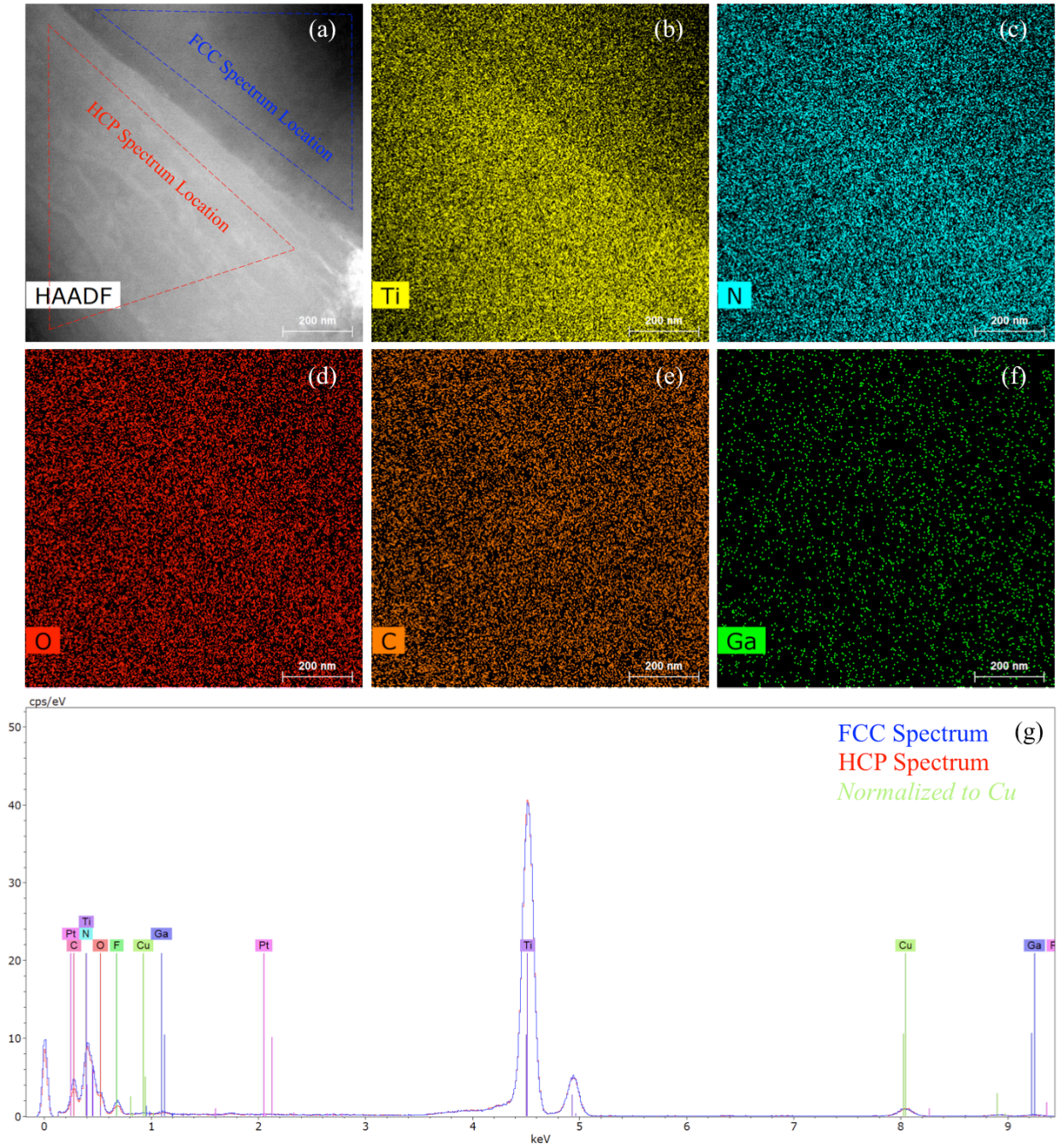

Figure 2.4: (a) TKD phase map of a R3 (initially) single crystalline high-purity α-Ti pillar that was thinned to electron transparency after compression with a FIB. (a) EDS HAADF STEM image of the HCP-FCC boundary outlined by the yellow dotted square in Figure 2.2(d). The regions outlined by the red and blue dotted lines in (a) correspond to the HCP and FCC spectra in (g). Chemical content estimations of the HCP and FCC spectra locations are presented in Table 2.2. (b) through (f) are the Ti, N, O, C, and Ga EDS elemental maps of (a). (g) EDS spectra of the HCP and FCC regions outlined in (a) and were normalized with respect to Cu (i.e. Cu signal was assumed to generate from the 3mm half grid supporting thinned micropillar). The detection of Ga, Pt, and F in the spectra was assumed to be due to residual contamination from the sample preparation process.

Table 2.2: Chemical content estimates of the HCP and FCC regions outlined in Figure 2.4(a).

Spectrum Location	**Estimated Chemical Content [Atomic %]** *Cu Deconvolution*						
	Ti	**O**	**C**	**N**	**Ga**	**Pt**	**F**
HCP	69.5%	4.01%	23.3%	0.580%	0.307%	0.0220%	2.21%
FCC	62.8%	4.07%	28.4%	1.34%	0.410%	0.00983%	3.04%

Due to the difficulties in measuring x-rays generated by light elements (i.e. atomic number below 11) [78–79], the chemical compositions of the HCP and FCC phases listed in Table 2.2 were not trusted to be accurate. However, these results did not qualitatively indicate any significant increase in O, C, N, and Ga contents within the FCC phase relative to the HCP phase. The strongest contrast across the HCP-FCC boundary was acquired from the Ti elemental map, which was most likely a consequence of the HCP side of the boundary being oriented slightly more on zone axis than the FCC side. Therefore, it was concluded from the above EDS results that FIB induced FCC Ti was definitely not TiGa, and TiC, TiN, and TiO could be disregarded due to the evidential lack of any solute segregation. In addition, these Ti-compounds were deemed far less likely candidates than the δ-Ti hydride (TiH_2) due to the strong similarity between the FIB induced FCC Ti and TiH_2 lattice parameters. To check for hydride contamination, the R4 pillars were heated *in situ* TEM to 350°C and held for approximately 30 minutes, i.e. above the eutectic temperature in the Ti-H binary phase diagram (see Figure 2.5). Figure 2.6 and Figure 2.7 summarize the before and after *in situ* heating TKD and TEM-SAD results for two individual R4 micropillars.

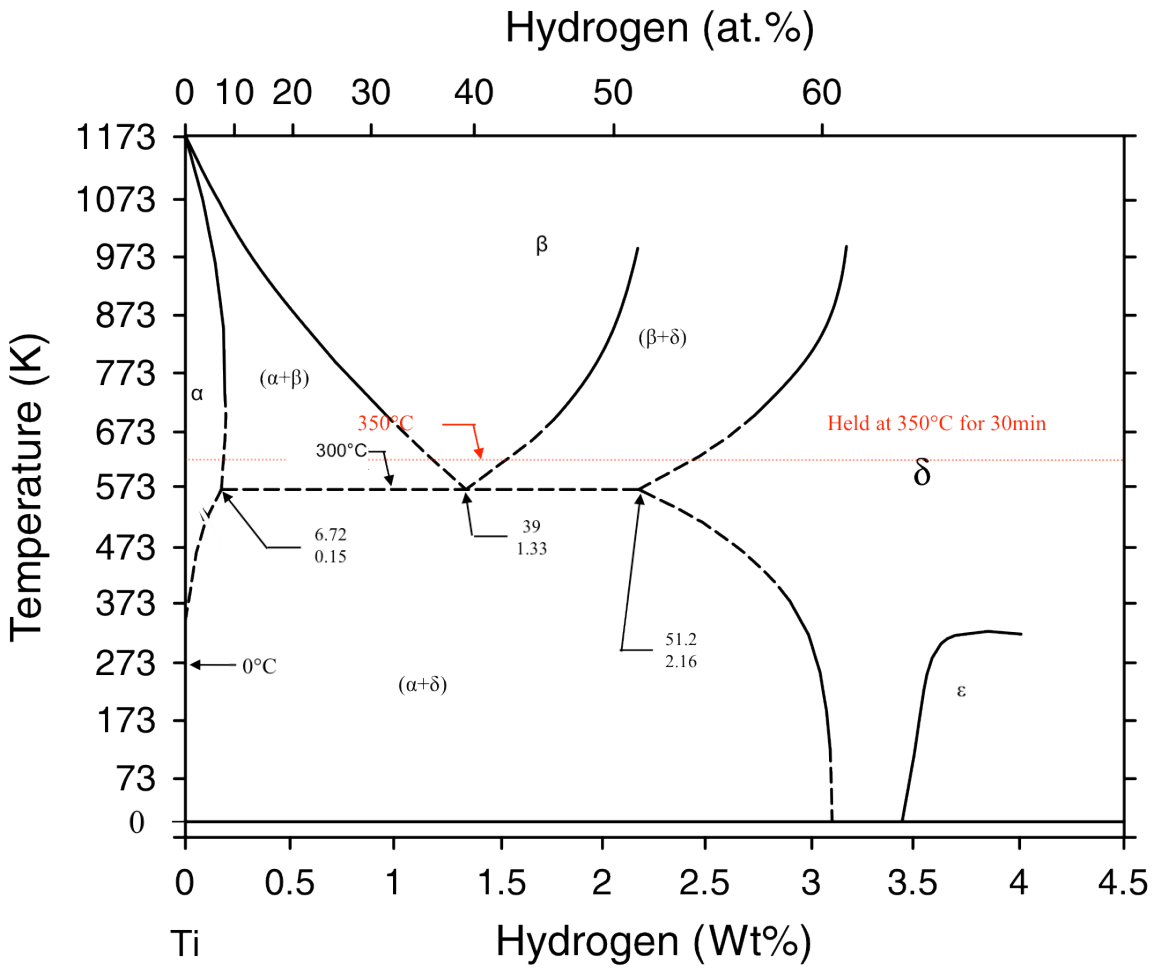

Figure 2.5: Ti-H binary phase diagram adapted S. Banerjee *et al*. (2007). *Phase Transformations: Examples from Titanium and Zirconium Alloys, First Ed*. p. 723. [3]. The FIB induced FCC Ti pillars were heated approximately to 350°C (red dotted line) *in situ* TEM and held for 30 minutes before cooling back to room temperature.

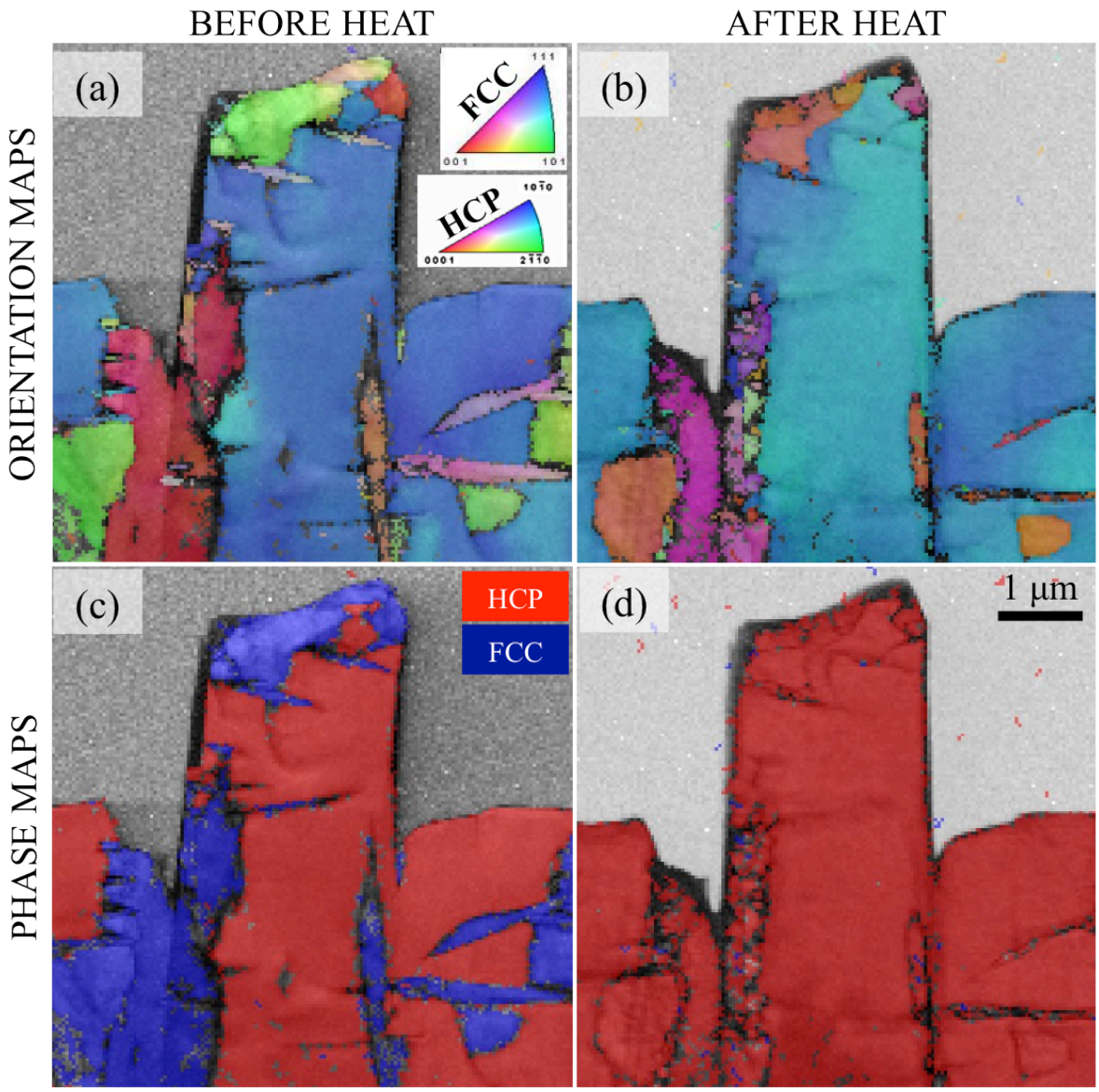

Figure 2.6: The before and after heat TKD orientation and phase maps of a partially transformed (HCP+FCC) R4 micropillar showing the disappearance of the FCC phase after heating to 350°C (for > 0.5hr) *in situ* TEM.

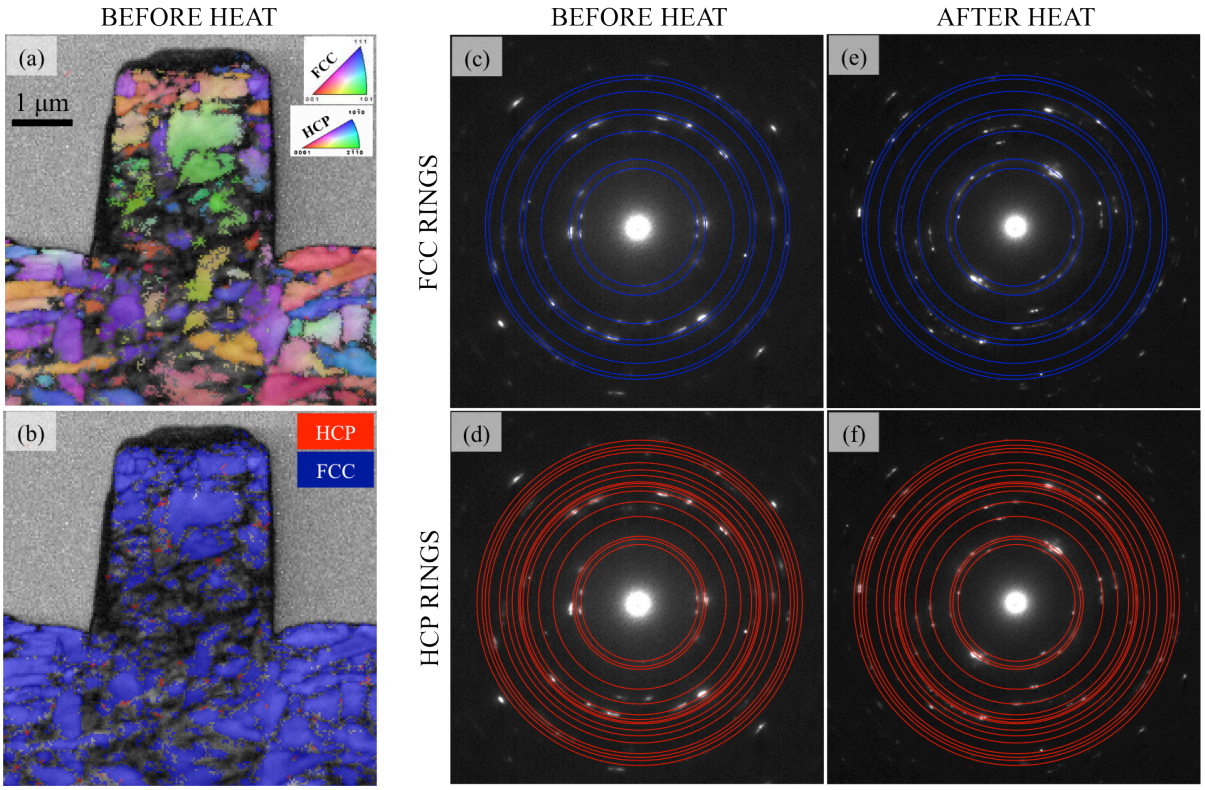

Figure 2.7: (a) and (b) are, respectively, the TKD orientation and phase maps of an entirely transformed FCC polycrystalline Ti R4 pillar prior to heating *in situ* TEM. A good quality post-heat TKD pattern could not be acquired from the particular pillar shown in (a) and (b). (c) through (f) are the before and after heat polycrystalline TEM SAD patterns overlaid with FCC (blue) and HCP (red) rings that confirm the disappearance of the FCC structure upon heating. The ring patterns were generated in R and match the d_{hkl} relative spacings of the FCC and HCP lattice. Note that (c) and (d) are the same SAD pattern but with different overlaid rings (likewise for (e) and (f)).

Both TKD and TEM show the reversion of FIB induced FCC Ti structure back into the stable HCP α-Ti phase upon *in situ* TEM heating. The dissolution of hydrides around 300°C during *in situ* heating in the electron microscope has been previously reported [62]. This FCC to HCP thermally driven reverse transformation strongly suggests that the FIB induced FCC Ti is in fact a type of hydride (δ-TiH_2 and/or γ-TiH). By the same logic, thermally induced FCC Ti was concluded to *not* be a variant of titanium hydride as it nucleated during *in situ* TEM heating at temperatures greater than 600°C.

2.3. Conclusion

A face-centered cubic structure of titanium has been widely reported since its discovery in 1969 [13]. The FCC Ti phase does not appear on any equilibrium phase diagram, however, the FIB induced FCC Ti variant discussed in the current chapter was found to be stable after formation. Analytical S/TEM and *in situ* investigations were implemented to deduce the chemical nature of this anomalous FIB induced FCC Ti phase. The results presented in this chapter suggest that FIB-induced FCC Ti is a form of titanium hydride (δ-TiH_2 and/or γ-TiH) based on the following:

- A HCP to FCC transformation was induced in high purity Ti micropillars during FIB thinning to electron transparency for TEM and TKD chemical and microstructural assessment.
    - TEM SAD on dual HCP-FCC phase thinned micropillars was implemented to evaluate the FIB FCC lattice parameter (4.40 ± 0.05Å), and is very similar to the reported of δ-TiH_2 lattice parameter ($a_{\delta TiH2}$ = 4.4Å) [75].
    - TKD and TEM show that FIB FCC Ti adopts the same two distinct HCP-FCC orientation relationships that are commonly found for the stable FCC δ-TiH_2 hydride and the metastable FCT γ-TiH_x (x<0.67) hydride [60–65]:
        - $(002)_{FCC} \parallel (0002)_{HCP}$, $[1\bar{1}0]_{FCC} \parallel [01\bar{1}0]_{HCP}$, and
        - $(1\bar{1}1)_{FCC} \parallel (0002)_{HCP}$, $[\bar{1}12]_{FCC} \parallel [01\bar{1}0]_{HCP}$ (also $[110]_{FCC} \parallel [11\bar{2}0]_{HCP}$)
    - EDS did not qualitatively indicate any significant increase in O, C, N, and Ga contents within the FIB FCC phase relative to the HCP phase and TiGa, TiC, TiN, and TiO were disregarded as possible candidates for the FIB induced case.
    - The disappearance of the FCC phase due to *in situ* TEM heating to temperatures greater than 300°C indicated that the FIB induced FCC Ti phase was Ti hydride [60].

Chapter 3. FCC Ti Type II
The Thermally Induced Case

A thermally induced HCP to FCC structural transition was first observed by Yu *et al*. (2017) [12] in high purity α-Ti TEM foils during *in situ* TEM heating experimentation. This transformation was successfully replicated on multiple occasions in the present study for the Ti-0.1O alloy. It should be noted that the TEM samples evaluated by Yu *et al*. (2017) [12] and those found in the current investigation were both cut from the same Ti-0.1O ingot listed in Table 2.1 (presented again for convenience), followed similar TEM sample preparation methodologies, and were fabricated and characterized using the same tools and facilities available at NCEM, LBNL. It should also be mentioned that *in situ* TEM heating of Ti-0.3O TEM samples (see Table 2.1) produced identical results, however, no chemical investigations were conducted on Ti-0.3O samples. As was the case for FIB induced FCC Ti, only the Ti-0.1O system is considered for investigations into thermally induced FCC Ti.

Table 2.1: Bulk chemical compositions (in both wt.% and at.%) of all Ti-alloys use in this study, as provided by TIMET Inc. (alloy supplier).

		Al	V	Fe	C	N	O	Ti
Ti-0.1O	[wt.%]	0.005	0.003	0.005	0.003	0.007	0.114	99.9
	[at.%]	0.009	0.003	0.004	0.012	0.024	0.340	99.6
Ti-0.2O	[wt.%]	0.005	0.003	0.006	0.006	0.004	0.207	99.8
	[at.%]	0.009	0.003	0.005	0.024	0.014	0.617	99.3
Ti-0.3O	[wt.%]	0.005	0.003	0.004	0.009	0.001	0.292	99.7
	[at.%]	0.009	0.003	0.003	0.036	0.003	0.868	99.1

3.1. Specimen Preparations and Characterization

The *in situ* heated TEM samples were prepared as follows. First, slices of around 500-1000μm thicknesses were cut from the bulk material using a Struers Inc. diamond saw (Secotom-10). Next the slices were manually thinned down to approximately 100-200μm thick foils with sequentially finer grit silicon carbide (SiC) papers, ending with P-4000 as a final step. The SiC papers were affixed to a 200mm diameter revolving grinding-polishing wheel (operated at ≤160 rpm), and water was continually applied to prevent frictional heating of the sample. This manual thinning methodology was applied evenly to both flat surfaces of every slice. 3mm diameter discs were then cut from the polished slices with the same abrasive slurry disc cutter mentioned previously. All burrs and sharp edges were smoothed away with P-4000 SiC paper and each sample was carefully, and thoroughly, cleaned with Kimwipe microfiber cloths in acetone to remove any residual adhesive. Next, the samples were electrochemically polished and thinned to electron transparency with a Fischione Twin Jet Electropolisher (Model 110) polishing apparatus (controlled by a Fischione Model 120 Automatic Power Control unit). The polishing solution consisted of 94% methanol, ~423mL, and 6% perchloric acid (60% concentrated so approximately 3.6% pure perchloric acid), ~27mL. It should be noted that perchloric acid was added to methanol only when the methanol reached ≤ -30°C in an effort to slow the exothermal

reaction [60]. The polishing solution was cooled within the jet polisher, via conduction, with coolant methanol and liquid nitrogen. The temperature of the polishing solution was checked frequently and liquid nitrogen was added to the coolant reservoir as needed. Electrochemical polishing was carried out at approximately -40°C in order to minimize the amount of hydrogen absorbed by the sample [60]. Voltages of around 26–30V and currents of 13–16mA, yielded a good quality polish after approximately 2.5–4.5 min. Power was cut to the jet polisher and polishing was ceased as soon as a hole was detected by the polishing apparatus, via a light sensor, and each disc was carefully rinsed in methanol followed by ethanol to remove any residual etchant. The polishing solution used by Yu *et al*. (2017) [12] (6% perchloric, 39% butanol, and 55% methanol maintained at -30°C) was also implemented in the present study and yielded similar results. Each sample was checked in an optical light microscope and only samples of the highest quality, i.e. smooth polish around a relatively centered hole with no evidence of acid or solvent residue, pitting, preferential grain or grain boundary etching, or coloration due to oxidation, were used for *in situ* TEM heating experimentation.

The selected TEM samples were slowly heated *in situ*, from room temperature to ≥ 600°C. The temperature ramp rate was set to 1°C/sec, however, heating was periodically paused to allow for easier observation of the evolving microstructure and stabilization of the temperature throughout the film. A majority of the TEM samples tested were cooled rapidly, typically by shutting off the current running through the holder, as it became apparent during the first few *in situ* TEM heating experiments that cooling rate had no noticeable influence on the FCC structure. All *in situ* heating experiments were performed on the NCEM 300kV JEOL 3010 TEM and the FEI TitanX 300kV TEM/STEM mentioned previously, as well as a 200kV JEOL 2100 field-emission analytical TEM equipped with a Gatan Tridiem electron energy loss spectrometer (EELS). A Gatan recirculating pump was connected to the TEM heating holders for *in situ* heating experiments greater than 500°C.

In situ TEM heating coupled with EELS was performed to assess the oxygen contents of the HCP and FCC phases soon after FCC nucleation and while under vacuum. As these results remained inconclusive, largely due to surface oxide interference, sections of *in situ* heated TEM samples that contained FCC Ti were lifted out and thinned for through-thickness, i.e. cross sectional, TEM and EDS evaluations. Cross-sectional samples were made with a similar methodology as the micropillar liftouts, though lower starting FIB currents were used as the samples required very little milling. The heated APT samples, or ‘tips’, were also made using similar but adapted liftout methods for additional chemical investigations into this anomalous FCC Ti phase (see Figures 3.1). The control tips were made using a Zeiss Ga^+ FIB/SEM and a W^+ ion deposited adhesive (instead of Pt) according to the method illustrated in Figure 3.2.

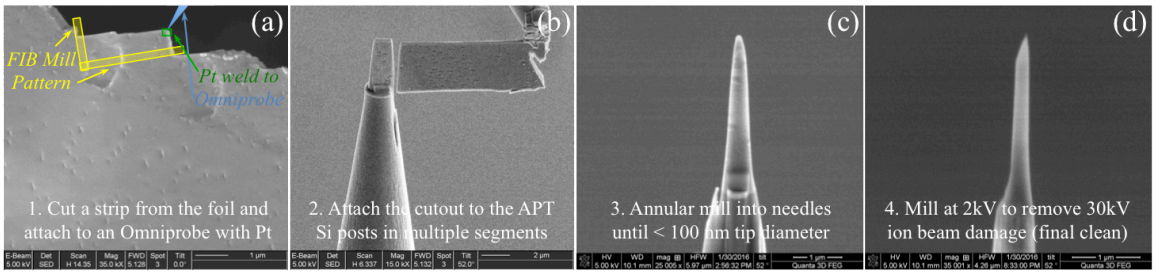

Figure 3.1: APT sample preparation method for *in situ* heated TEM foils. Note that this method is similar to conventional lift outs (see Figure 3.2) and involves: 1) lifting out a strip of thin material from a TEM sample (approximately 5-6μm wide x 15-20μm long), 2) attaching the cutout to the side of a Cu post (3mm half-disc) so that SEM electron beam is incident to cutout flat surface (at 0° stage tilt) and the long axis of cutout extends away from the Cu post and is in plane with the 3mm half-disc, 3) venting the FIB/SEM and manually rotating the Cu half-disc 90° (SEM electron beam now parallel to cutout flat surface at 0° tilt), 4) lifting the cutout strip again and attaching/sectioning it to the APT posts (cutouts standing upright), and 5) following the conventional annular milling APT tip shaping procedure [82].

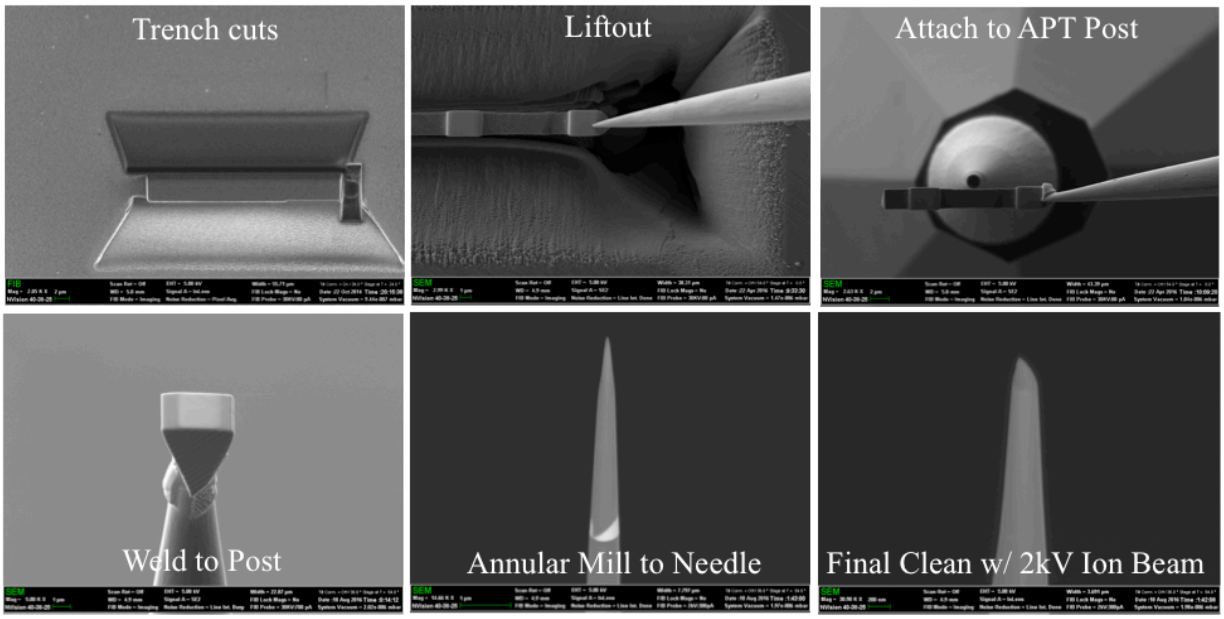

Figure 3.2: Conventional APT sample preparation method [82]. Note that control APT tips were fabricated according to this methodology from a thick region of a non-heated Ti-0.1O TEM foil.

3.2. Results and Discussion

The thermally driven HCP to FCC structural transition, via *in situ* TEM heating, recently reported by Q. Yu *et al*. (2017) [12] was successfully replicated in high purity Ti-0.1O TEM foils in the present study. As was shown by Yu *et al*. [12], this thermally induced FCC Ti was observed to nucleate around ~600°C and had strong directionality in growth. However, the thermal FCC Ti observed in the current investigation grew to larger overall sizes (ranging 20-150nm in width and 50-300nm in length) than those observed by Yu *et al*. [12] (48nm in width and 72nm in length). This size variation was due to continued heating for longer time intervals

and at a higher maximum temperature as the sample in Figure 3.3 was heated to approximately 700°C. Interestingly, it was found that the thermally-driven HCP to FCC transformation was highly dependent on the crystallographic orientation of the TEM foil and was only observed within prism oriented surface grains (i.e. when the $[0001]_{HCP}$ axis lay in plane with thin film).

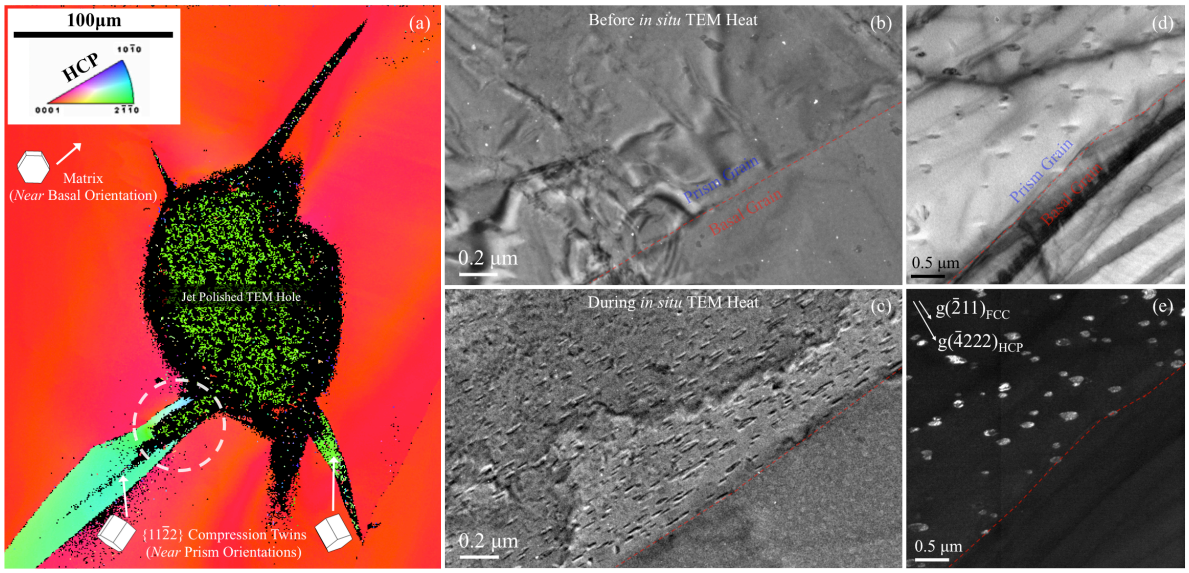

Figure 3.3: (a) EBSD orientation map of a Ti-0.1O TEM foil that was heated to approximately 700°C. The dashed white circle indicates the approximate locations of (b) through (e). (b) and (c) present snapshots from the *in situ* TEM heating movie showing the same area of the sample prior to and during *in situ* TEM heat, respectively. (d) and (e) are complementary TEM brightfield and darkfield micrographs high lighting the thermally induced FCC phase. Note that the FCC phase only appears within the prism orientated grain.

The TEM foil shown in Figure 3.3 was presumed to be entirely basal oriented (i.e. colored red in the EBSD orientation map) prior to jet polishing, and the force of the jets (aligned in compression along the $[0001]_{HCP}$) induced a $\{11\bar{2}2\}_{HCP}$ $\langle 1\bar{1}00\rangle_{HCP}$ type compression twin (colored green). This effectively resulted in a *nearly* prism-oriented grain within the foil where the thermally induced FCC phase was exclusively observed to nucleate during *in situ* TEM heating, as no FCC structures were found within the surrounding basal oriented grain.

The thermal FCC Ti lattice parameter ($a_{Thermal\text{-}FCC}$) was measured from TEM-SAD patterns (see Figure 3.4) to be 4.20 ± 0.07Å by the same method previously described for the FIB induced FCC hydride. In addition, HRSTEM micrographs of the HCP-FCC boundary (see Figure 3.5) showed a close-packed arrangement between the HCP and FCC phases, i.e. $\{0002\}_{HCP}$ parallel to $\{11\bar{1}\}_{FCC}$, and the thermal FCC lattice parameter was again measured to be 4.19 ± 0.03Å from fast Fourier transforms (FFTs) of the HRSTEM micrographs for confirmation.

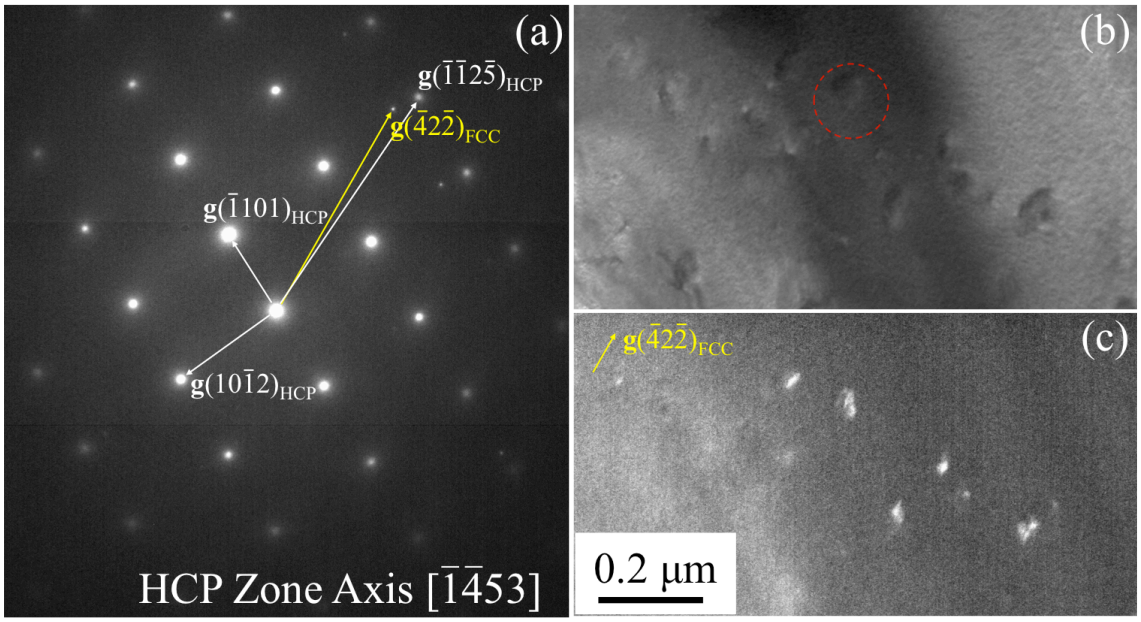

Figure 3.4: (a) SAD pattern acquired from an FCC precipitate marked by the red dashed circle in (b). (b) and (c) are the TEM bright and dark field images corresponding to (a). A FCC lattice parameter of 4.20 ± 0.07Å was approximated by measuring the distances of FCC SAD reflections relative to the known HCP SAD reflections of assumed HCP α-Ti lattice parameters a_{HCP} = 2.95Å and c_{HCP} = 4.68Å [1].

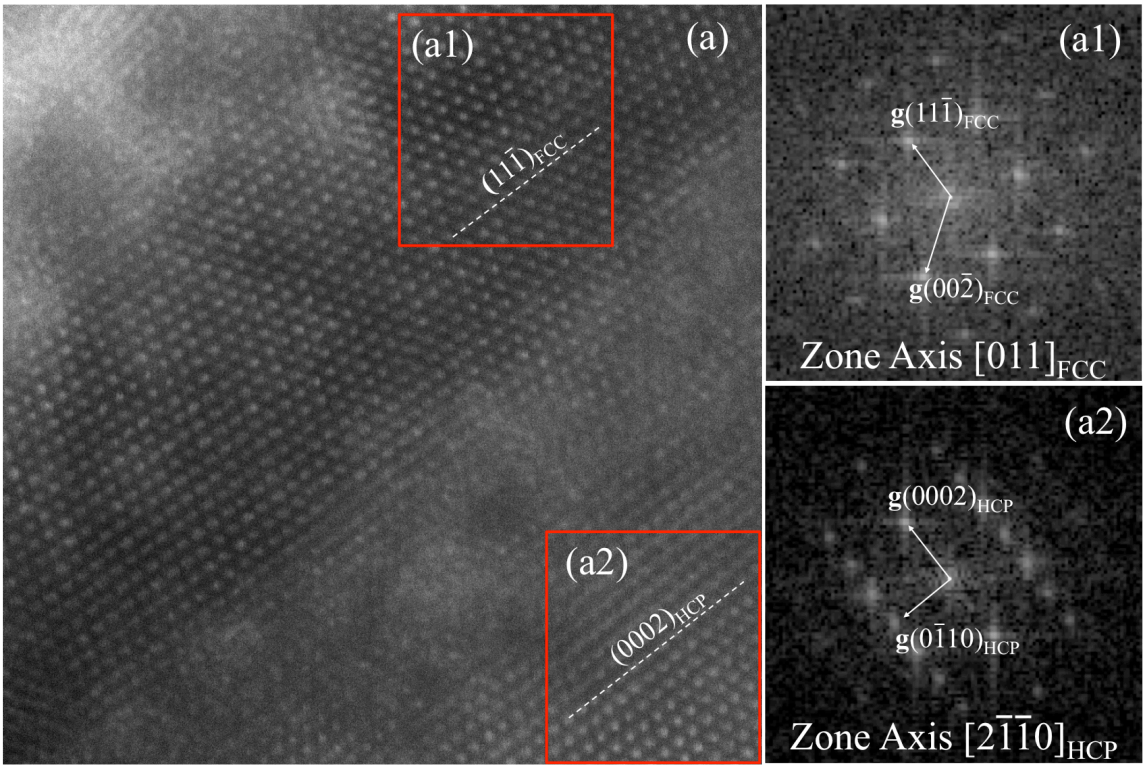

Figure 3.5: (a) HRSTEM micrograph of a HCP-FCC boundary. (a1) and (a2) are FFTs acquired from the FCC and HCP regions outlined in red in (a) and correspond to the $\langle 011\rangle_{FCC}$ and $\langle 2\bar{1}\bar{1}0\rangle_{HCP}$ zone axes, respectively.

The thermal FCC Ti lattice parameter was found to be slightly larger than that of Yu *et al*. [12] ($a_{Thermal\text{-}FCC}$ = 4.12 ± 0.03Å). As was previously mentioned in regards to thermal FCC Ti size distribution, the *in situ* TEM heated foil in Figure 3.3 likely reached a higher maximum temperature and/or was held at high temperature for longer amounts of time. These (speculated) differences in foil thermal history and the high reactivity of Ti with O [1] suggested that this discrepancy in the FCC phase overall size and lattice parameter were due to the prolonged absorption of oxygen into the TEM foil. As such, the primary FCC-based Ti-impurity suspected for thermally induced FCC Ti was γ-TiO (a_{TiO} = 4.29 Å, see Table 1.2). EELS, EDS, and APT were conducted on the same TEM foil shown in Figure 3.3 to assess the oxygen content of this thermally nucleated FCC phase relative to its parent HCP phase.

EELS was performed in TEM mode (operated at 120kV) both before and after thermal FCC Ti nucleation and prior to the removal of the sample from the TEM, (i.e. without exposing the foil to air between *in situ* heating and chemical evaluation). The post-heat spectra were acquired after the sample had been cooled to room temperature.

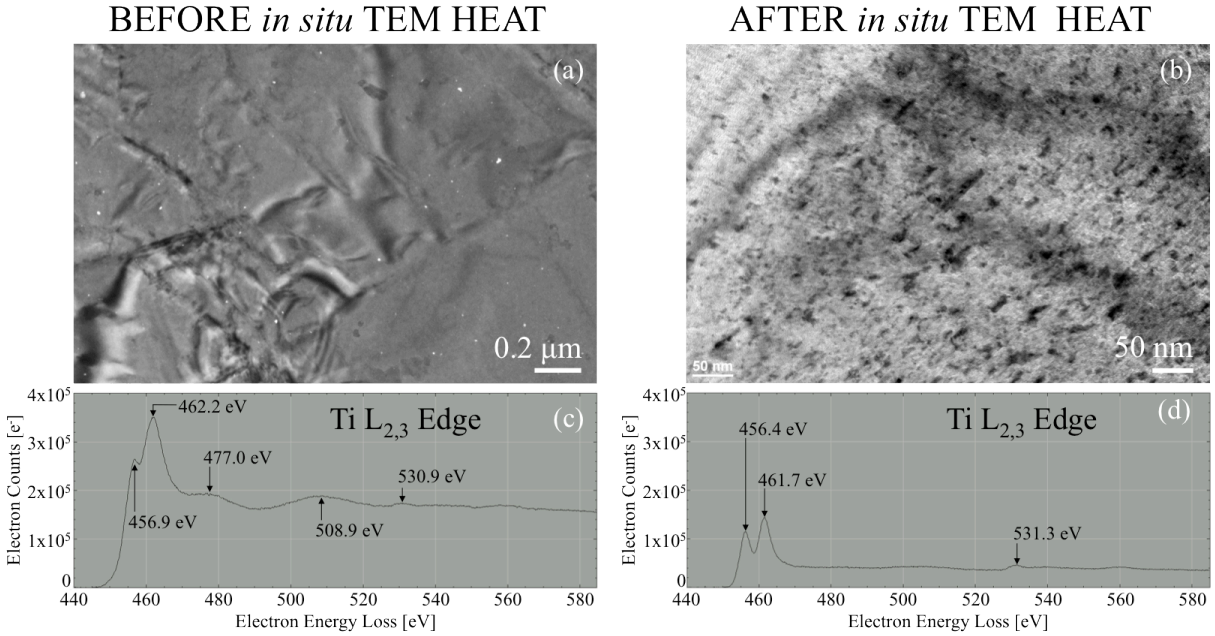

Figure 3.6: (a) and (b) are the before and after heat TEM bright field micrographs, respectively, of a Ti-0.1O TEM foil that precipitated a FCC Ti phase upon heating *in situ* TEM. (a) and (b) indicate the approximate region within the TEM foil from which EELS was conducted. (c) and (d) are the before and after heat $TiL_{2,3}$ EELS spectra, respectively.

The before and after *in situ* TEM heat Ti $L_{2,3}$ edge EELS spectra (presented in Figure 3.6) were acquired from different regions within the prism oriented twin and at different magnifications and aperture sizes. Therefore, little can be interpreted from the relative changes in peak heights before and after heating and the overall oxygen content (oxygen K edge located around 532 eV) could not be reliably quantified due to the high signal-to-noise ratio. However, the increase in the Ti L_2 edge relative to the Ti L_3 edge after heating may indicate an overall shift in the Ti charge state due to a change in atomic bonding (i.e. due to oxide formation). In addition, a ~0.5 eV shift

in the Ti $L_{2,3}$ peak positions upon heating was observed, which could also indicate some oxidation of the TEM foil [79]. Unfortunately due to the varying conditions by which the before and after heat spectra were acquired, even these inferences could be utilized to draw any concrete conclusions about thermally induced FCC Ti. Therefore EDS and APT was performed to supplement the EELS results.

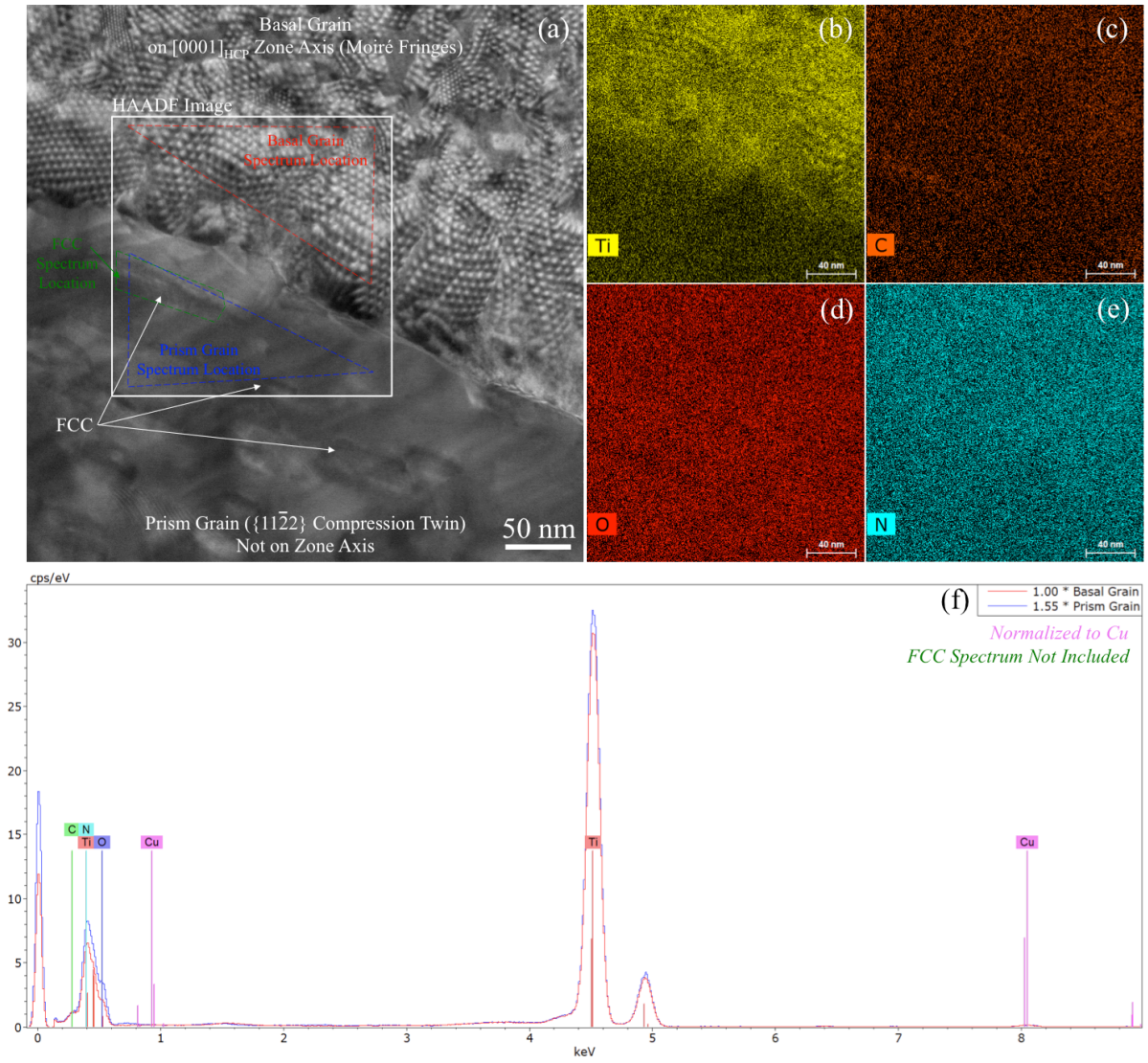

Figure 3.7: (a) STEM image of the $\{11\bar{2}2\}_{HCP}$ twin boundary from the sample shown in Figure 3.3 after *in situ* TEM heating. The basal grain was oriented along the $[0001]_{HCP}$ zone axis and contained Moiré fringes. The white box outlines the location of the HAADF STEM image and Ti, C, O, and N EDS elemental maps shown in (b) through (e), respectively. The regions outlined by the red, blue, and green dotted lines correspond to the spectra in (f) and are normalized with respect to Cu. Chemical content estimations of the spectra locations are presented in Table 3.1.

Table 3.1: Chemical content estimates of the entire HAADF image, basal grain, prism grain, and FCC precipitate region outlined in Figure 3.7(a).

Spectrum Location	**Estimated Chemical Content [Atomic %]** *Cu Deconvolution*			
	C	**N**	**O**	**Ti**
Entire HAADF Image	12.6%	1.79%	7.45%	78.2%
Basal Grain	13.5%	2.15%	5.68%	78.6%
Prism Grain	11.6%	1.07%	9.99%	77.4%
FCC	15.3%	1.44%	8.14%	75.1%

The EDS results presented in Figure 3.7 and Table 3.1 did not show a significant segregation of oxygen to the FCC phase. However, the presence of Moiré fringes in the basal oriented grain strongly suggested the epitaxial growth of a surface oxide. It was hypothesized that this surface oxide, combined with the limited reliability in EDS light element quantification, interfered with the oxygen signal and the values listed in Table 3.1 were not representative of the true oxygen content within the sample. To bypass the surface oxide, FIB strips were removed and thinned (liftout) for a cross-sectional EDS evaluation. However, fabricating these cross-sections was difficult and it became unclear as to whether any one of the ten prepared samples contained any thermally induced FCC precipitates. Only one cross-sectional cutout contained an FCC-like feature that could be imaged in TEM dark field mode using an FCC diffraction reflection. The EDS elemental maps and chemical content estimations for this cross-sectional sample are presented in Figure 3.8 and Table 3.2.

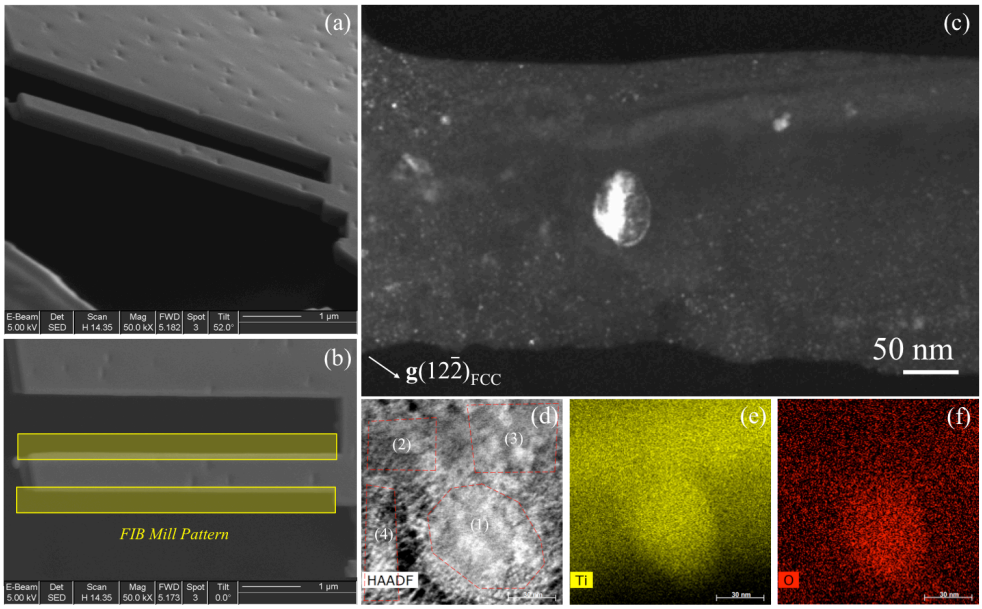

Figure 3.8: (a) and (b) are SEM micrographs of the same TEM sample in Figure 3.3. Cross sections of the TEM foil were prepared (via FIB liftout) for EDS. (c) TEM dark field micrograph highlighting an FCC feature within the cross sectional foil. (d) is a HAADF STEM image of the same FCC feature in (c). The dotted red polygons outline different regions where EDS spectra and chemical content estimations were acquired (see Table 3.2). (e) and (f) correspond to the Ti and O elemental EDS maps of (d), respectively.

Table 3.2: Chemical content estimates of the regions outlined by the red dotted polygons in Figure 3.8 (d). The bolded row was taken from the (assumed) thermally induced FCC Ti phase.

Spectrum Location	Estimated Chemical Content [Atomic %] *Cu Deconvolution*					
	Ti	O	C	N	Ga	Pt
(1)	**36.1%**	**15.5%**	**46.1%**	**0%**	**1.07%**	**1.31%**
(2)	48.4%	9.22%	33.9%	0%	5.82%	2.64%
(3)	51.0%	10.3%	31.5%	0%	5.64%	1.60%
(4)	28.6%	9.97%	56.5%	0%	1.28%	3.61%

Higher levels of oxygen were detected from this FCC feature relative to the surrounding HCP regions. However, due to *severe* carbon contamination and the tendency for high purity Ti to form hydrides due to FIB milling (i.e. FIB induced FCC Ti), this FCC feature could not be confidently identified as thermally induced FCC Ti let alone γ-TiO. However, the EDS results were suggestive of excessive amounts of oxygen contamination. The most enlightening results with regard to thermally induced FCC Ti chemical content estimations were acquired with APT.

APT was conducted on tips fabricated from the same sample shown in Figure 3.3 using a Cameca Local Electrode Atom Probe (LEAP) 5000XR operated in laser pulsed mode. Control tips were also tested for comparison. All APT experiments, or "runs", were carried out at 55K (-215.15°C) and were detection rate controlled, i.e. the voltage adjusted automatically to achieve the targeted detection rate. The target detection rate, laser pulse energy, and laser pulse frequency were adjusted (occasionally mid-run) to assist with the chemical evaluation and reconstruction analysis. The set values for the detection rate [%], laser pulse energy [pJ], and laser pulse rate [kHz] varied between 0.5%, 0.7%, 0.9%, and 1.0%, 50pJ and 100pJ, and 125kHz and 200kHz, respectively. Each APT experiment ran continuously until the APT sample, or "tip", fractured. Only seven out of the 22 APT tips tested generated approximately 2 million or more (detected) ions and were considered in the chemical content estimations. Two control tips were fabricated from a non-heated Ti-0.1O TEM sample using the conventional APT sample preparation method depicted in Figure 3.2, and five tips were fabricated from the *in situ* heated sample shown in Figure 3.3 using the thin foil method depicted in Figure 3.1. Due to known complications in evaluating Hydrogen in APT experiments the H peaks were disregarded [80–81]. However, the APT did show a clear inclusion of oxygen in the TEM-annealed samples, which supports the conclusion that oxygen inclusion inside the TEM (which is only a moderate vacuum) is linked to the formation of thermal FCC Ti (see Figure 3.9 and Tables 3.3 and 3.4).

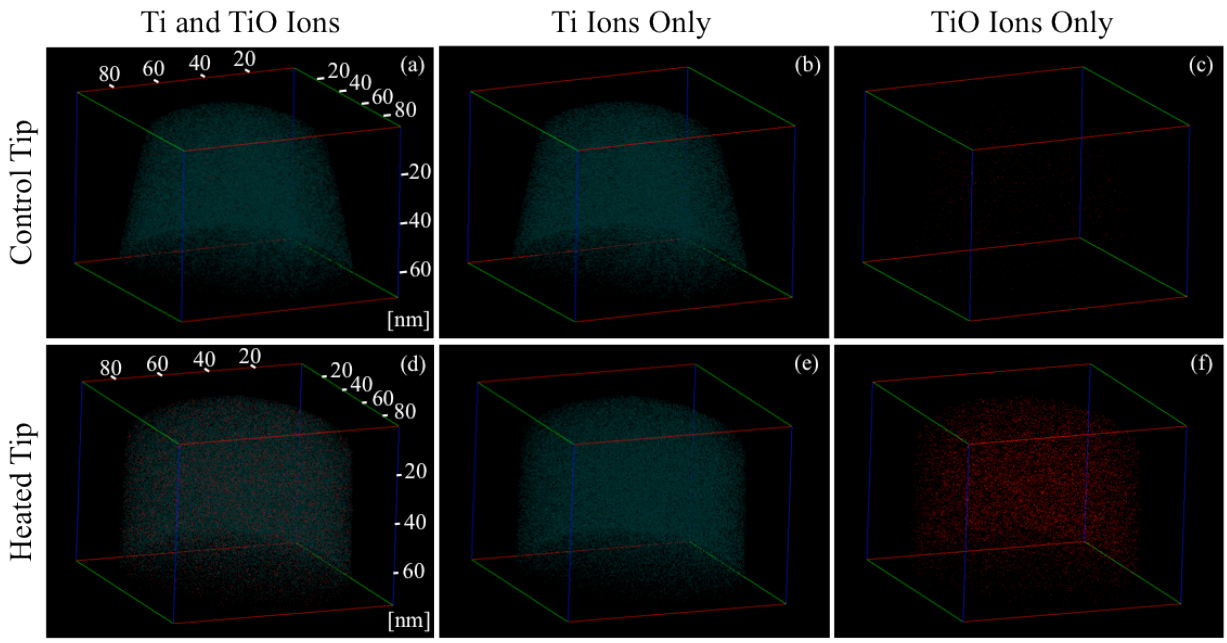

Figure 3.9: APT reconstructions for two tips (Note: 1 tip per row). Row 1 (i.e. a through c) and row 2 (d through f) are selected ion reconstructions of a control and heated APT tip, respectively. Column 1 (a and d), column 2 (b and e), and column 3 (c and f) are the Ti+TiO, Ti (only), and TiO (only) selected ion reconstructions for each tip. Note: only 2.5% of the selected ion in each reconstruction is shown. The chemical content estimates are presented in Tables 3.3 and 3.4.

Table 3.3: The estimated Ti, H, O, C, and N contents (in atomic %) for the two APT tip reconstructions shown in Figure 3.9. The bulk chemical content estimated by the alloy provider (TIMET Corp.) was listed for comparison. 'W' and 'I' refer to the estimated chemical contents of each tip reconstruction when considering all ions (decomposed into constituents) within the whole reconstruction (W) vs. all ions within a selected region of interest (ROI) within the tip interior (I), i.e. the interior values exclude the native oxide. The Ga content for each tip was measured at less than 0.004% and was therefore omitted from the table. These results are also provided in weight percent (wt.%) in Table 3.4.

Avg. Chemical Content x 100 [at.%]		**Ti**	**H**	**O**	**C**	**N**
***in situ* TEM Heated Tips**	W	88.9	1.92	7.67	1.22	0.256
	I	88.9	1.50	7.76	1.56	0.253
Control Tips (Not Heated)	W	94.8	4.38	0.521	0.0138	0.295
	I	95.7	3.66	0.406	0.0166	0.216
Nominal Bulk Content (Provided by TIMET)	-	*99.6*	-	*0.340*	*0.0119*	*0.0239*

Table 3.4: The estimated Ti, H, O, C, and N contents (in weight %) for the two APT tip reconstructions shown in Figure 3.9. The bulk chemical content estimated by the alloy provider (TIMET Corp.) was listed for comparison. 'W' and 'I' refer to the estimated chemical contents of each tip reconstruction when considering all ions (decomposed into constituents) within the whole reconstruction (W) vs. all ions within a selected region of interest (ROI) within the tip interior (I), i.e. the interior values exclude the native oxide. The Ga content for each tip was measured at less than 0.004% and was therefore omitted from the table. These results are also provided in atomic percent (wt.%) in Table 3.3.

Avg. Chemical Content x 100 [wt.%]		**Ti**	**H**	**O**	**C**	**N**
***in situ* TEM Heated Tips**	W	96.8	0.0439	2.79	0.332	0.0816
	I	96.6	0.0343	2.82	0.426	0.0806
Control Tips (Not Heated)	W	99.6	0.0969	0.183	0.00363	0.0907
	I	99.7	0.0803	0.142	0.00433	0.0658
Nominal Bulk Content (Provided by TIMET)	-	*99.9*	-	*0.114*	*0.00300*	*0.00700*

Taken together, the EDS, EELS and APT results suggest that a significant change in oxygen content occurred due to *in situ* TEM heating. In particular, the APT result shows an increase in oxygen content, from approximately 0.70 to 7.07 at.% O, due to *in situ* TEM heating. While γTiO is only predicted to be stable between 40-55. at.% O on the Ti-O binary phase diagram, it is possible that the thin foil effect of a TEM sample leads to the formation of γTiO of more moderate oxygen content. Interestingly, APT also suggests that the native oxide was absorbed by the sample during *in situ* TEM heating. As such, thermally induced FCC Ti was believed to be stabilized by oxygen and is an oxygen-rich (but still metallic) Ti alloy, i.e. similar to the alpha-case [75].

3.3. Conclusion

A face-centered cubic structure of titanium has been widely reported since its discovery in 1969 [13]. The FCC Ti phase does not appear on any equilibrium phase diagram, however, the thermally induced FCC Ti variant discussed in the current chapter was found to be stable after formation. Analytical and *in situ* S/TEM and APT investigations were implemented to deduce the chemical nature of this anomalous thermal FCC Ti phase. Though the thermally induced FCC Ti phase could not be confirmed to be γ-TiO, the results presented in this chapter do suggest that the HCP to FCC transformation observed during *in situ* S/TEM heating is accompanied by oxygen contamination.

- The thermally driven HCP to FCC transformation in high purity Ti TEM foils first reported by Q. Yu *et al*. (2017) [12] was successfully replicated the present study. A chemical and microstructural assessment of this anomalous FCC Ti phase was conducted.
    - The thermal FCC Ti lattice parameter was measured from both TEM-SAD patterns and HRSTEM micrographs to be 4.20 ± 0.07Å and 4.19 ± 0.03Å, respectively, which is slightly larger than previously reported by Yu *et al*. [12] ($a_{Thermal\text{-}FCC}$ = 4.12 ± 0.03Å). It is speculated that the differences in TEM foil thermal history and the high reactivity of Ti with O are responsible for discrepancy between the two studies and that this oxygen stabilized FCC Ti phase continues to getter oxygen and grow in lattice parameter over time, eventually becoming the metastable γ-TiO oxide (a_{TiO} = 4.29 Å).
    - Only the close-packed planar HCP-FCC orientation relationship was observed via TEM and HRSTEM for the thermal FCC Ti phase:
        - $(11\bar{1})_{FCC} \parallel (0002)_{HCP}$, $[011]_{FCC} \parallel [2\bar{1}\bar{1}0]_{HCP}$.
    - EDS, EELS, and APT were conducted on thermal FCC Ti, all of which show no clear segregation of oxygen to the FCC phase but do suggest that the sample increases in oxygen content due to *in situ* TEM heating. The most enlightening results into the chemical nature of thermal FCC Ti were from APT, which show the average oxygen content increased from approximately 0.70 at.%O in non-heated samples to 7.1 at.% O in *in situ* TEM heated samples. In addition, a native oxide was clearly observed in the control samples but was far less apparent in the heated APT samples, and this suggests that the TEM foil absorbed the native oxide during heating.
    - Thermal FCC Ti was found to nucleate only within prism oriented grains of the TEM foils during *in situ* TEM heating. The cause of this orientation dependence is currently unknown, though it is speculated that film surface energy, diffusivity of the film's native oxide at a given orientation and temperature, internal stresses built up in the foil due to alloy processing and sample preparation, and the transformation mechanism itself are some of the key conditions that dictate thermal FCC Ti nucleation.

Chapter 4. FCC Ti Type III
The Strain Induced Case

The objectives of this research were to structurally and chemically characterize the third experimentally found variant of FCC Ti and to elucidate the dislocation-mediated mechanism responsible for the HCP-to-FCC transformation. It was found that these "transformation" dislocations were **a**-type ($\vec{\mathbf{b}}=1/3\langle 11\bar{2}0\rangle_{HCP}$) and were the same type as those observed during planar slip in Ti-Al alloys (≤6 wt.% Al). The Ti-Al samples were aged to promote the short-range ordering (SRO) of the α_2 phase (Ti_3Al), which is known to promote planar-like over wavy-like dislocation slip. It is thought that type III FCC Ti nucleation was promoted in these aged alloys since deformation twinning is known to be suppressed in Ti-Al alloys (particularly when aged and show evidence of α_2 SRO) [83], thereby forcing the HCP lattice to adopt other mechanisms that accommodate strain along the c-axis. SRO and planar type dislocation slip may also promote FCC Ti nucleation by restricting slip to specific glide planes, which facilitate an ordered type of glide, i.e. what is often proposed as transformation mechanisms between phases in Ti. However, the relationship between the strain induced FCC Ti phase and Ti_3Al SRO was not specifically investigated.

4.1. Specimen Preparation and Characterization

A strain induced FCC Ti phase was observed in Ti-6Al and Ti-6Al-0.3O (wt.%) TEM straining bar samples that were aged to promote planar slip and the short-range ordering (SRO) of the α_2 (Ti_3Al) phase [83]. The alloy chemical contents and thermal history are provided in Table 4.1 and Figure 4.1, respectively. 0.5mm thick straining bar samples were cut (prior to thermal aging) to the dimensions depicted in Figure 4.2 with a wire electrical discharge machine (wire-EDM).

Table 4.1: Bulk chemical compositions (in both wt.% and at.%) of all Ti-alloys use in this study, as provided by TIMET (alloy supplier).

		Al	C	N	O	Ti
Pure Ti	[wt.%]	-	-	-	0.054	99.9
	[at.%]	-	-	-	0.161	99.8
Ti-6Al	[wt.%]	6.00	-	0.003	0.050	93.9
	[at.%]	10.16	-	0.010	0.143	89.7
Ti-6Al-0.3O	[wt.%]	6.00	-	0.002	0.307	93.7
	[at.%]	10.11	-	0.006	0.873	89.0

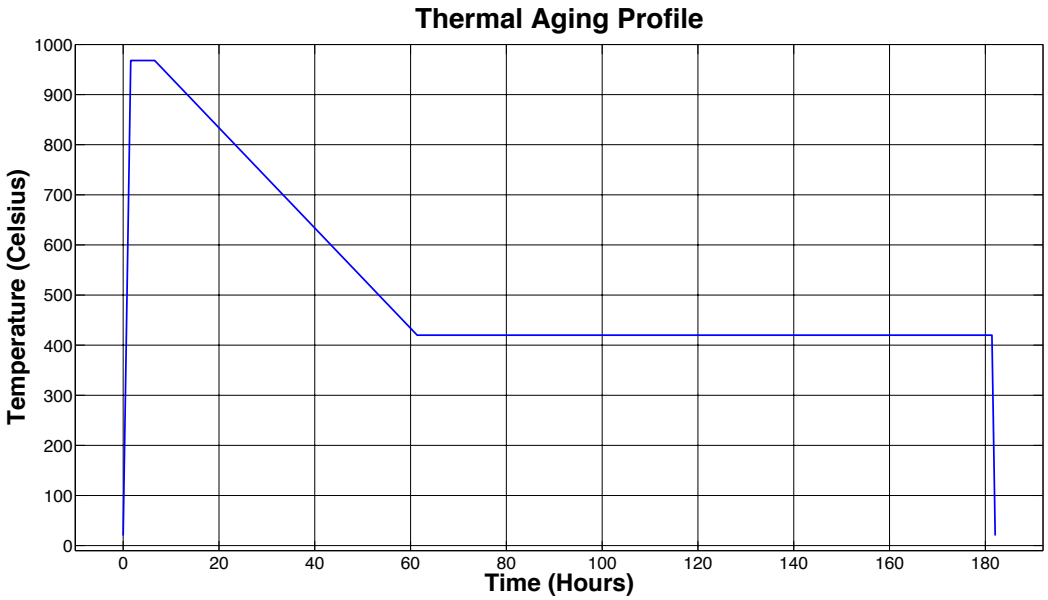

Figure 4.1: Profile for the thermal heating/aging treatment applied to the Ti-6Al and Ti-6Al-0.3O straining bar samples that promoted Ti_3Al SRO.

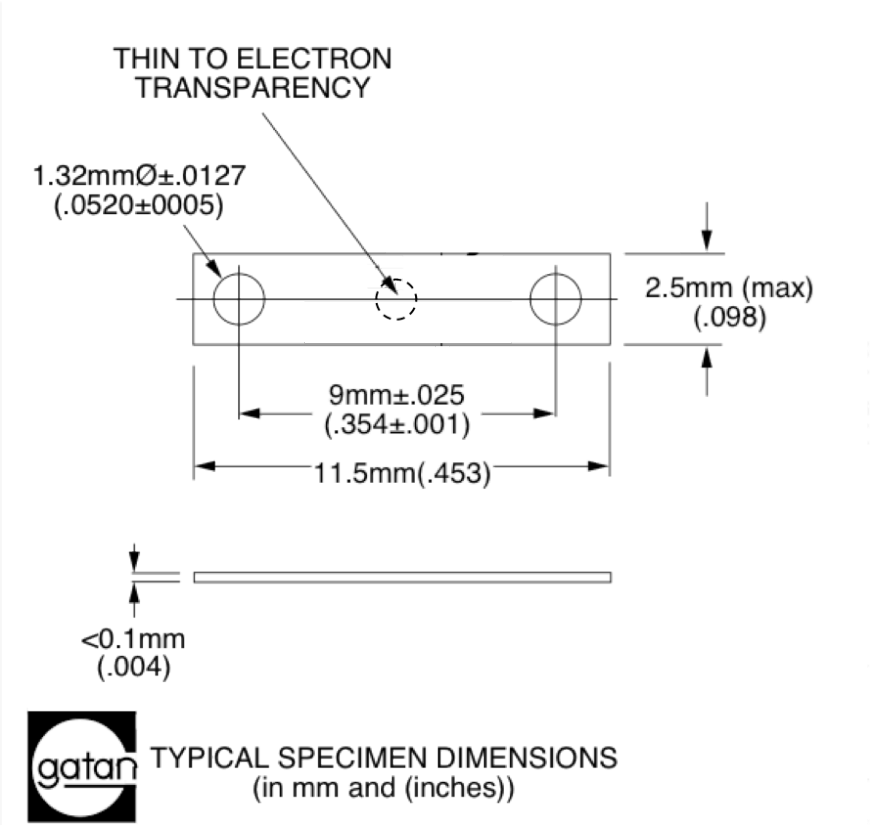

Figure 4.2: Straining bar sample dimensions as suggested by Gatan Inc. NOTE that the samples were cut (via wire EDM) to be 0.5mm thick prior to thermal aging and were polished down to <0.1mm in thickness after aging.

All aged straining bar samples were aged simultaneously, i.e. all pure Ti, Ti-6Al, and Ti-6Al-0.3O aged samples underwent the same thermal treatment, and were enclosed in quartz ampoules that were purged of air with Argon (Ar) and pumped (and sealed) under vacuum in order to minimize oxidation. The samples were then annealed and aged in a Lindberg/Blue M^{TM} Tube Furnace (Model Number: STF55433C-1) while Ar was continuously pumped through the tube. This was done to reduce the risk of oxidation in the event that the quartz ampoule fractured during the heat treatment. However, no vacuum leaks in any and all quartz ampoules were found after aging.

The samples were then manually thinned down to approximately 100-200μm in thickness (see Figure 4.2) using progressively finer grit SiC papers, ending with P-4000 as a final step. Next, the center region of the straining bar foils were electrochemically polished with a Fischione Twin Jet Electropolisher (Model 110) polishing apparatus (controlled by a Fischione Model 120 Automatic Power Control unit) until a small hole formed near the center of the straining bar. The polishing solution consisted of 94% methanol, ~423mL, and 6% perchloric acid (60% concentrated so approximately 3.6% pure perchloric acid), ~27mL. It should be noted that perchloric acid was added to methanol only when the methanol reached ≤ -30°C in an effort to slow the exothermal reaction [60]. The polishing solution was cooled within the jet polisher, via conduction, with coolant methanol and liquid nitrogen. The temperature of the polishing solution was checked frequently and liquid nitrogen was added to the coolant reservoir as needed. Electrochemical polishing was carried out at approximately -40°C in order to minimize the amount of hydrogen absorbed by the sample [60]. Voltages of around 26–30V and currents of 13–16mA, yielded a good quality polish after approximately 2.5–4.5 min. Power was cut to the jet polisher and polishing was ceased as soon as a hole was detected by the polishing apparatus, via a light sensor, and each disc was carefully rinsed in methanol followed by ethanol to remove any residual etchant.

Multiple *in situ* S/TEM straining experiments were conducted using different transmission electron microscopes located at NCEM, LBNL; the JEOL 3010 TEM, the FEI TitanX S/TEM, and the TEAM I microscope (a modified FEI Titan S/TEM). The TEAM I is a double-aberration-corrected S/TEM capable of 50pm resolution and was equipped with a high speed Gatan Inc. K2 IS direct electron detector (operated at 400 frames/second) during the *in situ* straining experiments. The K2 detector was utilized for nanobeam electron diffraction (NBED) mapping [84–85]. Dislocation analysis, i.e. **g** • **b** [86–88], and *in situ* TEM heating were also conducted on the samples using the JEOL 3010, and EDS was performed on the strain induced FCC Ti phase in the TitanX. All straining bar samples were loaded onto model 654 and model 672 Gatan Inc. single tilt straining TEM holders for the FEI and JEOL microscopes, respectively, both of which were controlled with a model 902 Gatan Inc. Accutroller.

4.2. Results and Discussion

The *in situ* S/TEM straining experiments were initially intended for NBED mapping of mobilized dislocations in various Ti-Al alloys to elucidate the connection between short-range ordering of Ti_3Al and the transition from “wavy” dislocation slip to “planar” dislocation slip. Therefore, *in situ* straining samples were made from all three alloys listed in Table 4.1 in both the aged and non-aged conditions. Half of the samples were thermally treated according to the

heating profile depicted in Figure 4.1, and a slight amount of Ti_3Al ordering was detected in TEM in the aged Ti-6Al and Ti-6Al-0.3O alloys (see Figure 4.3).

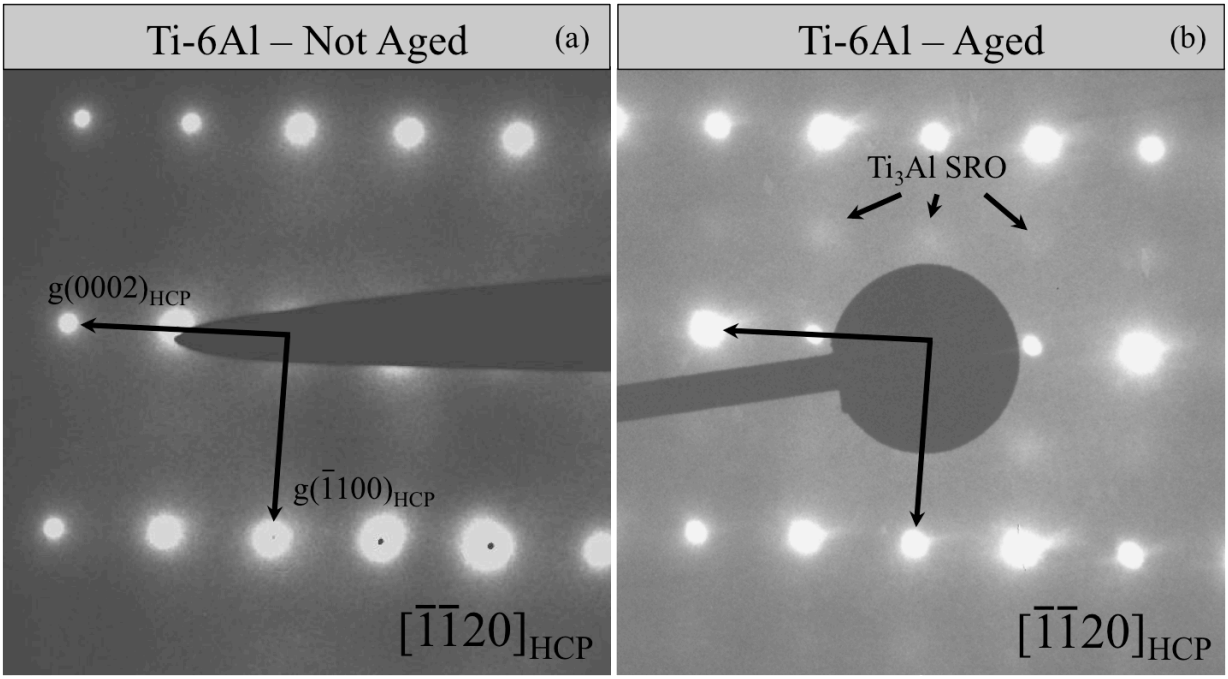

Figure 4.3: Acquired by R. Zhang. TEM SAD patterns of the Ti-6Al alloy listed in Table 4.1 in the (a) not aged and (b) aged conditions. The aged samples were heat treated according to the thermal profile depicted in Figure 4.1. (b) shows diffuse diffraction reflections indicating short range ordering (SRO) of the α_2 Ti_3Al phase.

No discernable difference in the degree of SRO was observed between Ti-6Al and Ti-6Al-0.3O alloys and, therefore, no conclusions regarding the effect of oxygen content on Ti_3Al ordering could be made. Both the aged and non-aged conditions of these alloys demonstrated planar-like dislocation slip during *in situ* straining, though it was more pronounced in the aged samples. As expected, the pure Ti samples exhibited wavy-like dislocation slip and did not show any signs of solute ordering due to thermal aging. Figure 4.4 presents a side-by-side comparison of wavy slip in pure Ti and planar slip in aged Ti-6Al-0.3O.

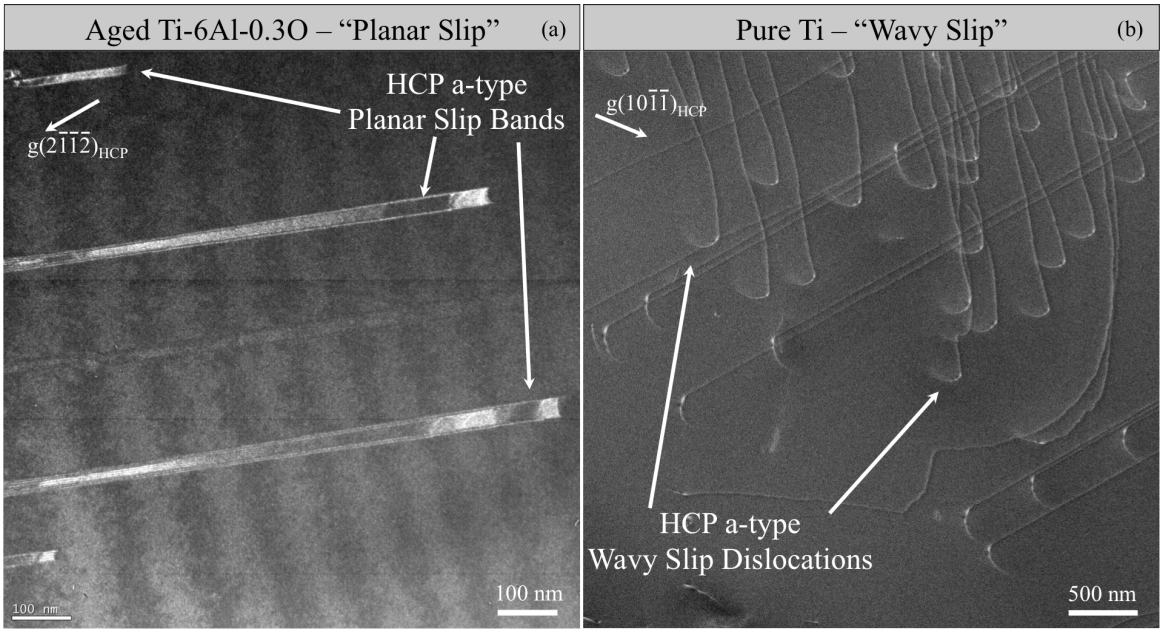

Figure 4.4: (a) and (b) are TEM darkfield images of aged Ti-6Al-0.3O and Pure Ti *in situ* TEM straining bar samples, respectively, demonstrating the difference between "planar" and "wavy" dislocation slip.

In addition to planar slip, several FCC lath-like features oriented parallel to planar slip bands were also observed in multiple Ti-6Al and Ti-6Al-0.3O straining bar samples, and dislocations were often observed emitting from the tips of these FCC precipitates as the sample was strained (see Figure 4.5).

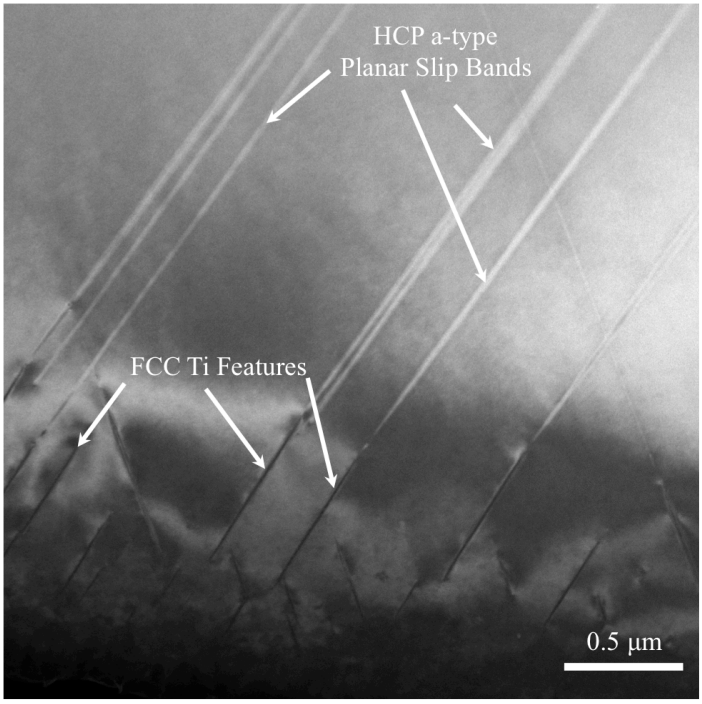

Figure 4.5: STEM micrograph of FCC precipitates emitting HCP a-type planar dislocations during *in situ* S/TEM straining.

The FCC structure was identified with NBED mapping and it was discovered that this third FCC Ti variant adopted the same HCP-FCC non-close-packed plane orientation relationship as the FIB FCC Ti hydrides (type I):

$$(001)_{FCC} \parallel (0001)_{HCP}$$
$$(1\bar{1}0)_{FCC} \parallel (1\bar{1}00)_{HCP}$$
$$[\bar{1}\bar{1}0]_{FCC} \parallel [\bar{1}\bar{1}20]_{HCP}$$

A schematic representing the alignment of the HCP and FCC Ti phases is provided in Figure 4.6.

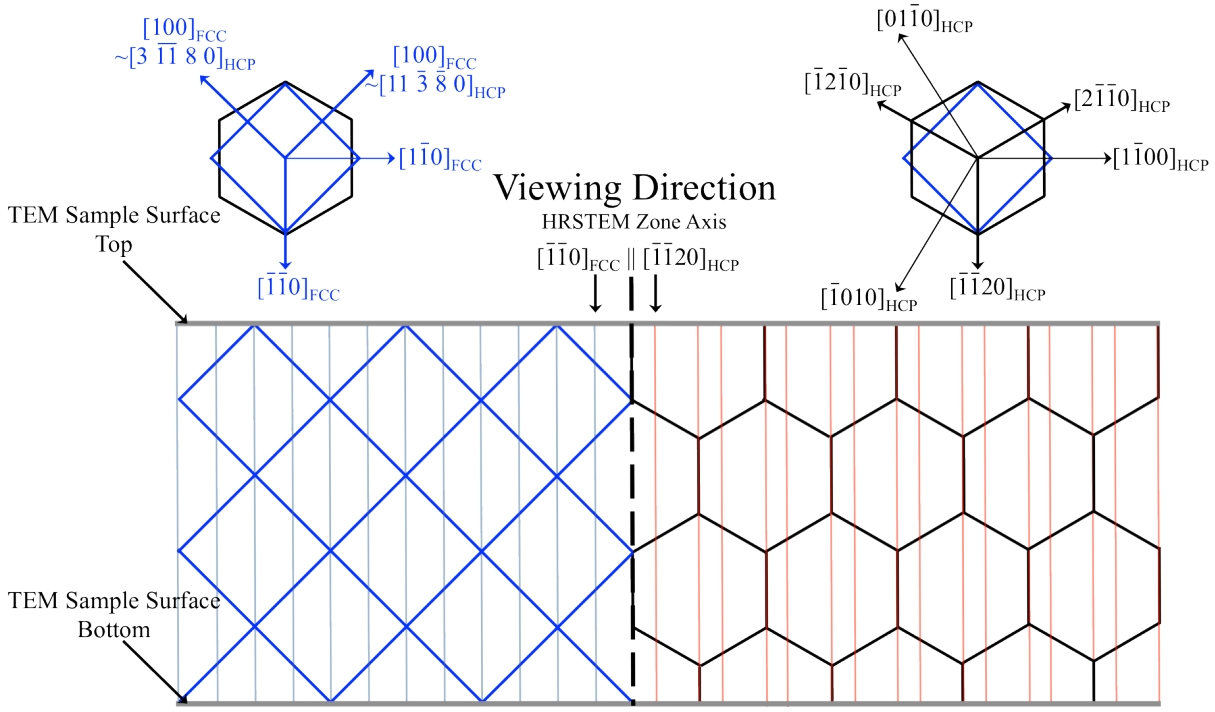

Figure 4.6: Schematic of the non-close packed relationship between the HCP and FCC Ti (Type III) phases.

Interestingly, FCC deformation twins were also found within the FCC Ti phase which changed the near perfect alignment of $(001)_{FCC} \parallel (0001)_{HCP}$ to a slightly angled alignment between $(1\bar{1}1)_{FCC\ Twin}$ // $(0001)_{HCP}$ (~13°-15°). NBED results confirming the presence of FCC twins within this FCC Ti feature are presented in Figure 4.7. Figure 4.7 also highlights the versatility of the NBED technique, showing how the manipulation of virtual (objective) apertures (small red squares in Figure 4.7-d, -f, and -h) generate the virtual darkfield reconstructions (Figure 4.7-c, -e, and -g) of the original STEM HAADF image (Figure 4.7-b). In other words, this technique helped isolate and identify which diffraction reflections corresponded to the HCP, FCC primary, and FCC twinned regions.

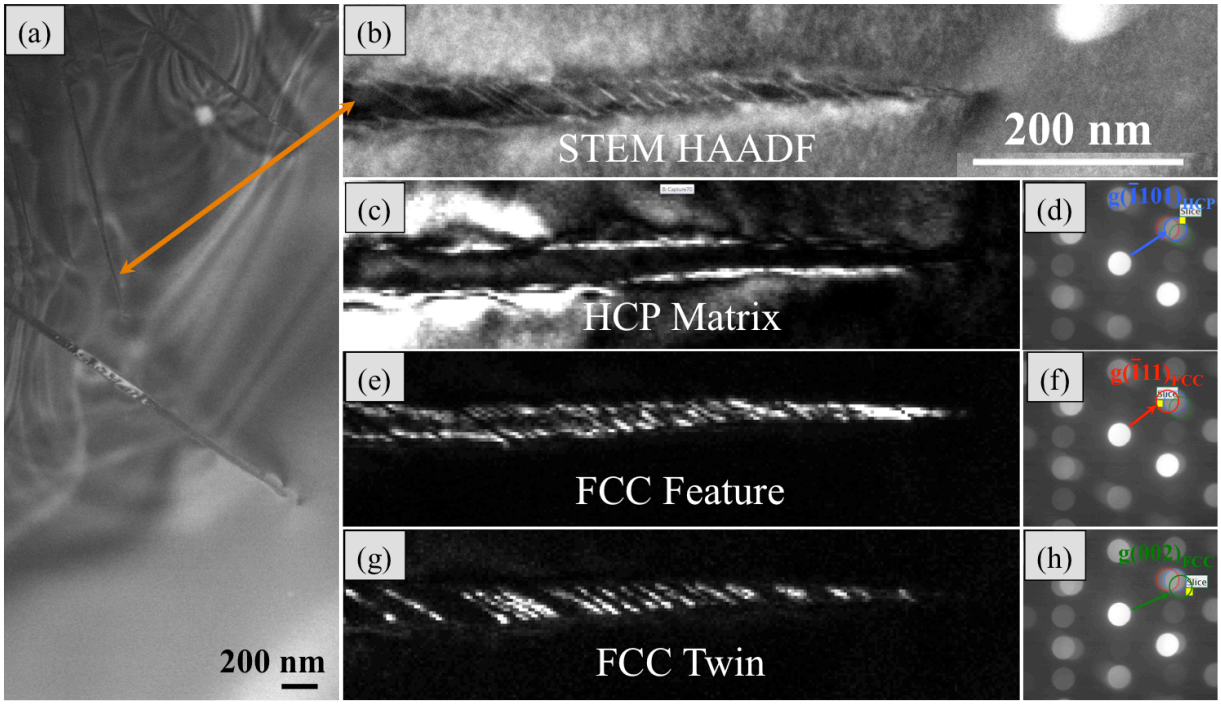

Figure 4.7: (a) is a low magnification STEM HAADF image of FCC features within a Ti-6Al (wt.%) *in situ* S/TEM straining bar sample which was aged to promote SRO of the α_2 (Ti_3Al) phase. The FCC features formed during sample preparation and grew during *in situ* TEM straining. The orange arrow indicates the FCC feature that was observed using nanobeam diffraction and corresponds to images (b) through (h). (b) is a high magnification STEM HAADF of the FCC feature indicated in (a). (c) through (h) are a collection of virtual darkfield reconstructions (VDRs) and diffraction patterns (DPs) all of which were contained within the same NBED dataset. VDRs (c), (e), and (g) were generated using information contained only within the small yellow square indicated in DPs (d), (f), and (h), respectively. The overlapping diffraction reflections chosen for VDR are indexed by the blue, red, and green arrows in (d), (f), and (h) correspond to the $\vec{\mathbf{g}}(\bar{1}101)_{HCP}$ HCP matrix, $\vec{\mathbf{g}}(\bar{1}11)_{FCC}$ FCC feature, and $\vec{\mathbf{g}}(002)_{FCC}$ FCC twin reflections, respectively.

The lattice parameter of this new FCC Ti structure ($a_{FCC\text{-}3}$) was determined from SAD TEM micrographs, as shown in Figure 4.8, by measuring the distances of FCC SAD reflections relative to the known HCP SAD reflections of assumed HCP α-Ti lattice parameters a_{HCP} = 2.95Å and c_{HCP} = 4.68Å [1]. By this method, $a_{FCC\text{-}3}$ was found to be 4.17 ± 0.02Å.

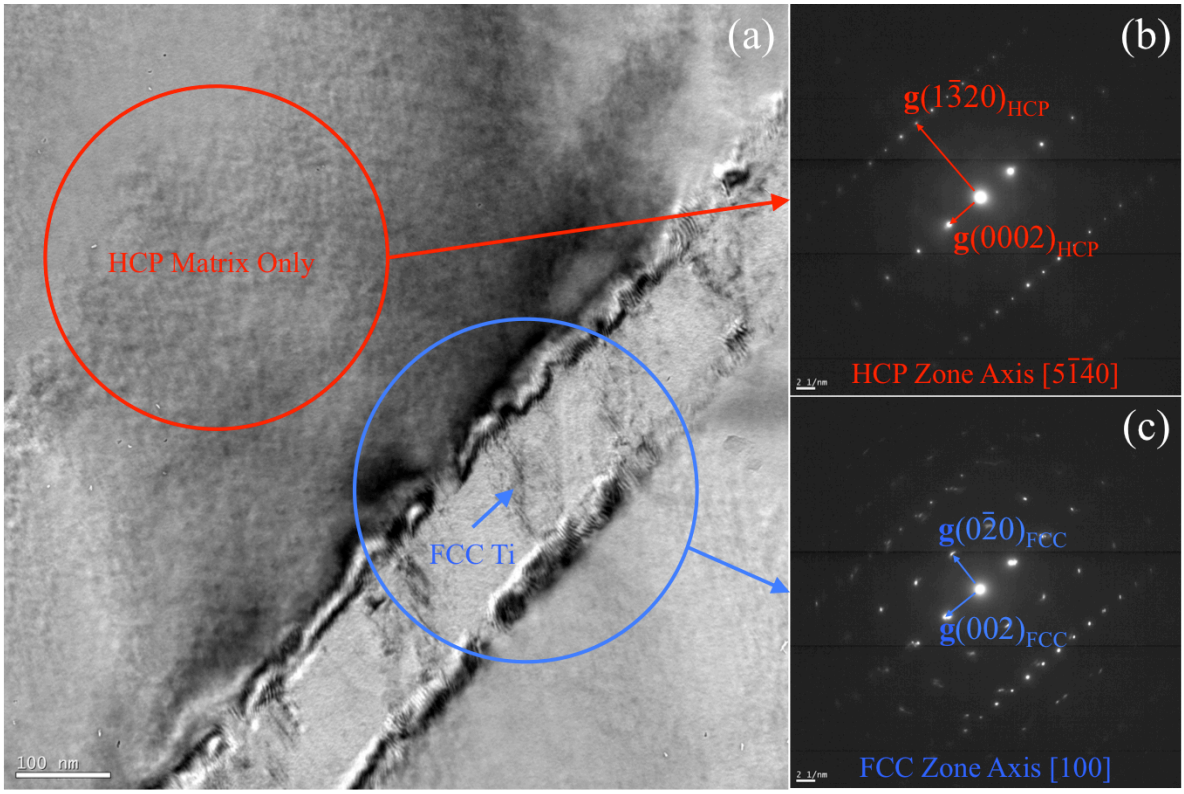

Figure 4.8: (a) TEM brightfield micrograph of the same FCC feature presented in Figure 4.7(a). The red and blue circles indicate the locations of the SAD aperture that generated DPs (b) and (c), respectively. (b) and (c) are SAD DPs of the HCP only and HCP+FCC Ti phases, respectively.

Since these FCC Ti features were present prior to *in situ* TEM straining, they were assumed to have formed during TEM sample preparation, specifically during twin-jet electropolishing. Most FCC features were found primarily around the thinnest and most damaged regions of the sample, i.e. nearest the hole and around bends and cracks, and appeared to be thinner than the surrounding HCP matrix, or nearly cracks themselves, as the transmitted diffraction disc would become much brighter whenever the electron beam encountered an FCC feature. These collective observations suggest that either contamination from the jet polishing solution, namely hydrogen and/or oxygen, or the mechanical forces applied by the twin-jets on an actively thinning film, or a combination of the two, lead to the formation of this third FCC Ti phase. As was done for the FIB induced FCC Ti case, these straining bar samples were *in situ* TEM heated above 300°C to check for hydride contamination. Some dislocation-related "activity" was observed, however, these FCC features did not disappear or revert back into the HCP structure unlike the FIB induced case. Therefore, it was concluded that this third FCC Ti variant was unlikely to be a type of Ti hydride though there may have been some Ti-hydrides adhered to them that dissociated upon heating. The decomposition of Ti-hydrides into "pure" FCC Ti was reported by Vullum *et al*. (2008) [53] in ball milled Ti microparticles who claimed that ball milling led to the formation of TiH_x ($x<0.67$) crystallites that were unstable under a TEM electron beam and decreased in lattice parameter (4.22Å to 4.10Å) with continued exposure. This resulting "pure" FCC Ti phase was found to be stable under ambient conditions and it was suspected that both hydrogen and the small crystallite size (10-20nm sized grains within a 50μm

diameter particle) contributed to FCC Ti stabilization [53]. The strain induced FCC feature in the present investigation did not appear to be unstable or change shape in anyway during 300kV TEM and STEM imaging and the "activity" mentioned previously was the only indication of possible hydride contamination. However, this "activity," or changes in local contrast, could have easily been due to the mobilization of dislocations during heating and unrelated to hydride decomposition. Since oxygen is suspected to stabilize the thermally induced FCC phase (FCC Ti type II, discussed in chapter 3), EDS was conducted on the largest FCC Ti feature found in Figure 4.7.

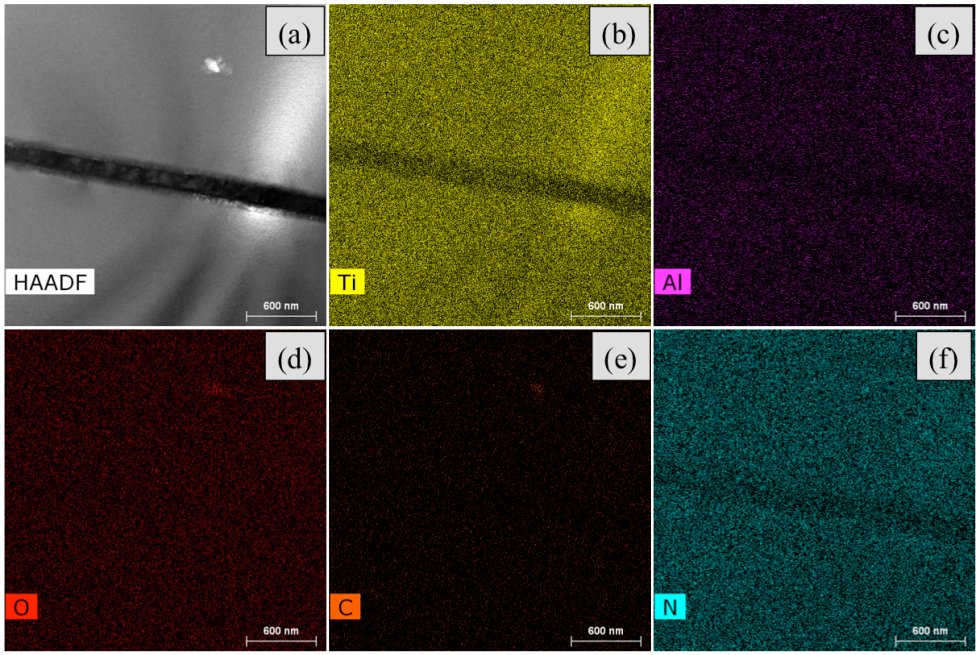

Figure 4.9: (a) STEM HAADF image of an FCC feature after *in situ* TEM heating to check for hydride contamination. (b) through (f) are the Ti, Al, O, C, and N EDS elemental maps of (a), respectively. Chemical content estimations of the FCC feature and the surrounding HCP region are presented next in Table 4.2.

Table 4.2: Estimated chemical composition of the FCC and HCP phases in Figure 4.9. The Cu signal was assumed to generate from the Cu washers and hex ring holding the sample in place within the *in situ* TEM straining holder.

Phase	**Estimated Chemical Content [Atomic %]**						
	Ti	**Al**	**O**	**C**	**N**	**Cl**	**Cu**
FCC	58.4	6.73	15.5	13.0	5.23	0.490	0.591
HCP	62.7	6.70	12.3	14.3	3.10	0.419	0.472

Due to the difficulties in measuring x-rays generated by light elements (i.e. atomic number below 11) [78–79], the chemical compositions of the HCP and FCC phases listed in Table 4.2 were not trusted to be accurate. However, these results did not qualitatively indicate any significant increase in O, C, and N contents within the FCC phase relative to the HCP phase. The EDS results combined with the evidential lack of hydride dissolution during *in situ* TEM heating led

to the conclusion that this third FCC Ti variant was not any of the suspected impurity driven Ti compounds listed in Table 1.2.

Instead, it is proposed that these FCC features are a stress-relaxation response to mechanical straining since they appeared to grow during *in situ* TEM straining in quick bursts and were frequently observed emitting HCP dislocations into the thicker region of the TEM foil. These dislocations were determined to be a-type ($\vec{\mathbf{b}}=1/3[11\bar{2}0]_{HCP}$) through $\vec{\mathbf{g}}\cdot\vec{\mathbf{b}}$ analysis, summarized in Figure 4.10.

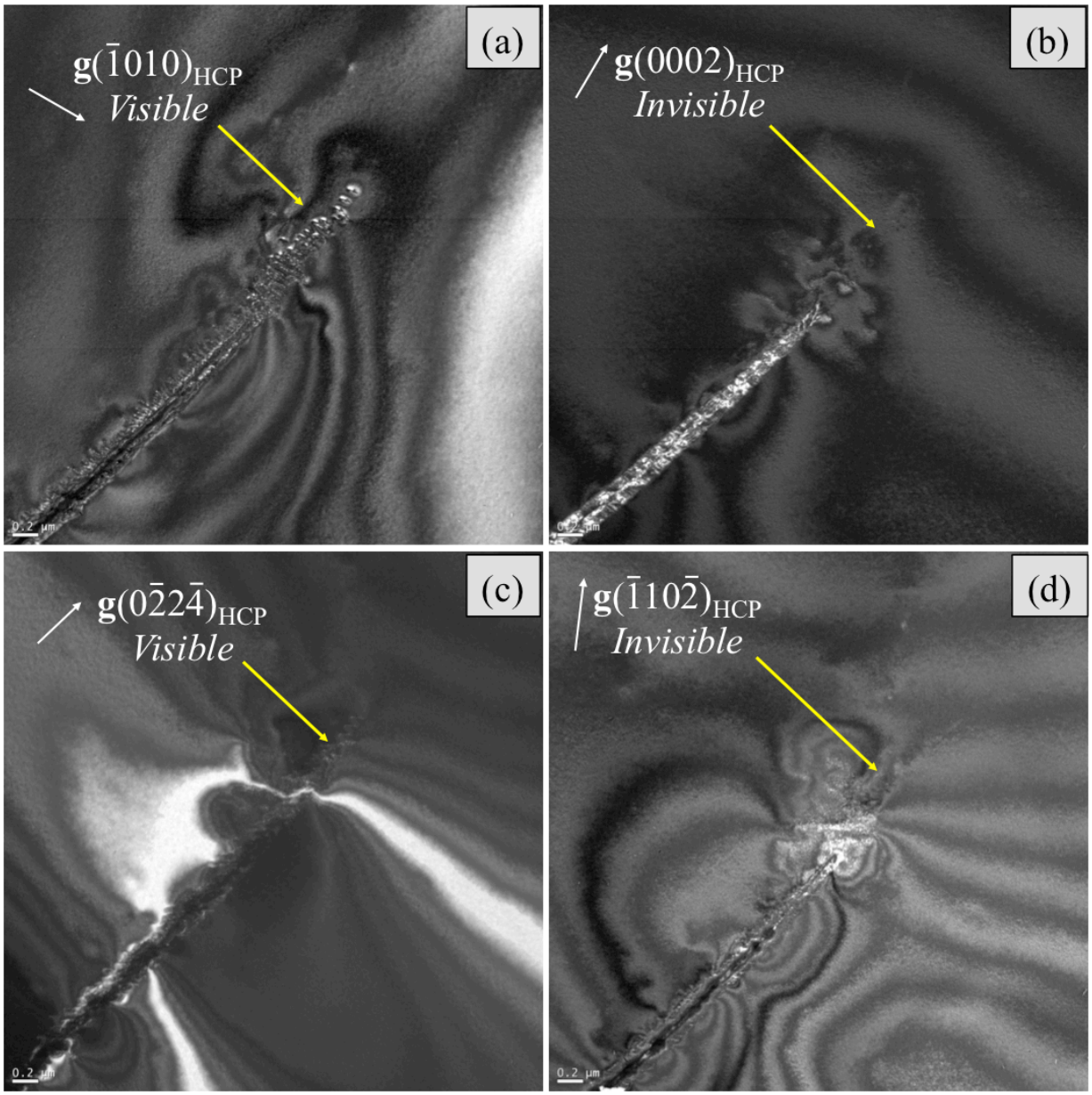

Figure 4.10: (a) through (d) are a collection of weak beam darkfield (WBDF) micrographs of that HCP dislocations that were emitted from the FCC phase during *in situ* TEM straining. The visibility of the dislocations under different imaging conditions was utilized to determine the type and Burgers vector of these HCP dislocations, i.e. a $\vec{\mathbf{g}}\cdot\vec{\mathbf{b}}$ analysis [86–88].

The relationship between **a**-type HCP dislocations and the nucleation of the FCC structure within α-Ti TEM samples is not well understood. NBED was conducted on overlapping HCP **a**-type dislocations and the FCC $\vec{\mathbf{g}}(1\bar{1}\bar{1})_{FCC}$ and $\vec{\mathbf{g}}(\bar{2}20)_{FCC}$ virtual darkfield reconstructions hint at the presence of an FCC nuclei within the HCP matrix (see Figure 4.11). This is suggestive that the HCP-to-FCC transformation in α-Ti is mediated through the glide and dissociation of multiple perfect **a**-type dislocations into partial dislocations.

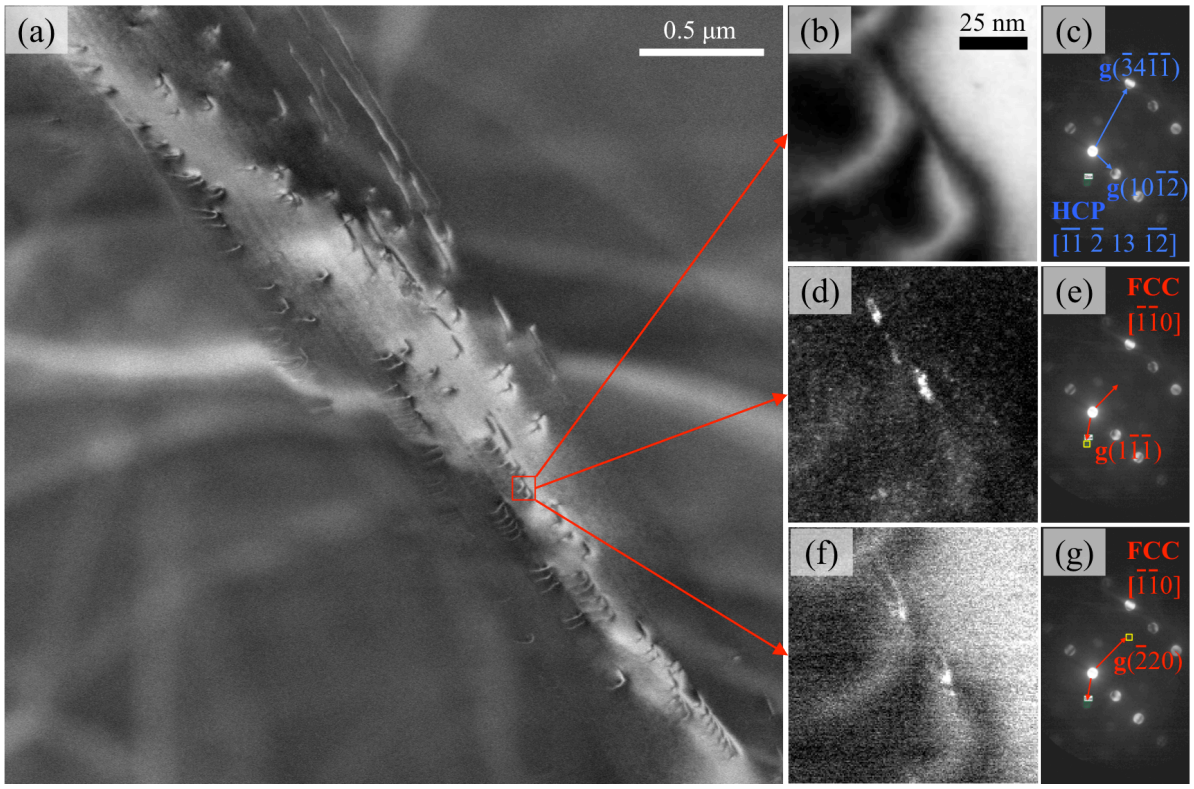

Figure 4.11: NBED of FCC nuclei. (a) HAADF STEM micrograph of HCP **a**-type dislocations emitted from an FCC Ti feature (out of view) due to *in situ* STEM straining. (b) is the NBED HAADF STEM image (virtual BF reconstruction). (d) and (f) are virtual DF reconstructions selecting the $\vec{\mathbf{g}}(1\bar{1}\bar{1})_{FCC}$ and $\vec{\mathbf{g}}(\bar{2}20)_{FCC}$ reflections (selected region indicated by the yellow square in (e) and (g)), respectively. (c), (e), and (g) are indexed DPs showing the rough zone axes alignment. Note that the HCP phase is tilted slightly off the high order zone $[\bar{1}\bar{1}\ \bar{2}\ 13\ \bar{1}\bar{2}]_{HCP}$, which is fairly close to the $[\bar{1}\bar{1}20]_{HCP} \parallel [\bar{1}\bar{1}0]_{FCC}$.

HRSTEM imaging and Burgers circuit analysis of the HCP-FCC interface (see Figure 4.12) and of the **a**-type HCP dislocations emitted from the FCC feature during *in situ* straining (see Figure 4.13) show possible evidence of both HCP and FCC Shockley partial (SP) dislocations. The same HRSTEM images in 4.12(b) and (e), but with no overlaid markings, along with two additional HRSTEM images are also provided in Figures 4.14 – 4.17 for reference. It is uncertain if the observed HCP SPs are actually SPs with $\vec{\mathbf{b}}=1/3[1\bar{1}00]_{HCP}$ or perfect **a**-type dislocations with $\vec{\mathbf{b}}=1/3[2\bar{1}\bar{1}0]_{HCP}$ where only the $[1\bar{1}00]_{HCP}$ portion of the perfect dislocation can be resolved when viewing along the $[\bar{1}\bar{1}20]_{HCP}$ zone axis. Theoretically, a perfect **a**-type dislocation viewed under this orientation should distort the atomic HRSTEM image significantly. Therefore, it is

probable that the HCP SP observed in Figure 4.12(c) is indeed a SP since a high quality HRSTEM image was acquired. Though it is less justifiable in Figure 4.13(b) due to the large out-of-focus region (hence why the Burgers circuit was drawn so large).

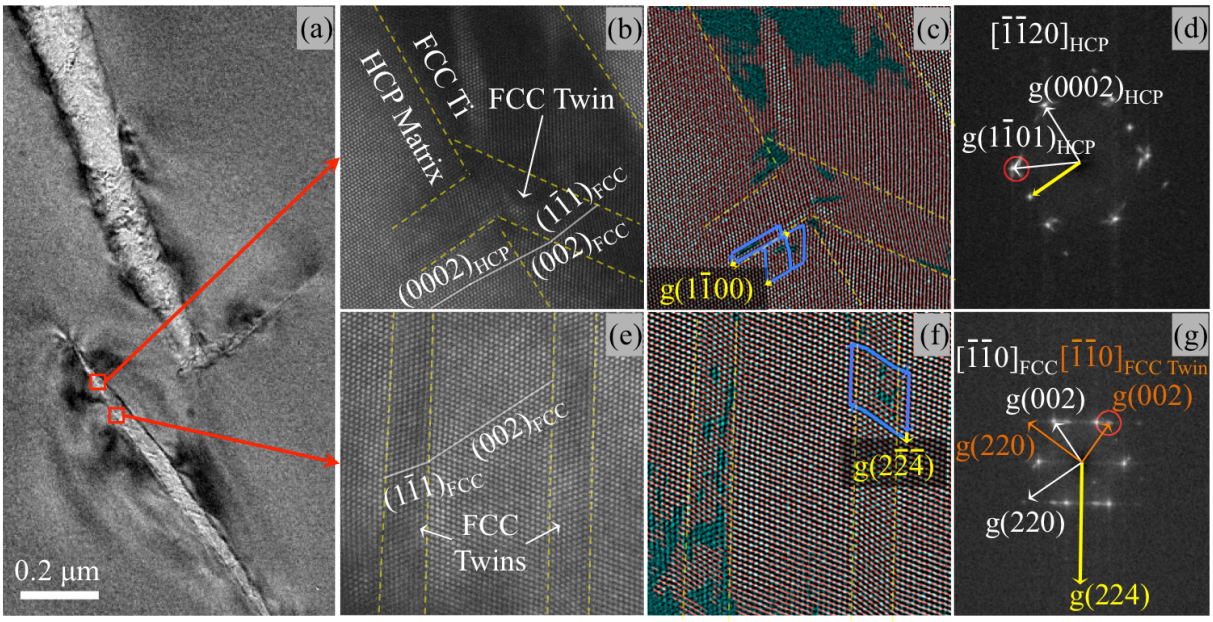

Figure 4.12: (a) STEM image of FCC Ti features induced in an aged Ti-6Al-0.3O *in situ* S/TEM straining bar sample. (b) and (c) are the same HRSTEM micrograph of the HCP-FCC region outlined by the upper red square in (a), where (c) has the $(1\bar{1}01)_{HCP}$ plane lines overlaid in red. Disruptions in the plane lines appear green, which help locate dislocations for Burgers circuit analysis. (d) is the FFT of (b) and is equivalent with the $[\bar{1}\bar{1}20]_{HCP}$ DP. The red circle in (d) indicates the chosen diffraction reflection for the overlaid plane lines in (c). (e), (f), and (g) follow the same descriptions as (b), (c), and (d) but for the FCC-FCC_{Twin} region outlined by the lower red square in (a). The same HRSTEM images in (b) and (e), but with no overlaid markings, along with two additional HRSTEM images is also provided in Figures 4.14 – 4.

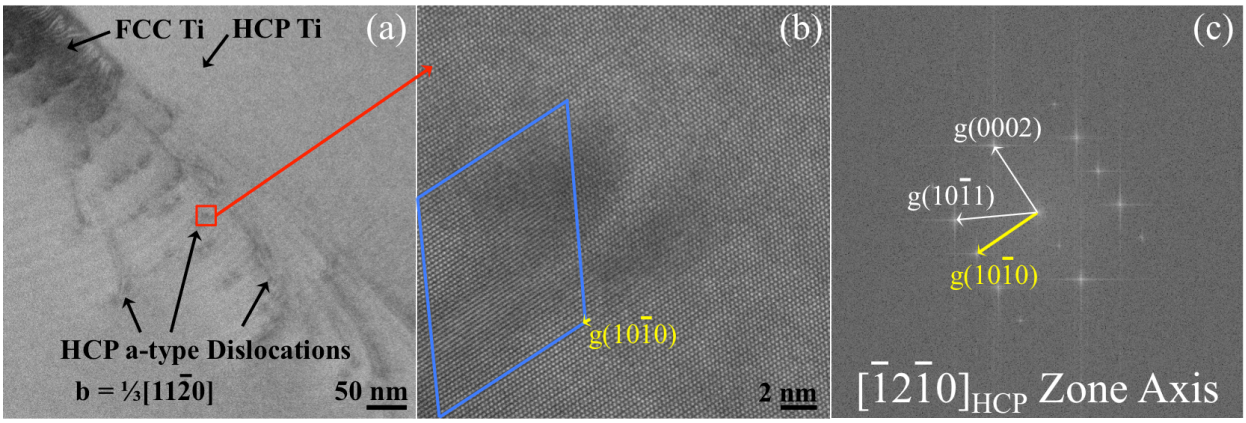

Figure 4.13: (a) STEM image of the a-type HCP dislocations emitted from the FCC feature during *in situ* straining. (b) is an HRSTEM micrograph of the region outlined by the red square in (a) and Burgers circuit analysis indicate the presence of HCP Shockley partial dislocations. (c) is the FFT of (b) and is equivalent with the $[\bar{1}2\bar{1}0]_{HCP}$ DP.

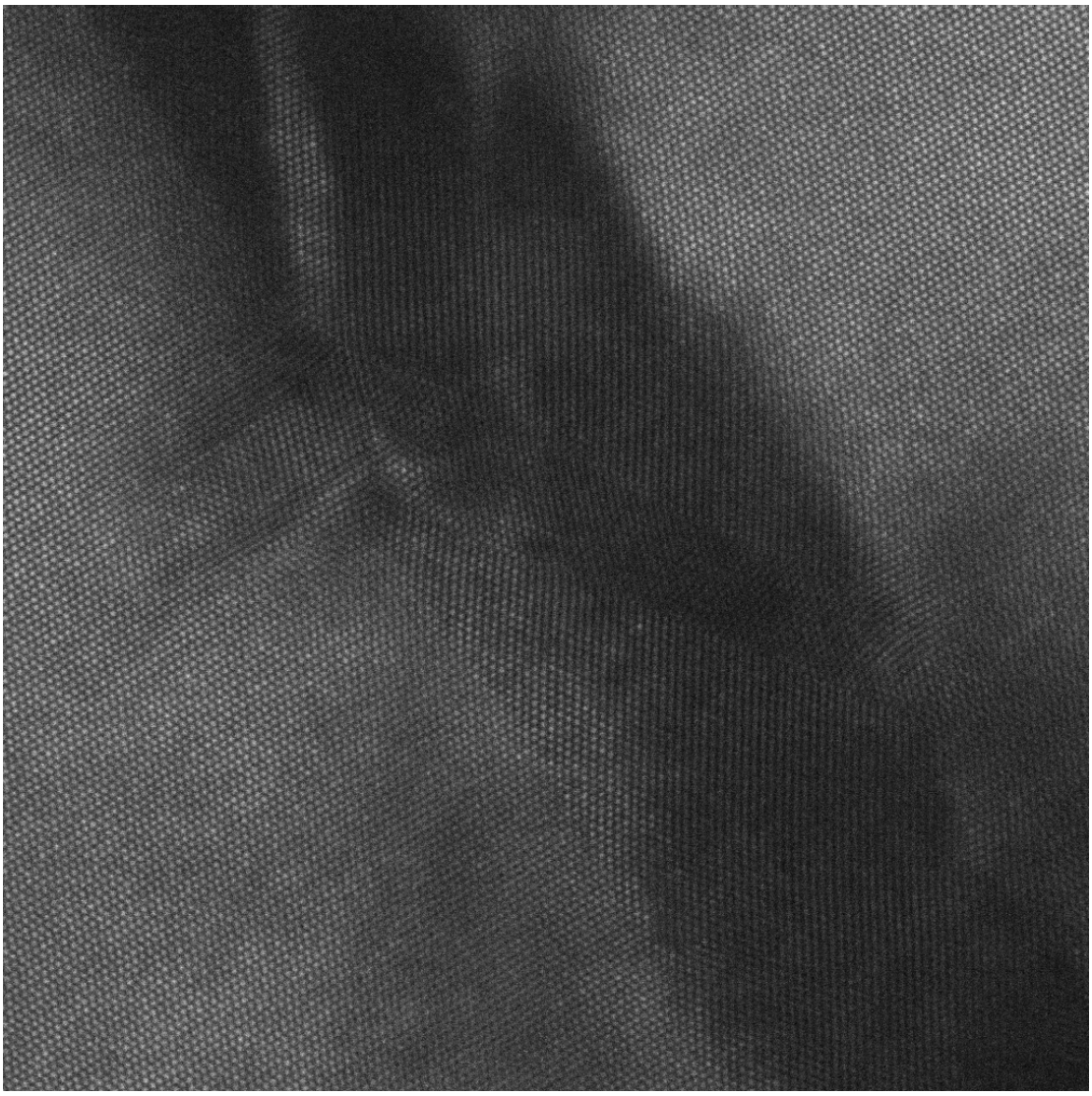

Figure 4.14: The same HRSTEM micrograph as 4.12(b) but without overlaid boundary lines for better viewing.

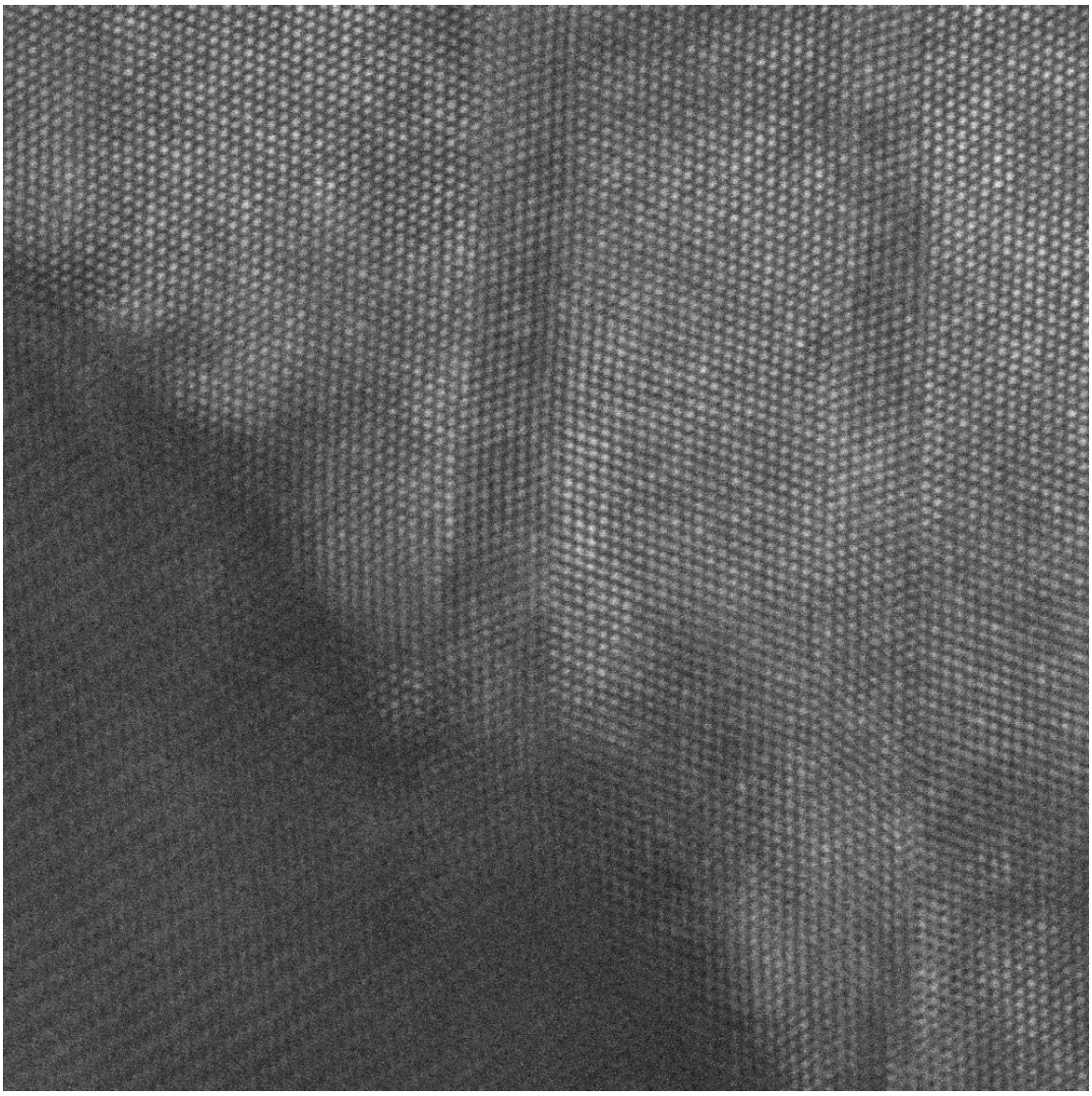

Figure 4.15: The same HRSTEM micrograph as 4.12(e) but without overlaid boundary lines for better viewing.

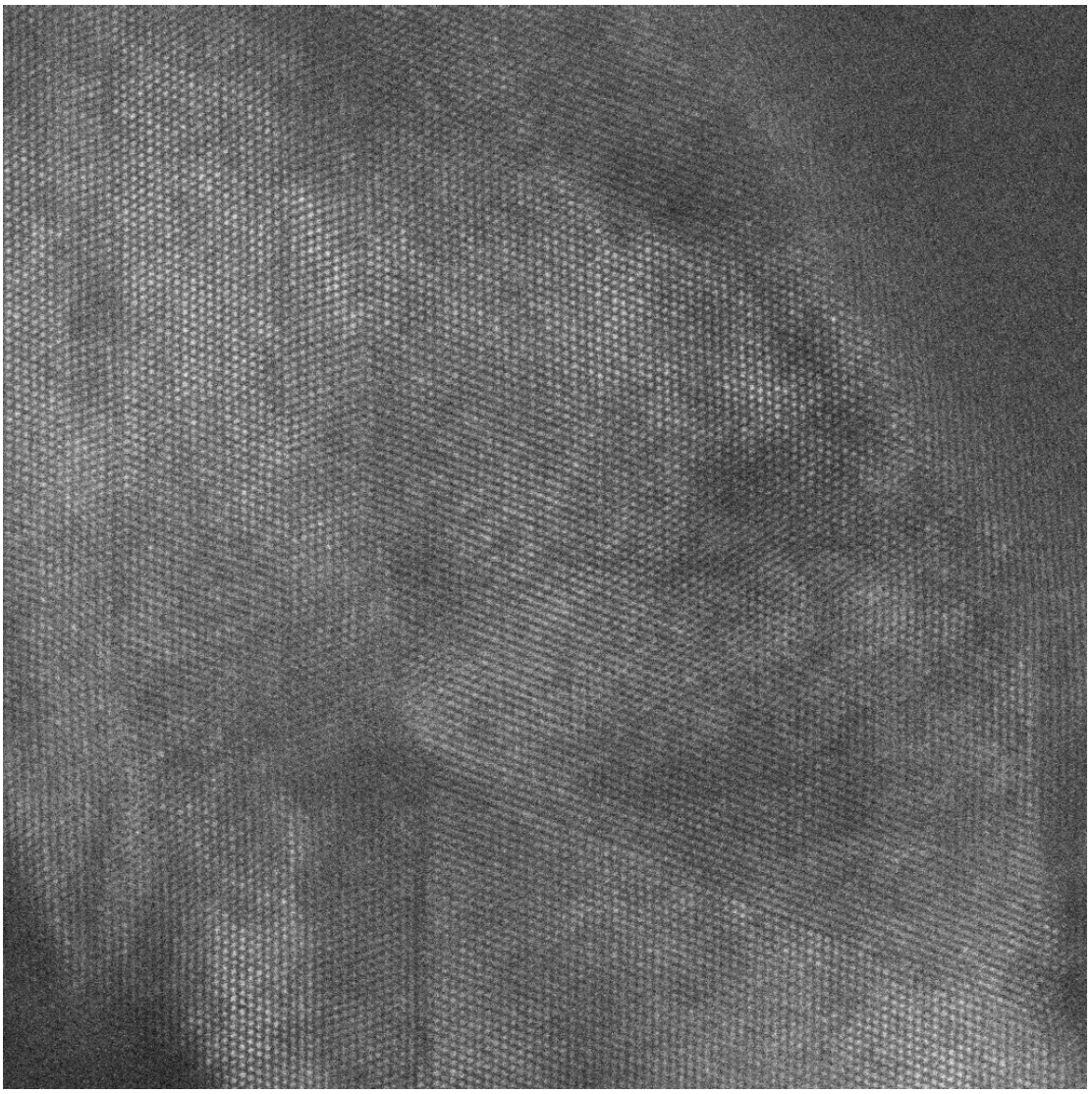

Figure 4.16: HRSTEM micrograph very near the same region as 4.12(e). Note the junction vertices where suspected FCC SPs have interacted.

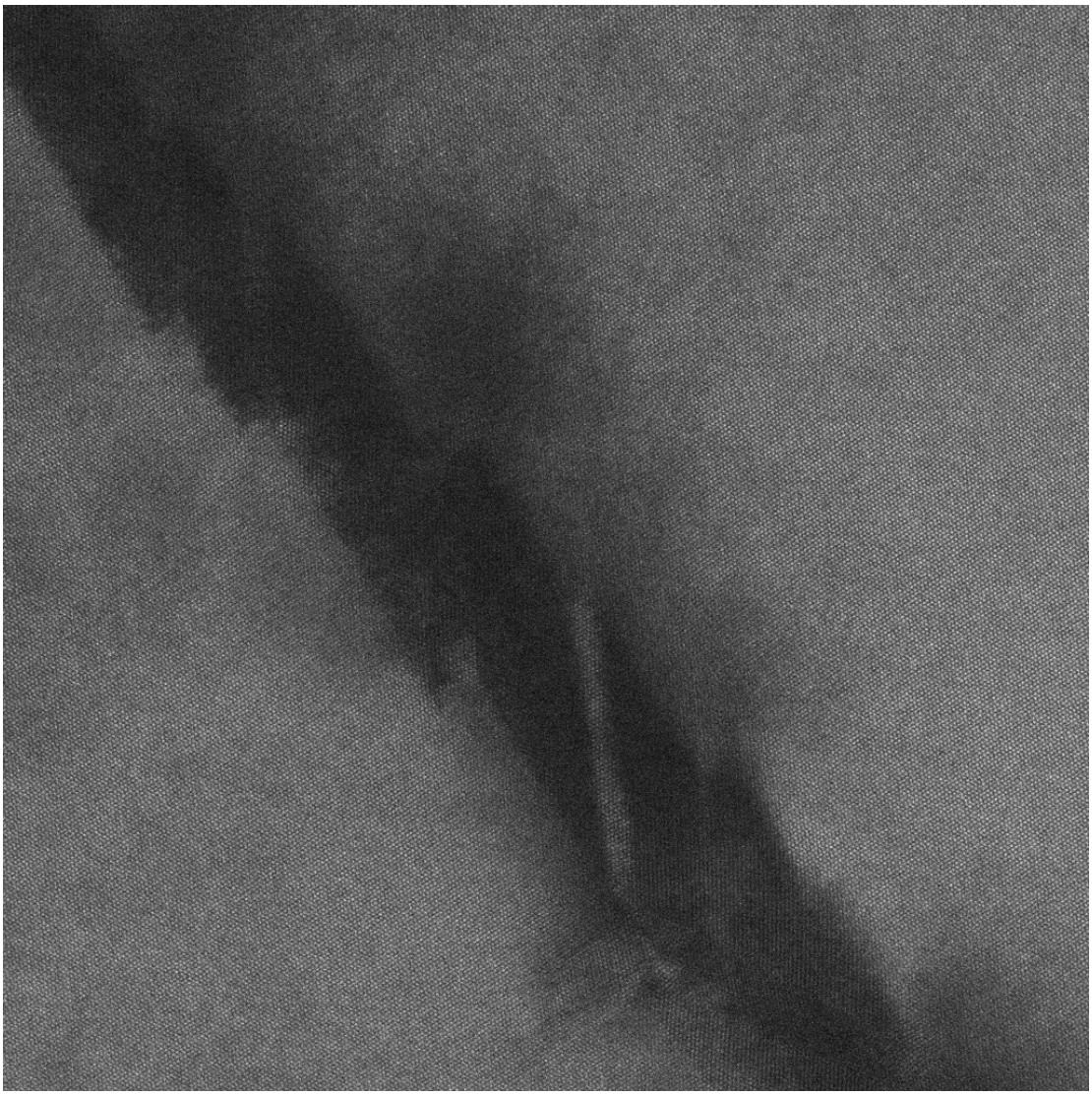

Figure 4.17: HRSTEM micrograph of the same region as 4.12(b) but at lower magnification. Note the helical nature of the FCC band and the distorted region protruding from the lower left side. It is suspected that this distortion is actually cause by a dissociated **a**-type HCP dislocation.

Connections between deformation twinning and partial dislocation glide have been extensively reported for FCC metals [89], and it is therefore no surprise that both FCC perfect dislocations ($\vec{\mathbf{b}}=1/2\langle 110\rangle_{FCC}$) and FCC Shockley partials ($\vec{\mathbf{b}}=1/6\langle 112\rangle_{FCC}$) were found near the FCC-FCC$_{Twin}$ boundary (see Figure 4.12(f)). The dissociation of multiple **a**-type ($\vec{\mathbf{b}}=1/3[11\bar{2}0]_{HCP}$) dislocations into SPs ($\vec{\mathbf{b}}=1/3[1\bar{1}00]_{HCP}$) and the subsequent glide of SPs on every other close-packed plane is the proposed mechanism for the HCP-FCC transformation in cobalt (Co) [90]. However, this mechanism results in the alignment of the close-packed planes, i.e. $(0002)_{HCP} \parallel \{111\}_{FCC}$, but does not explain the $(0002)_{HCP} \parallel \{002\}_{FCC}$ orientation relationship observed in the Type I (FIB induced) and Type III (strain induced) FCC Ti studies. Theories for the HCP-to-FCC transformation involving the dissociation and ordered glide of HCP **a**-type dislocations on prism and/or pyramidal planes that could generate the observed $(0002)_{HCP} \parallel \{002\}_{FCC}$ orientation relationship are discussed in detail next in chapter 5.

4.3. Conclusion

A face-centered cubic structure of titanium has been widely reported since its discovery in 1969 [13]. The FCC Ti phase does not appear on any equilibrium phase diagram, however, the strain induced FCC Ti variant discussed in the current chapter was found to be stable after formation. Analytical S/TEM combined with NBED and *in situ* straining and heating experimentation were implemented to deduce the structural and chemical nature of this third FCC Ti phase. The results presented in this chapter suggest that strain-induced FCC Ti cannot be a Ti hydride nor oxide and forms an unusual non-close packed plane orientation relationship with the parent HCP phase:

- A HCP to FCC transformation was induced in Ti-6Al (wt.%) TEM foils during sample preparation and growth were observed during *in situ* TEM straining.
    - TEM SAD, HRSTEM, and NBED mapping were implemented to evaluate the FIB FCC lattice parameter (4.17 ± 0.02Å).
    - S/TEM and NBED mapping also show that FIB FCC Ti adopts the following HCP-FCC orientation relationships:

$$(001)_{FCC} \parallel (0001)_{HCP}$$
$$(1\bar{1}0)_{FCC} \parallel (1\bar{1}00)_{HCP}$$
$$[\bar{1}\bar{1}0]_{FCC} \parallel [\bar{1}\bar{1}20]_{HCP}$$

    - Deformation twins were also observed and appeared within the initial FCC phase. It is thought that the periodic nature of FCC twinning may be indicative of a transformation mechanism involving $[0001]_{HCP}$ axial rotations.
    - $\vec{\mathbf{g}}\cdot\vec{\mathbf{b}}$ analysis was conducted on the dislocations that were emitted from the FCC features during *in situ* straining and were concluded to be **a**-type $\vec{\mathbf{b}}=1/3[11\bar{2}0]_{HCP}$ dislocations. Burgers circuit trace analysis around the HCP-FCC and FCC-FCC_{Twin} interfaces show possible evidence of both HCP and FCC Shockley partial dislocations (SPs), though, additional work is needed to confirm HCP SPs.
    - EDS did not qualitatively indicate any significant increase in O, C, N, and Ga contents within the type III FCC phase relative to the HCP phase and TiGa, TiC, TiN, and TiO were disregarded as possible candidates for the strain induced case.
    - The strain induced FCC Ti phase did *not* disappear when *in situ* TEM heated above 300°C (unlike type I FCC Ti) indicating that this strain induced FCC Ti phase was also not a form of Ti hydride [60].

Chapter 5. The HCP - FCC Transformation
Background & Transformation Mechanisms

Due to the inherent limitations in analytical electron microscopy, primarily with quantifying chemical contents and stage tilting capabilities during *in situ* S/TEM straining (i.e. single tilting axis severely reduced the chances of observing these features on zone axis), the HCP to FCC transformation mechanism in Ti could not be positively identified. However, a transformation mechanism based on the literature and the collective experimental observations discussed in chapters 2 through 4 is proposed here.

5.1. Related Transformations in the Literature

The next sections present additional literature background pertaining to the HCP-FCC transformation for cobalt (Co) and more recent FCC Ti investigations [55–58].

5.1.1. HCP – FCC Transformations in Cobalt

Pure Co exhibits the HCP and FCC crystal structures at low and high temperatures, respectively [90]. The FCC to HCP transformation occurs during cooling from the FCC phase field and is martensitic in nature [91]. Transitioning from an FCC (ABCABC…stacking sequence) into an HCP (ABABAB…stacking sequence) crystal structure can be achieved through the motion of FCC Shockley partial (SP) dislocations ($\vec{\mathbf{b}}=1/6\langle 11\bar{2}\rangle_{FCC}$) on every second closed-packed $(111)_{FCC}$ plane. A schematic depicting this dislocation mediated transformation was taken from Bauer *et al*. (2011) [90] and is presented in Figure 5.1.

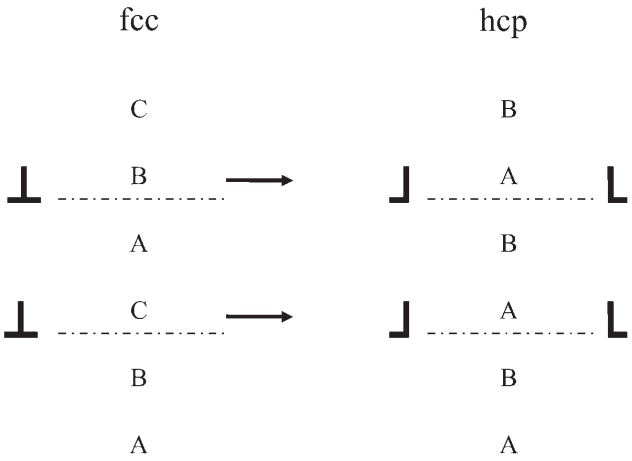

Figure 5.1: Taken from Bauer *et al*. (2011). *Phil Mag.,* **91**(3), p. 441 [90]. Ordered arrays of SPs gliding through an FCC Co crystal resulting in the HCP Co structure.

Bauer *et al*. [90] investigated the reversibility of this transformation using thermal cycling through the transition temperature regime. Interestingly, a temperature hysteresis was observed, i.e. the martensite start temperature (M_S) for the FCC-to-HCP transformation ranged from 419°C

to 388°C whereas the austenite start temperature (A_S) for the reverse HCP-to-FCC transformation ranged from 421°C to 447°C. After extensive cycling (~60), a fixed transformation temperature range was achieved, i.e. constant values for M_S and A_S. These observations were supported with light microscopy to assess the evolving microstructure as a function of the number of thermal cycles. It was proposed that the stabilization of the transition temperature regime and gradual elimination of HCP martensite plate variants (with increasing number of thermal cycles) was related to the stabilization of an ordered dislocation network that carried the forward (HCP to FCC) and backward (FCC to HCP) phase transformations. A schematic of the developing dislocation network upon increasing number of thermal cycles was taken from Bauer *et al*. [90] and is presented in Figure 5.2 for clarity.

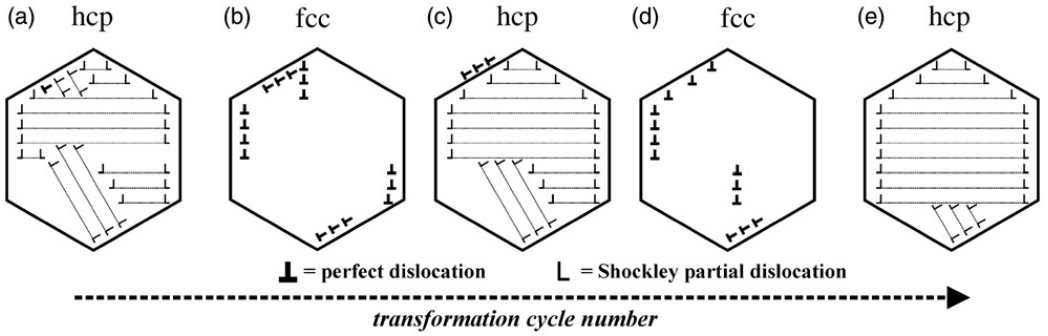

Figure 5.2: Taken from Bauer *et al*. (2011). *Phil Mag.,* **91**(3), p. 454 [90]. Schematic presentation of the evolving dislocation structure within a single Co grain during thermal cycling through the HCP←→FCC temperature regime. (a) The initial state represents the severely deformed HCP Co phase as formed by perfect FCC dislocations dissociating into an ordered array of FCC SPs that slip on alternating parallel $(111)_{FCC}$ planes; a single packet of parallel SPs glides along one of the four available $\{111\}_{FCC}$ planes (two variants are depicted in (a)). (b) through (e) Continued thermal cycling promoted a preferred set of SPs (perpendicular to $(0001)_{HCP} \parallel (111)_{FCC}$ planes) operating within a single grain.

The initial sample (a 5mm diameter high purity Co rod) was severely deformed prior to the first thermal cycle, i.e. the sample was not annealed after manufacturing and was referred to as the "hammered state". Despite the instability of FCC Co at room temperature, regions of retained FCC structure were observed between HCP martensitic plate-like features in the as-received sample. The HCP plates were assumed to have formed during alloy production (cooling from high temperatures) through the dissociation of perfect FCC dislocations ($\vec{\mathbf{b}}=1/2\langle\bar{1}10\rangle_{FCC}$) into FCC SPs ($\vec{\mathbf{b}}=1/6\langle11\bar{2}\rangle_{FCC}$) and their subsequent glide on alternating closed packed parallel $(111)_{FCC}$ planes within the parent FCC lattice. Due to the higher number of available close-packed slip planes in the FCC lattice, i.e. four distinct sets of $\{111\}_{FCC}$ planes vs. one $(0001)_{HCP}$, multiple HCP plate orientations were often found within a single grain in the initial state. It was assumed that these non-parallel HCP plates interfered with one another during their growth, thereby preventing the complete transformation of the initial FCC grain to HCP. The overall number of lattice defects was reduced during the first few complete thermal cycles (recovery), transitioning the initial complex dislocation network into a more ordered array. Upon additional thermal cycling, the number of different HCP martensite plate orientations was reduced to a

single variant (took approximately 40 complete thermal cycles). This dominant HCP plate orientation was indicative of a fully reversible HCP-FCC transformation mediated by a solitary ordered array of perfect FCC dislocations (equivalent to two parallel arrays of HCP SPs) that dissociate into two ordered arrays of FCC SPs within a single grain. The region between these two SP arrays results in a stacking fault thereby transforming the FCC lattice into HCP.

Other investigations into the HCP-FCC transition in Co predating Bauer *et al*. (2011) [90] also observed a preferred HCP variant (referred to as "whiskers") and propose that the FCC to HCP transformation occurred on the particular set of parallel $\{111\}_{FCC}$ planes that align the whisker growth axes with the close-packed directions for both phases, i.e. $\langle 110\rangle_{FCC} \parallel \langle 11\bar{2}0\rangle_{HCP}$, and results in a HCP whisker with the densest possible *combination* of surface planes, i.e. planes which form the crystal faces parallel to the whisker axis [92–93]. The dominant HCP whisker observed by R.D. Dragsdorf (1962) [92] and R.T. Johnson, Jr. (1967) [93] had $\langle 2\bar{1}\bar{1}0\rangle_{HCP}$ directionality (initially $\langle 110\rangle_{FCC}$) and varying combinations of $(0002)_{HCP}$, $(01\bar{1}1)_{HCP}$, and $(01\bar{1}\bar{1})_{HCP}$ surface planes (or $(001)_{FCC}$, $(\bar{1}11)_{FCC}$, and $(1\bar{1}1)_{FCC}$ for the corresponding FCC whiskers). The FCC to HCP transformation was thought to occur on the $(\bar{1}11)_{FCC}$ or $(1\bar{1}1)_{FCC}$ planes for the $[110]_{FCC}$ grown whiskers, i.e. the growth direction was perpendicular to the slip plane. Additional (though very few) HCP whisker variants with $[11\bar{2}3]_{HCP}$, $[01\bar{1}2]_{HCP}$, $[\bar{1}101]_{HCP}$, and $[0001]_{HCP}$ axes were also found, which formed from $\langle 110\rangle_{FCC}$, $\langle 100\rangle_{FCC}$, and $\langle 111\rangle_{FCC}$ initial FCC whiskers. The resulting surface planes differed quite a bit between these variants (various combinations of different $(0002)_{HCP}$, $\{01\bar{1}1\}_{HCP}$, $\{11\bar{2}\bar{2}\}_{HCP}$, $\{\bar{2}110\}_{HCP}$, and $\{1\bar{1}00\}_{HCP}$), and it was concluded that the FCC to HCP transformations and resulting orientations of the HCP whiskers were not defined by one close-packed surface plane, but by the combination of *all* surface planes forming the whisker. Despite differences in whisker orientation and morphology, all FCC to HCP transformations were reported to have occurred on $\{111\}_{FCC}$ planes and mediated through the dissociation and glide of an axial screw dislocation into partial dislocations. It was proposed that the lattice strain associated with the axial screw dislocation would restrict the atomic shuffle to the $\{111\}_{FCC}$ planes most nearly parallel to the whisker axis during the FCC to HCP transformation, thereby decreasing strain and minimizing rotation in the lattice once the transformation was complete. Therefore, the strain associated with the axial screw dislocation and the imposed surface plane restraints, i.e. surface planes combinations that collectively generate the densest packing, work together to restrict the FCC to HCP transformation to only one of the four possible $\{111\}_{FCC}$ planes. This explains why a vast majority of the HCP whiskers observed by R.D. Dragsdorf [92] and R.T. Johnson, Jr. [93] were $\langle 2\bar{1}\bar{1}0\rangle_{HCP}$ type and why thermal cycling through the HCP-FCC transition temperature reduced the differently oriented HCP martensite plates observed by Bauer *et al*. [90] to a single variant.

Two types of dissociations were proposed by R.T. Johnson, Jr. [93] for the axial screw dislocation resulting in; 1) two SP dislocations ($\vec{\mathbf{b}}=1/6\langle 11\bar{2}\rangle_{FCC}$) for the dominant $\langle 2\bar{1}\bar{1}0\rangle_{HCP}$ HCP whisker variant, and 2) one SP and one Frank partial (FP) ($\vec{\mathbf{b}}=1/6\langle \bar{1}11\rangle_{FCC}$) for the more rare HCP whisker variants with $\langle 11\bar{2}3\rangle_{HCP}$, $\langle \bar{1}101\rangle_{HCP}$ and $\langle 01\bar{1}2\rangle_{HCP}$ whisker axes. In both scenarios, a SP slipped through the lattice completing the FCC to HCP transformation. A snapshot of Table V from R.T. Johnson, Jr. [93] listing the various dissociations of the axial screw dislocation is provided in Figure 5.3.

TABLE V. Formation of partial dislocations from the extension of the axial screw dislocation in cobalt whiskers.

Slip plane	Dislocation reaction relating Burgers vectors[a] (axial screw to two partials)	Resulting hcp whisker axes	Energy[b] ratio (partials to axial screw)
111	$\frac{1}{2}[110]=\frac{1}{3}[111]+\frac{1}{6}[11\bar{2}]$	$\bar{1}\bar{2}\cdot 2:\bar{1}\bar{1}\cdot 1$	1
$\bar{1}11$	$\frac{1}{2}[110]=\frac{1}{6}[12\bar{1}]+\frac{1}{6}[211]$	$\bar{1}0\cdot 0$	$\frac{2}{3}$
$1\bar{1}1$	$\frac{1}{2}[110]=\frac{1}{6}[121]+\frac{1}{6}[21\bar{1}]$	$10\cdot 0$	$\frac{2}{3}$
$11\bar{1}$	$\frac{1}{2}[110]=\frac{1}{3}[11\bar{1}]+\frac{1}{6}[112]$	$\bar{2}\bar{1}\cdot 2:\bar{1}\bar{1}\cdot 1$	1
111	$[100]=\frac{1}{3}[111]+\frac{1}{3}[2\bar{1}\bar{1}]$	$\bar{2}\bar{1}\cdot 1$	1
$\bar{1}11$	$[100]=\frac{1}{3}[1\bar{1}\bar{1}]+\frac{1}{3}[211]$	$\bar{1}1\cdot\bar{1}$	1
$1\bar{1}1$	$[100]=\frac{1}{3}[1\bar{1}1]+\frac{1}{3}[21\bar{1}]$	$1\bar{1}\cdot 1$	1
$11\bar{1}$	$[100]=\frac{1}{3}[11\bar{1}]+\frac{1}{3}[2\bar{1}1]$	$\bar{1}\bar{2}\cdot 1$	1

[a] ⟨211⟩ are slip directions and are parallel to the Burgers vectors of Shockley partial dislocations. ⟨111⟩ directions are parallel to the Burgers vectors of the Frank partial dislocations.

[b] The energy is approximated to be proportional to the square of the Burgers vector.[26]

Figure 5.3: Taken from R.T. Johnson, Jr. *et al.* (1967). *J. Appl. Phys.*, **38**(2), p. 625 [93]. The notation of resulting HCP whisker axes (first column only) corresponds to the conventional Miller Bravais notation for HCP in the following way. The translation for planes (second column only) is also provided for clarity and to show how the 3-to-4 index conversion for HCP directions and HCP planes are different:

$[10\cdot 0]_{HCP} = [2\bar{1}\bar{1}0]_{HCP}$ $\quad$ $(10\cdot 0)_{HCP} = (10\bar{1}0)_{HCP}$

$[\bar{1}0\cdot 0]_{HCP} = [\bar{2}110]_{HCP}$ $\quad$ $(\bar{1}0\cdot 0)_{HCP} = (\bar{1}010)_{HCP}$

$[\bar{1}\bar{2}\cdot 2]_{HCP} = [0\bar{1}12]_{HCP}$ $\quad$ $(\bar{1}\bar{2}\cdot 2)_{HCP} = (\bar{1}\bar{2}32)_{HCP}$

$[\bar{1}\bar{1}\cdot 1]_{HCP} = [\bar{1}\bar{1}23]_{HCP}$ $\quad$ $(\bar{1}\bar{1}\cdot 1)_{HCP} = (\bar{1}\bar{1}21)_{HCP}$

$[\bar{2}\bar{1}\cdot 2]_{HCP} = [\bar{1}012]_{HCP}$ $\quad$ $(\bar{2}\bar{1}\cdot 2)_{HCP} = (\bar{2}\bar{1}32)_{HCP}$

$[\bar{2}\bar{1}\cdot 1]_{HCP} = [\bar{1}011]_{HCP}$ $\quad$ $(\bar{2}\bar{1}\cdot 2)_{HCP} = (\bar{2}\bar{1}32)_{HCP}$

$[\bar{1}1\cdot\bar{1}]_{HCP} = [\bar{1}10\bar{1}]_{HCP}$ $\quad$ $(\bar{1}1\cdot\bar{1})_{HCP} = (\bar{1}10\bar{1})_{HCP}$

$[1\bar{1}\cdot 1]_{HCP} = [1\bar{1}01]_{HCP}$ $\quad$ $(1\bar{1}\cdot 1)_{HCP} = (1\bar{1}01)_{HCP}$

$[\bar{1}\bar{2}\cdot 1]_{HCP} = [0\bar{1}11]_{HCP}$ $\quad$ $(\bar{1}\bar{2}\cdot 1)_{HCP} = (\bar{1}\bar{2}31)_{HCP}$

The loss of the axial screw dislocation through its dissociation into two distinct SPs was predicted to be more energetically favorable than its dissociation into a single SP and FP. This was supported with the higher frequency in observations for the $\langle 2\bar{1}\bar{1}0\rangle_{HCP}$ whisker variant, which appeared to be straighter in morphology with little evidence of lattice rotation. Conversely, the other HCP whisker variants formed from a SP + FP were more twisted and distorted in appearance indicating left over strain from the axial screw dislocation in the form of a sessile FP. FPs have Burgers vectors normal to the glide plane rendering them sessile (pinned in the lattice) except through climb, whereas the Burgers vectors of the SPs lie in the transformation (slip) plane and are glissile. Therefore, the proposed SP + FP mediated FCC to HCP transformation mechanism for Co involves the glide of the SP through the lattice (lost at the surface) thereby transforming the crystal structure, and the immobilized FP forms the boundaries around the martensitic HCP whiskers and accounts for the residual strain left over from the axial screw dislocation.

For reasons unexplained, the dissociation reaction for the $[0001]_{HCP}$ type whisker was omitted from Table V (Figure 5.3) and the transformation mechanism resulting in this HCP whisker variant was not discussed. It was reported that only three out of the sixty whiskers investigated exhibited $[0001]_{HCP}$ growth axes were bound by $\{\bar{2}110\}_{HCP}$ type surface planes. Interestingly, these whiskers were helical in appearance, i.e. a $[0001]_{HCP}$ helical axis and $[2\bar{1}\bar{1}0]_{HCP}$ growth segments (arms), and demonstrated a lattice twist that corresponded to Burgers vectors of partial lattice periodicities in the $[0001]_{HCP}$ direction. A micrograph of a helical $[0001]_{HCP}$ type Co whisker taken by R.D. Dragsdorf [92] is provided in Figure 5.4 for clarity.

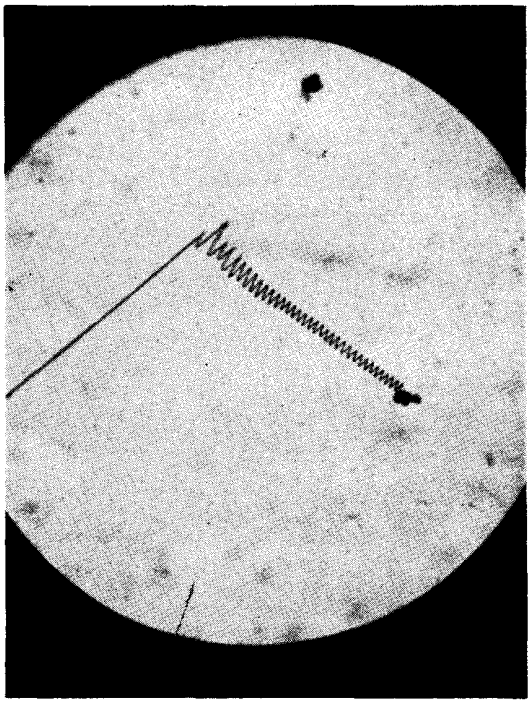

Figure 5.4: Taken from R.D. Dragsdorf *et al*. (1962). *J. Appl. Phys.*, **33**(2), p. 725 [92]. A helical cobalt whisker with a $[00{\cdot}1]_{HCP} = [0001]_{HCP}$ helical axis and $[10{\cdot}0]_{HCP} = [2\bar{1}\bar{1}0]_{HCP}$ growth segments. Each turn of the spiral has hexagonal geometry when viewed along the axis of the helix. The cross-sectional dimension of the initially straight portion of the whisker is 5μm. Note the extraneous material on the growth tip.

5.1.2. HCP – FCC Transformations in Titanium

Recently, a few investigations into FCC Ti have proposed HCP to FCC transformation mechanisms though there is some disagreement between them [55–58, 70]. The debate begins with Hong *et al*. (2013) [56] who experimentally observed a stress-induced FCC Ti phase in pure Ti TEM samples made from parallelepiped bulk samples (24mm x 24mm x 12mm) that were severely deformed via cryogenic channel-die compression. The FCC Ti phase was observed around intersecting slip bands and demonstrated the following relationships:

$$\langle 001\rangle_{FCC} \parallel \langle 0001\rangle_{HCP}$$
$$\langle 1\bar{1}0\rangle_{FCC} \parallel \langle 10\bar{1}0\rangle_{HCP}$$
$$\langle 110\rangle_{FCC} \parallel \langle 11\bar{2}0\rangle_{HCP}$$

These are identical to the directional orientations relationships found for the type III FCC Ti phase (strain-induced) discussed in chapter 4. They propose that SPs with $\vec{\mathbf{b}}=1/6\langle 11\bar{2}0\rangle_{HCP}$, i.e. half of the perfect HCP **a**-type dislocation ($\vec{\mathbf{b}}=1/3\langle 11\bar{2}0\rangle_{HCP}$), gliding on every other two $\{10\bar{1}0\}_{HCP}$ planes convert the HCP lattice into FCC. A schematic outlining the transformation mechanism proposed by Hong *et al*. [56] is presented in Figure 5.5 for convenience.

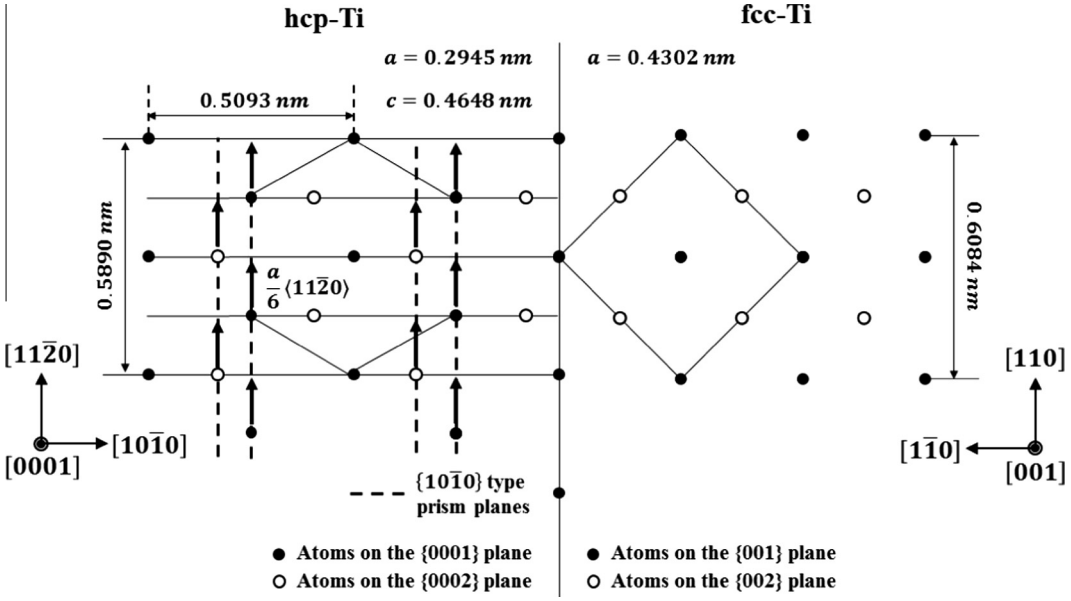

Figure 5.5: Taken from D.H. Hong *et al*. (2013). *Scripta Mater.*, **69**, p. 407 [56]. Schematic diagram of a transformation mechanism, in which glide of partial dislocations on prism planes result in an FCC structure from the original HCP phase.

This SP mediated HCP to FCC transformation mechanism was supported experimentally by Liu *et al*. (2016) [58] and Niu *et al*. (2017) [57], and through molecular dynamics (MD) simulations by Ren *et al*. (2017) [70]. Liu *et al*. [58] observed FCC Ti in TEM foils made from severely deformed bulk samples (via high energy shot peening) of the binary (α+β) alloy Ti-6Al-4V. FCC deformation nanotwins were also observed by within the FCC Ti phase, which were assumed to nucleate at grain boundaries, and grew via SPs emission from the grain boundary. Partial dislocation emission from grain boundaries was preferred to perfect dislocations due to the small grain sizes of the sample. It was proposed that these small grain size effects combined with the high strain rate imposed on the sample during deformation allowed for the high stresses necessary to initiate the transformation [58]. Similar findings were reported by Niu *et al*. (2017) [57] for 20μm thick CP Ti foils (3.3μm average grain size) under uniaxial tension loading. They add that the FCC Ti phase was concentrated near the fracture surfaces (propagating cracks) and present evidence of SPs with $\vec{\mathbf{b}}=1/6\langle 11\bar{2}0\rangle_{HCP}$ at the HCP-FCC interface [57]. MD simulations conducted by Ren *et al*. [70] investigated the temperature and strain rate dependences on the HCP-FCC transformation in simulated single-crystalline nanopillars under $\langle 0001\rangle_{HCP}$ uniaxial tensile loading. They report a double yielding phenomenon, where $\{10\bar{1}2\}_{HCP}$ $\langle 10\bar{1}1\rangle_{HCP}$ type

deformation twinning followed by FCC nucleation represent the first and second load drops in the stress strain curve, respectively. The FCC Ti phase formed from a group of high-density stacking faults within the deformation twin (accumulated through the continuous glide of multiple SPs) for lower tested temperatures (<107°C) and high strain rates (>10^8 s^{-1}). Perfect **a**-type dislocation on glide was activated on $\{10\bar{1}1\}_{HCP}$ planes or $\{10\bar{1}0\}_{HCP}$ planes when the MD simulation was ran above 107°C and below 10^8 s^{-1}, respectively. They conclude that the different deformation modes (i.e. perfect dislocation slip, deformation twinning, and SP mediated HCP to FCC transformation) can be activated or suppressed given the appropriate environmental and loading conditions [70]. The FCC Ti investigation conducted by Wu *et al*. (2016) [55] disagreed with the established HCP to FCC transformation mechanism proposed by Hong *et al*. (2013) [56] based on: 1) the gliding of SPs does not generate a lattice expansion normal to the phase boundary (corresponding to macroscopic transformation strain), 2) the sharp steps observed along the phase boundary can only form when the SPs are opposite in sign on every other two atomic planes, which was said to be unlikely, and 3) SP nucleation must occur at initiation sites such as grain boundaries, crack tips, or free surfaces (Hong *et al*. [56] showed FCC Ti features entirely within a grain). As such, it was concluded that FCC Ti nucleation was accomplished by a pure-shuffle mechanism (with a min stable thickness of three atomic layers) and growth was facilitated via a shear-shuffle mechanism (with a minimum growth unit of two atomic layers) [55]. However, this argument put forth by Wu *et al*. [55] seems less applicable to the strain induced FCC Ti phase discussed in chapter 4 since they were observed primarily around cracks and were accompanied by mobile dislocations during growth. Furthermore, all of the experimentally observed FCC Ti phases demonstrating the $(001)_{FCC} \parallel (0001)_{HCP}$ relationship [55–58] were found using TEM, none of which address the possibility of hydride contamination nor that FCC nucleation may have occurred during TEM sample preparation. Based on what was reported in their respective experimental methods (and supported with five and a half years of personal Ti TEM sample preparation experience), it is very probable that the FCC phase nucleated during TEM sample preparation, thereby invalidating Wu *et al*. [55] argument against nucleation initiation sites (i.e. the sample surface itself likely acted as a nucleation site for FCC Ti observations away from grain boundaries). Wu *et al*. [55] was correct in addressing that SP glide ($\vec{\mathbf{b}}=1/6\langle 11\bar{2}0\rangle_{HCP}$) on the $\{1\bar{1}00\}_{HCP}$ prism plane does not result in a lattice expansion normal to the $\{1\bar{1}00\}_{HCP}$ (i.e. boundary plane). However, SPs with $\vec{\mathbf{b}}=1/3\langle 1\bar{1}00\rangle_{HCP}$ gliding on the $\{01\bar{1}0\}_{HCP}$, $\{11\bar{2}0\}_{HCP}$, $\{0002\}_{HCP}$, or $\{1\bar{1}01\}_{HCP}$ planes do result in lattice expansions normal to $\{1\bar{1}00\}_{HCP}$.

5.2. Proposed HCP to FCC Transformation Mechanisms

After careful consideration of all of the arguments for and against a partial dislocation driven transformation, the following HCP to FCC transformation mechanisms are proposed for the three distinct FCC Ti phases investigated; mechanism I) the established SP driven mechanism for Co that aligns the closest-packed *planes* of the respective HCP and FCC phases, and mechanism II) a new model based on the FCC Ti type III experimental results and literature reports (discussed previously in this chapter) that aligns the closest-packed *directions* of the respective HCP and FCC phases.

5.2.1. Mechanism I – Alignment of the Close-Packed Planes

The horizontally oriented Ti-hydrides (FIB-induced FCC Ti, type I) and the thermally induced FCC Ti phase (FCC Ti type II) were observed to have the following orientation relationship to the parent HCP phase:

$$(1\bar{1}1)_{FCC} \parallel (0002)_{HCP}$$
$$[110]_{FCC} \parallel [11\bar{2}0]_{HCP}$$
$$[\bar{1}12]_{FCC} \parallel [01\bar{1}0]_{HCP}$$

This alignment of the closed-packed $(0002)_{HCP}$ and $\{111\}_{FCC}$ planes is presented schematically in Figure 5.6.

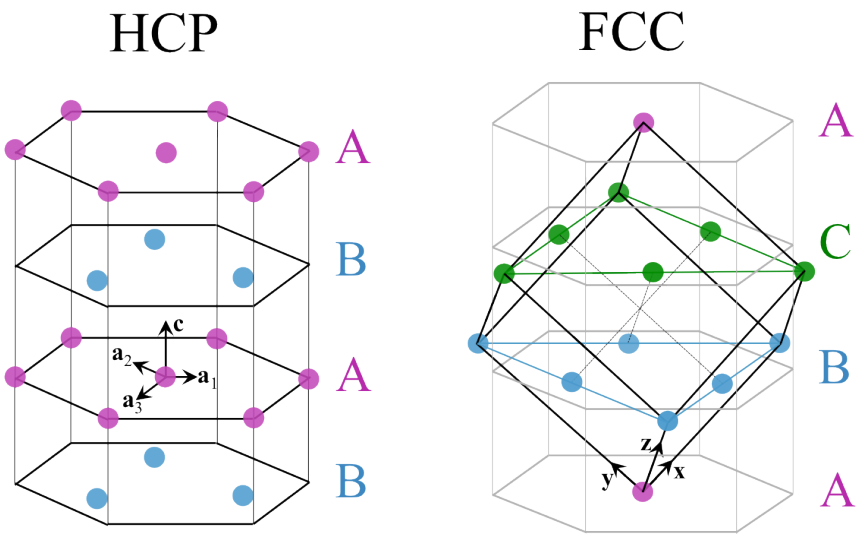

Figure 5.6: The HCP (left) and FCC (right) crystal structures oriented to one another by their respective close-packed planes. The FCC structure was drawn on top of the hexagonal prism (greyed out) to better show the orientation relationship between the two phases. The differently colored atoms represent individual close packed layers stacked on top of one another. The HCP and FCC structures adopt ABABAB and ABCABC type stacking sequences, respectively.

This type of HCP-FCC orientation relationship is well established commonly observed for Co, which exhibits the HCP and FCC crystal structures at low and high temperatures, respectively [90–93]. As discussed in detail in section 5.1.1, the transition from the FCC structure to HCP can be realized through the motion of Shockley partial (SP) dislocations ($\vec{\mathbf{b}}=1/6\langle 11\bar{2}\rangle_{FCC}$) gliding on every second closed-packed $(111)_{FCC}$ plane. The reverse transformation (HCP to FCC) is rarely depicted in the literature, likely due to the complexity of hexagonal coordinates, but this mechanism is believed to be completely reversible. The schematic of the FCC to HCP transformation created by Bauer *et al*. (2011) [90] (presented in Figure 5.1) was adapted for the HCP to FCC transition in Figure 5.7.

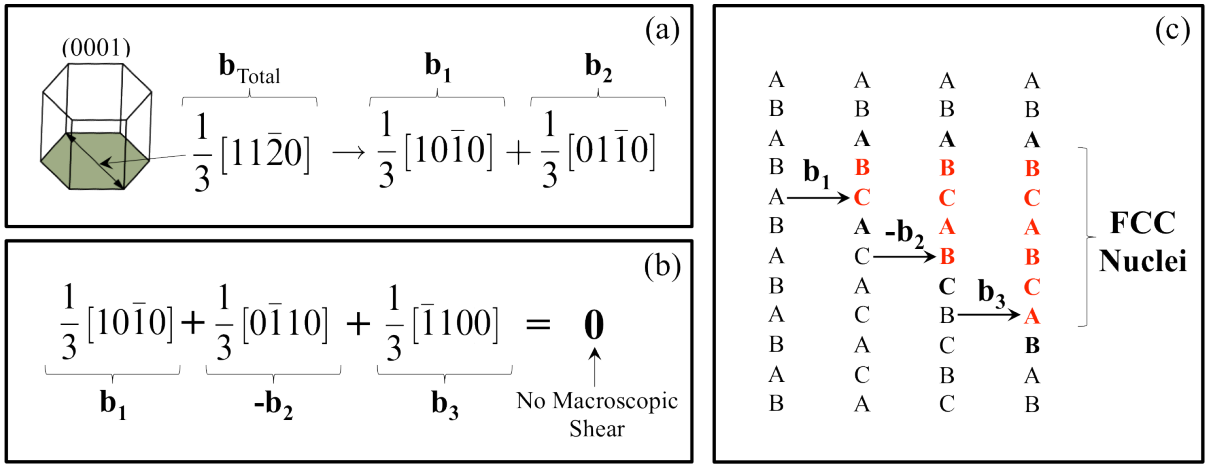

Figure 5.7: Adapted from Bauer *et al*. (2011). *Phil Mag.,* **91**(3), p. 441 [90]. (a) Schematic HCP **a**-type dislocation dissociations into SPs glissile on the close-packed $(0001)_{HCP}$. (b) and (c) show how the glide of multiple SPs on every other close-packed plane result in an FCC nuclei within the HCP stacking sequence without causing macroscopic shear (i.e. essential only for situations where lattice is confined and unable to change size and shape).

It should be mentioned that **a**-type dislocations in HCP Ti prefer to glide on the $\{1\bar{1}00\}_{HCP}$ prism planes instead of the $(0001)_{HCP}$ plane. In addition, high stacking fault energies (SFE) typically limit **a**-type dislocation dissociations, which would indicate that this type of transformation mechanism is unfavorable. However, it is suspected that external factors, such as vacancy clustering, high temperatures, and H and O contamination, promote basal slip and **a**-type dislocation dissociations into SPs.

As shown in chapter 3, thermal FCC Ti (type II) was found to be oxygen rich (nearly an order of magnitude higher O content in heated Ti TEM foils than non-heated foils), was plate-like in morphology with the flat faces corresponding to the $(0002)_{HCP}$ and $\{111\}_{FCC}$ planes, and preferentially precipitated within prism-oriented grains. Oxygen is a remarkable solid solution strengthener in HCP α-Ti and small editions can lead dramatic increases in strength at the cost of reduced ductility [94–95]. This effect is attributed to a change in the dislocation slip behavior (wavy to planar) and suppressed deformation twining. In addition, an increase in interstitial content tends to increase the c/a ratio for Ti (c/a = 1.587), which is below the ideal value (c/a = 1.633). FCC structures demonstrate ideal c/a ratios when drawn within a hexagonal prism (see Figure 5.6); therefore it is reasonable to suspect that high levels of oxygen can expand the HCP lattice and reduces the SFE associated with **a**-type dislocation slip on basal planes. Thermal FCC Ti was observed to nucleate at high temperatures (>600°C) and had strong directionality in growth. Short line segments preceded the FCC precipitates, though they could not be confirmed as dislocations during the time frame of the experiment. Thermally activated dislocations were observed moving throughout the sample well before the first FCC nucleation event and the sample bent quite significantly during *in situ* heating due to thermal expansion. In addition, the TEM sample itself was strained during sample preparation, as is evident by the large $\{11\bar{2}2\}_{HCP}$ $\langle 1\bar{1}00\rangle_{HCP}$ type compression twins found in the EBSD pattern of the foil (Figure 3.3). Therefore, it does seem plausible to assume that a ready source of dislocations and internal strain was already confined within the TEM sample prior to heating. Through the combined influences of strain, temperature, increased oxygen content, film thickness, and surface plane orientation

restrictions (discussed previously in section 5.1.1 in relation to martensite HCP Co whiskers), the thermally activated HCP to FCC transformation first observed by Q. Yu *et al*. (2017) [12] can be initiated in high purity Ti TEM foils and it is proposed that the transformation is accomplished by the dissociation of perfect **a**-type dislocations into SPs and their subsequent ordered glide on alternating close-packed planes .

Since vacancy accumulation was likely increased in the thinned micropillars due to FIB milling (i.e. knock-on damage [96–97]), an additional SP nucleation method is proposed for type I FCC Ti. Basal stacking faults (SF) can form when vacancies accumulate in a $(0001)_{HCP}$ plane (assume within an A layer in the ABABAB stacking sequence). As a consequence, two B layers will come into contact, forming a very unstable stacking sequence surrounded by a $1/2\langle 0001\rangle_{HCP}$ partial loop. This high-energy situation is avoided when $1/3\langle 1\bar{1}00\rangle_{HCP}$ type slip occurs in the basal planes adjacent to the fault. Two faulting mechanisms are possible resulting in either an extrinsic (E) or intrinsic (I) SF. For the ESF case, an adjacent B layer can move into C positions, which is the same as two $1/3\langle 1\bar{1}00\rangle_{HCP}$ SPs of opposite sign gliding above and below the missing A layer ultimately forming a sessile Frank partial dislocation (FP) with a Burgers vector $\vec{\mathbf{b}}=1/2\langle 0001\rangle_{HCP}$ surrounding the ESF [86]. The reaction can be written as:

$$1/2\langle 0001\rangle + 1/3\langle 1\bar{1}00\rangle + 1/3\langle \bar{1}100\rangle \rightarrow 1/2\langle 0001\rangle$$

The ISF mechanism involves only a single $1/3\langle 1\bar{1}00\rangle_{HCP}$ SP, which glides above the missing A layer, shifting B atoms to C sites, and A atoms to B sites. This creates a low-energy intrinsic stacking fault encircled by a $1/6\langle \bar{2}203\rangle_{HCP}$ sessile FP [86]. These faulting mechanisms were drawn schematically by Hull *et al*. (2001) [86] and are presented in Figure 5.8 for clarity.

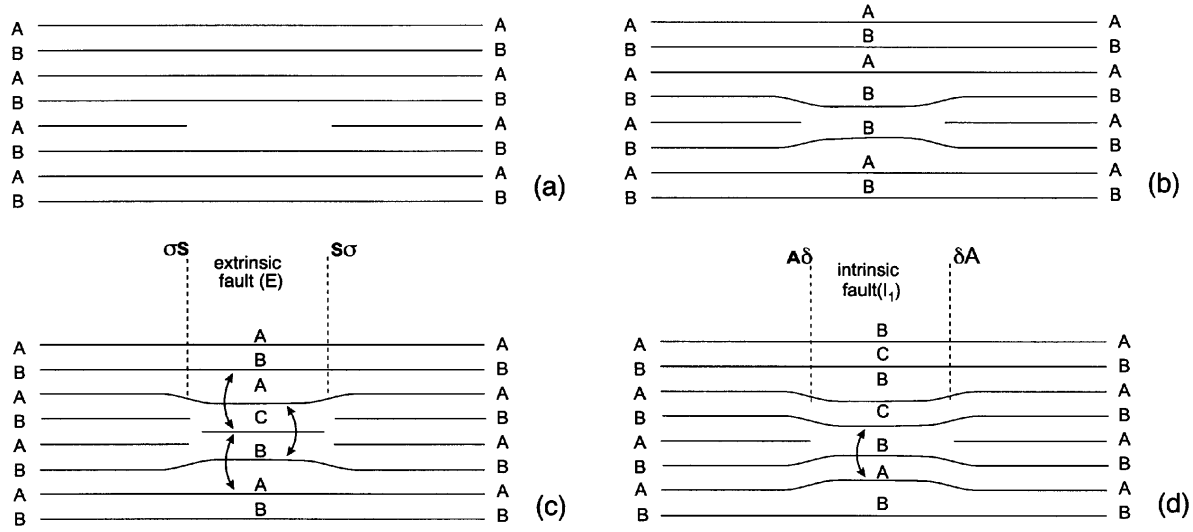

Figure 5.8: Taken from Hull *et al*. (2001). *Introduction to Dislocations, Fourth Edition*, p. 107 [86]. Formation of Frank sessile dislocation loops as a consequence of vacancy clustering. See Appendix A.2.1 for more detail.

Since the ion beam was directed along the $\langle 0001\rangle_{HCP}$ during sample thinning via FIB, it is suspected that a high density of vacancies accumulated particularly within the $(0001)_{HCP}$ planes

thereby creating the defects needed to drive the transformation. These same defects were likely utilized for the second HCP to FCC transformation mechanism (discussed next), where the close packed planes are not preferentially aligned.

5.2.2. Mechanism II – Alignment of the Close-Packed Directions

The more vertically oriented Ti-hydrides (FIB-induced FCC Ti, type I) and the strain induced (type III) FCC Ti phases demonstrated the following orientation relationship (refer to Figure 4.6 for a 2D illustration of the orientation arrangement):

$$(001)_{FCC} \parallel (0001)_{HCP}$$
$$(1\bar{1}0)_{FCC} \parallel (1\bar{1}00)_{HCP}$$
$$[\bar{1}\bar{1}0]_{FCC} \parallel [\bar{1}\bar{1}20]_{HCP}$$

The mechanism proposed by D.H. Hong *et al*. [56] (see Figure 5.5) does produce the observed orientation relationship indicated in Figure 4.6, however, it seems incomplete since it does not account for the change in spacing of the parallel interface planes, $(1\bar{1}00)_{HCP} \parallel (1\bar{1}0)_{FCC}$, between the two phases. Furthermore, the high frequency of FCC deformation twins and rotated appearance of the type III FCC Ti phase indicates that additional deformation mechanisms might be at play. Though it is still a bit in the early stages of development, the proposed mechanism for this HCP to FCC transformation combines the theories suggested by D.H. Hong *et al*. (2013) and R.D. Dragsdorf *et al*. (1962) (discussed in detail in section 5.1) and involves the dissociation of perfect HCP **a**-type axial screw dislocations into SPs and FPs.

These $[0001]_{HCP}$ Co whisker variants discussed by R.D. Dragsdorf *et al*. (1962) and R.T. Johnson, Jr. *et al*. (1967) were most similar in morphology to the strain induced FCC Ti phase and were helical in appearance, i.e. a $[0001]_{HCP}$ helical axis and $[2\bar{1}\bar{1}0]_{HCP}$ growth segments (arms), and demonstrated a lattice twist that corresponded to Burgers vectors of partial lattice periodicities in the $[0001]_{HCP}$ direction. Each turn of the helix had hexagonal geometry when viewed along the $[0001]_{HCP}$. It thought that these arms could be related to the FCC deformation twinning events observed in the type III FCC Ti phase and may be a product of the continuing lattice distortion along the $[0001]_{HCP}$. If we initially assume that the $[2\bar{1}\bar{1}0]_{HCP}$ and $[100]_{FCC}$ axes are aligned, then the base of the square that makes up the $(002)_{FCC}$ plane in the FCC unit cell must rotate ~14-15° about the $[0001]_{HCP}$ to align the diagonals of the cube (i.e. *both* FCC close-packed directions) to a pair of normal $\langle 2\bar{1}\bar{1}0\rangle_{HCP}$ and $\langle 01\bar{1}0\rangle_{HCP}$ directions, i.e. the orientation presented in Figure 4.6. When following the atomic plane indicated in Figure 4.12(b), $(0002)_{HCP}$ to $(002)_{FCC}$ to $(1\bar{1}1)_{FCC}$, the plane appears to bend at the FCC-FCC_{Twin} with a measured angle of about ~14-15°. If you think about this while considering Figure 4.6, the FCC twin changes the square blue squares back into hexagons so it reasonable to think that HCP to FCC and FCC to FCC_{Twin} are accomplished by similar (or the same) mechanism, which causes lattice rotations about the $[0001]_{HCP}$. This type of lattice rotation can be accomplished by an axial screw dislocation. It is proposed that the dissociation of this type of screw dislocation into SPs and FPs facilitates the HCP to FCC transformation in Ti, where the lattice is transformed during glide of the SP (lost to surface of the TEM foil) and the FP forms the boundaries of the FCC phase and promotes FCC deformation twinning events. Additional work is needed to

conclude which type of SPs gliding on which planes work with the FPs to generate this HCP-FCC phase relationship and finalize this mechanism II theory.

5.3. Summary

A hexagonal-close packed (HCP) to face-centered cubic (FCC) phase transition has been observed in freestanding alpha-titanium thin foils under three separate conditions: Type I – upon focused ion beam (FIB) irradiation, Type II – during *in situ* heating in a transmission electron microscope (TEM), and Type III – during *in situ* TEM straining. A summary of the physical properties for each FCC Ti type discussed in the present investigation is provided in Table 5.1.

Table 5.1: Summary of the conditions that form each FCC Ti variant and their observed FCC lattice parameters (a_{FCC}), orientation relationships (OR) with the HCP parent phase, and predicted dislocation mediated transformation mechanism.

FCC Type	Formation Condition	a_{FCC} [Å]	OR w. HCP	Proposed Mechanism
I	FIB Milling	4.40 ± 0.05	$(1\bar{1}1)_{FCC} \parallel (0002)_{HCP}$ $[\bar{1}12]_{FCC} \parallel [01\bar{1}0]_{HCP}$	Closed Packed Planes
			&	
			$(002)_{FCC} \parallel (0002)_{HCP}$ $[1\bar{1}0]_{FCC} \parallel [01\bar{1}0]_{HCP}$	Closed Packed Directions
II	*in situ* TEM heating	4.20 ± 0.07	$(11\bar{1})_{FCC} \parallel (0002)_{HCP}$ $[011]_{FCC} \parallel [2\bar{1}\bar{1}0]_{HCP}$	Closed Packed Planes
III	*in situ* TEM straining	4.17 ± 0.02	$(002)_{FCC} \parallel (0002)_{HCP}$ $(1\bar{1}0)_{FCC} \parallel (1\bar{1}00)_{HCP}$ $[\bar{1}\bar{1}0]_{FCC} \parallel [\bar{1}\bar{1}20]_{HCP}$	Closed Packed Directions

The differences between each FCC Ti type outlined in Table 5.1 and the wide range of reported lattice parameters in the literature (see Table 1.1) indicate that not all FCC Ti observations are of the same phase. Analytical and *in situ* electron microscopy combined with atom probe tomography (APT) have revealed that type I FCC Ti was comprised of both the δ-TiH_2 and γ-TiH_x hydrides, whereas type II FCC Ti was believed to be a precursor to γ-TiO_x. Chemical assessment of Type III FCC Ti suggested that this particular FCC phase was neither hydride nor oxide; however, the true oxygen content could not be accurately measured. It was suspected that type III may have contained higher levels of oxygen and/or hydrogen than the starting HCP bulk material due to contamination during sample preparation, however, these were also suspected to be far less than the H and O contents measured in types I and II. Based on the findings presented in this investigation and FCC reports found in the literature, it is believed that the variability in measured FCC phase lattice parameters were largely due to the prolonged absorption of hydrogen or oxygen (or both) into the TEM foil. The type of mechanism by which the HCP to

FCC transformation is mediated also likely affects the final FCC lattice parameter since different HCP-FCC orientation relationships can be generated for a given mechanism. The two transformation mechanisms proposed in the present investigation involve the dissociation of perfect HCP **a**-type dislocations into partial dislocations and their subsequent ordered glide cause an alignment of the closed-packed planes, i.e. $(0002)_{HCP} \parallel \{1\bar{1}1\}_{FCC}$, or alignment of both FCC closed-packed directions to the HCP directions; $[1\bar{1}00]_{HCP} \parallel [1\bar{1}0]_{FCC}$ and $[\bar{1}\bar{1}20]_{HCP} \parallel [\bar{1}\bar{1}0]_{FCC}$. The first is identical to the mechanism proposed for cobalt [90], where the **a**-type dislocation dissociates into two SPs, and the latter involves a dissociation of an axial screw **a**-type dislocation into a SP and a FP. Though, the exact dissociation reaction for this second mechanism is not yet finalized, a lattice rotation of approximately 14-15° is apparent, and the series of transformations observed in the type III; HCP-to-FCC, and FCC-to-FCC_{twin}, help accommodate strains along the $\langle 0001 \rangle_{HCP}$. To date, a vast majority of FCC Ti observations have been from thin films and there is little evidence (that does not involve TEM samples) of FCC Ti within bulk materials. However, the adjustable parameters that promote FCC Ti nucleation in films, such as small grain size, high temperatures, high stress state/degree of defect accumulation, and increased solute content, are only more recently coming to light. Some combinations of these parameters may yet result in a bulk FCC Ti phase, providing a whole new phase of titanium to incorporate into already complex microstructures thereby increasing the versatility of these impressive alloys even further.

References

[1] Lutjering, G. & Williams, J.C. (2007). *Titanium, Second Edition*. Berlin, Germany: Springer-Verlag.

[2] Hennig, R.G., Trinkle, D.R., Bouchet, J., Srinivasan, S.G., Albers, R.C. & Wilkins, J.W. (2005). Impurities block the alpha to omega martensitic transformation in titanium. *Nat. Mater.*, **4**, p. 129-133.

[3] Banerjee, S. & Mukhopadhyay, P. (2007). *Phase Transformations: Examples from Titanium and Zirconium Alloys, First Edition*. Amsterdam, The Netherlands: Elsevier Ltd.

[4] Banerjee, D. & Williams, J.C. (2013). Perspectives on titanium science and technology. *Acta Mater.*, **61**, p. 844-879.

[5] Trinkle, D. (2003). A theoretical study of the hcp to omega martensitic phase transition in titanium. *The Ohio State University*. (Doctoral dissertation).

[6] Jing, R., Liang, S.X., Liu, C.Y., Ma, M.Z. & Liu, R.P. (2013). Aging effects on the microstructures and mechanical properties of the Ti-20Zr-6.5Al-4V alloy. *Mater. Sci. Eng. A*, **559**(1), p. 474-479.

[7] Jing, R., Liu, C.Y., Ma, M.Z. & Liu, R.P. (2013). Microstructural evolution and formation mechanism of FCC titanium during heat treatment processing. *J. Alloys Compd.*, **552**, p. 202-207.

[8] Bolokang, A.S., Phasha, M.J., Motaung, D.E., Cummings, F.R., Muller, T.F.G. & Arendse, C.J. (2014). Microstructure and phase transformation on milled and unmilled Ti induced by water quenching. *Mater. Lett.*, **132**(1), p. 157-161.

[9] Rhodes, C.G. & Williams, J. C. (1975). Observations of an interface phase in the α/β boundaries in titanium alloys. *Metall. Trans. A.,* **6A**, p. 1670-1671.

[10] Rhodes, C.G. & Paton N.E. (1979). The influence of α/β interface phase on tensile properties of Ti-6Al-4V. *Metall. Trans. A.,* **10A**, p. 1753-1758.

[11] Rhodes, C.G. & Paton N.E. (1979). Formation characteristics of the α/β interface phase in Ti-6Al-4V. *Metall. Trans. A.,* **10A**, p. 209-216.

[12] Yu, Q., Kacher, J., Gammer, C., Traylor, R., Samanta, A., Yang, Z. & Minor, A.M. (2017). In situ TEM observation of FCC Ti formation at elevated temperatures. *Scripta Mater.,* **140**, p. 9-12.

[13] Wawner, Jr., F.E. & Lawless, K.R. (1969). Epitaxial growth of titanium thin films. *J. Vac. Sci. Technol.,* **6**, p. 588-590.

[14] Yamada, Y. & Yoshida, K. (1988). Growth and structure of titanium evaporated films. *Appl. Surf. Sci.* **33/34**, p. 465-471.

[15] Yue, L.P., Yao, W.G., Qi, Z.Z. & He, Y.Z. (1994). Structure of nanometer-size crystalline Ti film. *Nanostruct. Mater.,* **4**(4), p. 451-.456.

[16] Kim, S.K., Jona, F. & Marcus, P.M. (1996). Growth of face-centered-cubic titanium on aluminum. *J. Phys. Condens. Matter.,* **8**, p. 25-36.

[17] Chakraborty, J., Kumar, K., Ranjan, R., Chowdhury, S.G. & Singh, S.R. (2011). Thickness-dependent fcc-hcp phase transformation in polycrystalline titanium thin films. *Acta Mater.,* **59**(7), p. 2615-2623.

[18] Fazio, M., Vega, D., Kleiman, A., Colombo, D., Franco Arias, .M. & Márquez, A. (2015). Study of the structure of titanium thin films deposited with a vacuum arc as a function of the thickness. *Thin Solid Films,* **593**, p. 110-115.

[19] Arshi, N., Lu, J., Lee, C.G., Yoon, J.H., Koo, B.H. & Ahmed, F. (2013). Thickness effect on properties of titanium film deposited by d.c. magnetron sputtering and electron beam evaporation techniques. *Bull. Mater. Sci.,* **36**(5), p. 807-812.

[20] Svalov, A.V., Kurlyandskaya, G.V., Asensio, B.G., Collantes, J.M. & Larrañaga, A. (2015). Tuning the structure and magnetic softness of thin permalloy films by variations in the thickness of titanium seed layer. *Mater. Lett.,* **152**, p. 159-162.

[21] Sugawara, Y., Shibata, N., Hara, S. & Ikuhara, Y. (2000). Interface structure of face-centered-cubic-Ti thin film grown on 6H-SiC substrate. *J. Mater. Res.,* **15**(10), p. 2121-2124.

[22] Smith, R.J., Kim, Y.W., Shivaparan, N.R., White, G.A. & Teter, M.A. (1999). Growth of thin Ti films on Al single-crystal surfaces at room temperature. *Surf. Interface Anal.,* **27**, p. 185-193.

[23] Saleh, A.A, Shutthanandan, V. & Smith, R.J. (1993). Growth of thin Ti films on Al(110) surfaces. *J. Vac. Sci. Technol., A*, **11**, p. 1982-1986.

[24] Saleh, A.A., Shutthanandan, V. & Smith, R.J. (1994). Observation of ultrathin metastable fcc Ti films on Al(110) surfaces. *Phys. Rev. B: Condens. Matter*, **49**(7), p. 4908-4914.

[25] Saleh, A.A., Shutthanandan, V., Shivaparan, N.R. & Smith, R.J. (1997). Epitaxial growth of fcc Ti films on Al(001) surfaces. *Phys. Rev. B: Condens. Matter*, **56**(15), p. 9841-9847.

[26] Wang, L., Mohammed, F.M. & Adesida, I. (2007). Differences in the reaction kinetics and contact formation mechanisms of annealed Ti/Al/Mo/Au Ohmic contacts on n-GaN and AlGaN/GaN epilayers. *J. Appl. Phys.*, **101**, id. 24370, p. 1-11.

[27] Lu, C.J., Davydov, A.V., Josell, D. & Bendersky, L.A. (2003). Interfacial reactions of Ti/n-GaN contacts at elevated temperature. *J. Appl. Phys.*, **94**(1), p. 245-253.

[28] Harada, T. & Ohkoshi, H. (1997). Growth and structure of Ti films deposited on chemically polished MgO(100) substrate. *J. Cryst. Growth.*, **171**(1-2), p. 433-441.

[29] Harada, T. & Ohkoshi, H. (1997). Influence of MgO(100) substrate surfaces on epitaxial growth of Ti films. *J. Cryst. Growth.*, **173**(1-2), p. 109-116.

[30] Yamada, Y., Kasukabe, Y. & Yoshida, K. (1990). Cubic crystals in Ti films evaporated on NaCl substrates. *Jpn. J. Appl. Phys*., **29**, p. 706-709.

[31] Yamada, Y., Kasukabe, Y. & Nagata, S. (1990). Spontaneous hydrogenation of Ti films evaporated on NaCl Substrates I. *Jpn. J. Appl. Phys*., **29**, p. L1888-L1891.

[32] Kasukabe, Y. & Yamada, Y. (1990). Spontaneous hydrogenation of Ti films evaporated on NaCl Substrates II. *Jpn. J. Appl. Phys*., **29**, p. L1904-L1906.

[33] Kado, T. (2000). Structure of Ti films deposited on MgO(001) substrates. *Surf. Sci*., **454-456**, p. 783-789.

[34] Jankowski, A.F. & Wall, M.A. (1994). Formation of face-centered cubic titanium on a Ni single crystal and in Ni/Ti multilayers. *J. Mater. Res.,* **9**(1), p. 31-38.

[35] Jankowski, A.F. & Wall, M.A. (1996). Synthesis and characterization of nanophase face-centered-cubic titanium. *Nanostruct. Mater.,* **7**(1/2), p. 89-94.

[36] Josell, D., Shechtman, D. & Van Heerden, D. (1995). Fcc titanium in Ti/Ni multilayers. *Mater. Lett.,* **22**, p. 275-279.

[37] Banerjee, R., Dregia, S.A. & Fraser, H.L. (1995). Stability of FCC titanium in titanium/aluminum multilayers. *Acta Mater*., **47**(15), p. 4225-4231.

[38] Ahuja, R. & Fraser, H.L. (1994). Microstructural transitions in titanium-aluminum thin film multilayers. *J. Electron. Mater.,* **23**(10), p. 1027-1034.

[39] Ahuja, R. (1994). The synthesis, structure and properties of titanium-aluminum multiayered thin films. *The Ohio State University*. (Doctoral dissertation).

[40] Banerjee, R., Ahuja, R. & Fraser, H.L. (1996). Dimensionally induced structural transformations in titanium-aluminum multilayers. *Phys. Rev. Lett*., **76**(20), p. 3778-3781.

[41] Bonevich, J., van Heerden, D. & Josell, D. (1999). Face-centered-cubic titanium: an artifact in titanium/aluminum multilayers. *J. Mater. Res*., **14**(5), p. 1977-1981.

[42] Bonevich, J. & Josell, D. (1999). Comment on "Dimensionally Induced Structural Transformations in Titanium-Aluminum Multilayers." *Phys. Rev. Lett.*, **82**(9), p. 2002.

[43] Banerjee, R., Ahuja, R. & Fraser, H.L. (1999). Banerjee, Ahuja, and Fraser Reply. *Phys. Rev. Lett*., **82**(9), p. 2002.

[44] Banerjee, R. (2014). *Thin Films: Structural Transitions, Dekker Encyclopedia of Nanoscience and Nanotechnology, Third Edition*. Taylor & Francis., p. 4920-4930.

[45] Shechtman, D., Van Heerden, D. & Josell, D. (1994). Fcc titanium in Ti-Al multilayers. *Mater. Lett.,* **20**, p. 329-334.

[46] Van Heerden, D., Josell, D. & Shechtman, D. (1996). The formation of f.c.c. titanium in titanium-aluminum multilayers. *Acta. Mater.,* **44**(1), p. 297-306.

[47] Tepper, T., Shechtman, D., Van Heerden, D. & Josell, D. (1997). Fcc titanium in titanium/silver multilayers. *Mater. Lett.,* **33**, p. 181-184.

[48] Tepper, T., Shechtman, D., Van Heerden, D. & Josell, D. (1998). Allotropic phase formation in Ti/Zr multilayers. *Mater. Lett*., **35**(1-2), p. 100-107.

[49] Lai, J.B., Chen, L.J. Liu, C.S. (1999). Ion beam induced formation of metastable fcc-Ti phase in the epitaxial Ti/Cu(111)Si structures. *Micron*, **30**(3), p. 205-211.

[50] Zhang, D.L. & Ying, D.Y. (2002). Formation of fcc titanium during heating high energy ball milled Al-Ti powders. *Mater. Lett.,* **52**(4-5), p. 329-333.

[51] Chatterjee, P. & Sen Gupta, S.P. (2001). An x-ray diffraction study of nanocrystalline titanium prepared by high-energy vibrational ball milling. *Appl. Surf. Sci.,* **182**(3-4), p. 372-376.

[52] Manna, I., Chattopadhyay, P.P., Nandi, P., Banhart, F. & Fecht, H.J. (2003). Formation of face-centered-cubic titanium by mechanical attrition. *J. Appl. Phys.,* **93**(3), p. 1520-1524.

[53] Vullum, P.E., Pitt, M., Walmsley, J., Hauback, B. & Holmestad, R. (2009). Observations of nanoscopic, face centered cubic Ti and TiH_x. *Appl. Phys. A*, **94**(4), p. 787-793.

[54] Sarkar, R., Ghosal, P., Prasad, K.S., Nandy, T.K. & Ray, K.K. (2014). An fcc phase in a metastable β-titanium alloy. *Phil. Mag. Lett.,* **94**(5), p. 311-318.

[55] Wu, H.C., Kumar, A., Wang, J., Bi, X.F., Tomé, C.N., Zhang, Z. & Mao, S.X. (2016). Rolling-induced face centered cubic titanium in hexagonal close packed titanium at room temperature. *Sci. Rep.*, **6**(1), id. 24370, p. 1-8.

[56] Hong, D.H., Lee, T.W., Lim, S.H., Kim, W.Y. & Hwang, S.K. (2013). Stress-induced hexagonal close-packed to face-centered cubic phase transformation in commercial-purity titanium under cryogenic plane-strain compression. *Scripta Mater.*, **69**, p. 405-408.

[57] Niu, L., Wang, S., Chen, C., Qian, S.F., Liu, R., Li, H., Liao, B., Zhong, Z.H., Lu, P., Wang, M.P., Li, P., Wu, Y.C. & Cao, L.F. (2017). Mechanical behavior and deformation mechanism of commercial pure titanium foils. *Mater. Sci. Eng. A*, **707**, p. 435-442.

[58] Liu, Y.G., Li, M.Q. & Liu, H.J. (2016). Deformation induced face-centered cubic titanium and its twinning behavior in Ti-6Al-4V. *Scripta Mater.*, **119**, p. 5-8.

[59] Ito, M., Setoyama, D., Matsunaga, J., Muta, H., Kurosaki, K., Uno, M. & Yamanaka, S. (2006). Electrical and thermal properties of titanium hydrides. *J. Alloys Compd.*, **420**, p. 25-28.

[60] Gardiner, R.W. & Partridge, P.G. (1967). Preparation of thin foils of titanium and titanium alloys for transmission electron microscopy. *J. Sci. Instrum*., **44**, p. 63-65.

[61] Spurling, R.A., Rhodes, C.G. & Williams, J.C. (1974). The microstructure of Ti alloys as influenced by thin-foil artifacts. *Metall. Trans.*, **5**, p. 2597-2600.

[62] Banerjee, D., Shelton, C. G., Ralph, B. & Williams, J. C. (1988). A resolution of the interface phase problem in titanium alloys. *Acta Metall.,* **36**(1), p. 121-141.

[63] Woo, O.T., Weatherly, G.C. & Coleman, C.E. (1985). The precipitation of gamma-deuterides (hydrides) in titanium. *Acta Metall*., **33**(10). p. 1897-1906.

[64] Numakura, H. & Koiwa, M. (1984). Hydride precipitation in titanium. *Acta Metall*., **32**(10). p. 1799-1807.

[65] Bourret, A, Lasalmonie, A. & Naka, S. (1986). In-situ high resolution observation of hydride precipitation in titanium. *Scripta Metall.*, **20**, p. 861-866.

[66] Chen, C.Q., Li, S.X. & Lu, K. (2003). The deformation behaviors of gamma hydrides in titanium under cyclic straining. *Acta Mater.*, **51**, p. 931-942.

[67] Li, Z., Ou, P., Sun, N., Li, Z. & Shan, A. (2013). Face-centered tetragonal titanium hydrides in fine-grained commercial pure (grade 2) titanium. *Mater. Lett.*, **105**, p. 16-19.

[68] Aguayo, A., Murrieta, G. & de Coss, R. (2002). Elastic stability and electronic structure of fcc Ti, Zr, and Hf: a first-principles study. *Phys. Rev. B*., **65**, p. 1-4.

[69] Ren, J., Sun, Q., Xiao, L. & Sun, J. (2017). Temperature and strain rate effect of the deformation-induced phase transformation in pure titanium nanopillars oriented along [0001]. *Comput. Mater. Sci*., **126**, p. 66-73.

[70] Ren, J., Sun, Q., Xiao, L., Ding, X. & Sun, J. (2014). Phase transformation behavior in titanium single-crystal nanopillars under [0001] orientation tension: a molecular dynamics simulation. *Comput. Mater. Sci.*, **92**, p. 8-12.

[71] Xiong, S., Qi, W., Huang, B., Wang, M. & Li, Y. (2010). Size and shape dependent gibbs free energy and phase stability of titanium and zirconium nanoparticles. *Mater. Chem. and Phys*., **120**, p. 446-451.

[72] Xiong, S., Qi, W., Huang, B., Wang, M., Li, Y., Li, Z. & Liang, S. (2011). Size- and temperature-induced phase transformations of titanium nanoparticles. *EPL*, **93**, p. 1-4.

[73] Chen, Z.P., Wen, Z. & Jiang, Q. (2004) Phase stabilities of fcc ti nanocrystals. *Solid State Commun*., **132**, p. 747-750.

[74] Marcus, P.M. & Jona, F. (1997). Identification of metastable phases: face-centered cubic Ti. *J. Phys. Condens. Matter.*, **9**, p. 6241-6246.

[75] The Boeing Company: Gammon, L.M, Briggs, R.D., Packard, J.M., Batson, K.W., Boyer, R. & Domby, C.W. (2004). Metallography and Microstrutures of Titanium and Its Alloys. *ASM Handbook*, **9**, p. 899-917.

[76] Geiss, R. H., Rice, K. P. & Keller, R. R. (May 2013). Transmission EBSD in the scanning electron microscope. *Microscopy Today*, p. 16-20.

[77] Matysina, Z. A. & Shchur, D. V. (2001). Phase transformations $\alpha \rightarrow \beta \rightarrow \gamma \rightarrow \delta \rightarrow \varepsilon$ in titanium hydride TiH_x with increase in hydrogen concentration. *Russ. Phys. J.,* **44**(11), p. 1237-1243.

[78] Ngo, P.D. (1999). Energy Dispersive Spectroscopy, *Failure Analysis of Integrated Circuits-Tools and Techniques*. Ed. Lawrence C. Wagner. Springer, New York.

[79] Egerton, R.F. (1986). *Electron Energy-Loss Spectroscopy in the Electron Microscope. Third Edition*. Springer, New York Dordrecht Heidelberg London.

[80] Sundell, G., Thuvander, M. & Andren, H.O. (2013). Hydrogen analysis in APT: Methods to control adsorption and dissociation of H_2. *Ultramicroscopy*, **132**, p. 285-289.

[81] Chen, Y.S., Haley, D., Gerstl, S.A., London, A.J., Sweeny, F., Wepf, R.A., Rainforth, W.M., Bagot, P.A.J. & Moody, M.P. (2017). Direct observation of individual hydrogen atoms at trapping sites in a ferritic steel. *Science*, **355**, p. 1196-1199.

[82] McKenzie, W.R., Marquis, E.A. & Munroe, P.R. (2010). Focused ion beam sample preparation for atom probe tomography. *Microscopy: Science and Technology, Applications and Education*, Mendez, A. & Diaz, J. (Eds). p. 1800-1810.

[83] Fitzner, A., Prakash, D.G.L., da Fonseca, J.Q., Thomas, M., Zhang, S., Kelleher, J. Manuel, P. & Preuss, M. (2016). The effect of aluminum on twinning in binary alpha-titanium. *Acta. Mater*., **103**, p. 341-351.

[84] Gammer, C., Ozdol, V.B., Liebscher, C.H. & Minor, A.M. (2015) Diffraction contrast imaging using virtual apertures. *Ultramicroscopy*, **155**, p. 1-10.

[85] Ozdol, V.B., Gammer, C., Jin, X.G., Ercius, P., Ophus, C., Ciston, J. & Minor, A.M. (2015) Strain mapping at nanometer resolution using advanced nano-beam electron diffraction. *Appl. Phys. Lett.*, **106**, id. 253107, p. 1-10.

[86] Hull, D., & Bacon, D. J. (2001). *Introduction to Dislocations, Fourth Edition*. Oxford, England: Pergamon.

[87] Fultz, B. & Howe, J.M. (2008). *Transmission Electron Microscopy and Diffractometry of Materials, Third Edition*. Springer-Verlag Berlin Heidelberg.

[88] Williams, D.B. & Carter, C.B. (2009). *Transmission Electron Microscopy: A Textbook for Materials Science, Second Edition*. Springer, New York, NY.

[89] Niewczas, M. (2007). Chapter 75 Dislocations and Twinning in Face Centred Cubic Crystals. *Dislocations in Solids*. **13**. p. 263-364. 10.1016/S1572-4859(07)80007-6.

[90] Bauer, R., Jägle, E. A., Baumann, W. & Mittemeijer, E. J. (2011). Kinetics of the allotropic hcp–fcc phase transformation in cobalt. *Phil Mag.,* **91**(3), p. 437-457.

[91] Sebilleau, F. & Bibring, H. (eds), (1955). *The Mechanism of Phase Transformation in Metals*, **18**, Institute of Metals, London, p. 209.

[92] Dragsdorf, R.D. & Johnson Jr., R.T. (1962). Parallel dislocations in cobalt whiskers. *J. Appl. Phys.*, **33**(2), p. 724-728.

[93] Johnson Jr., R.T. & Dragsdorf, R.D. (1967). The martensitic transformation in cobalt. *J. Appl. Phys.*, **38**(2), p. 618-626.

[94] Conrad, H. (1981). Effect of interstitial solutes on the strength and ductility of titanium. *Prog. Mater. Sci.,* **26**(2-4), p. 123-403.

[95] Yu, Q. Qi, L., Tsuru, T., Traylor, R., Rugg, D., Morris Jr., J.W., Asta, M., Chrzan, D.C. & Minor, A.M. (2015). Origin of dramatic oxygen solute strengthening effect in titanium. Science, 347(6222), p. 635-639.

[96] Kim, S., Park, M. J., Balsara, N. P., Liu, G. & Minor, A. M. (2011). Minimization of focused ion beam damage in nanostructured polymer thin films. *Ultramicroscopy*, **111**, p. 191-199.

[97] Volkert, C.A., & Minor, A.M. (May 2007). Focused ion beam microscopy and micromachining. *MRS Bulletin*, **32**, p. 389-399.

[98] Battaini, M. (2008). Deformation behabious, and twinning mechanisms of commercially pure titanium alloys. (*Doctoral dissertation*). p. 4-5.

[99] Cullity, B. D. (1978). Elements of X-Ray Diffraction, Second Edition, Reading, Massachusetts: Addison-Wesley Publishing Company, Inc. p. 501-503.

[100] Partridge, P. G. (1967). The crystallography and deformation modes of hexagonal close-packed metals. *Met. Rev.,* **12**, p. 169-194.

[101] Yoo, M. H. (1981). Slip, twinning and fracture in hexagonal close-packed metals. *Metall. Mater. Trans. A*,**12A**, p. 409-418.

[102] Yu, Q. (2012). Size-related mechanical properties of pure magnesium. (*Doctoral dissertation*).

[103] Sands, D. E. (1975). *Introduction to Crystallography*. Mineola, NY: Dover Publications, Inc. p. 129-135.

[104] Asta, M. "The Face-Centered Cubic (fcc) and Hexagonal Close-Packed (hcp) Structures." MSE 200A, UC Berkeley, Fall 2012.

[105] Vitek, V. & Igarashi, M. (1991). Core structure of 1/3<11$\bar{2}$0> screw dislocations on basal and prismatic planes in h.c.p. metals: an atomistic study. *Philos. Mag. A*, **63**(5), p. 1059-1075.

[106] Yoo, M. H., Morris, J. R., Ho, K. M. & Agnew, S. R. (2002). Nonbasal deformation modes of HCP metals and alloys: role of dislocation source and mobility. *Metall. Mater. Trans. A,* **33A**, p. 813-822.

[107] Legrand, P.B. (1984). *Philos. Mag. B*, **49**, p. 171.

[108] Legrand, P. B. (1984). In P. Veyssiere, L. P. Kubin & J. Castaing (Eds.), *Dislocations*, Editions C.N.R.S., (p. 73-92). Paris, France.

[109] Numakura, H., Minonishi, Y. & Koiwa, M. (1986). *Scripta Metall*., **20**, p. 1581-1586.

[110] Minonishi, Y., Morozumi, S. & Yoshinaga, H. (1982). *Scripta Metall*., **16**, p. 427-430.

[111] Minonishi, Y., Morozumi, S. & Yoshinaga, H. (1985). *Scripta Metall*., **19**, p. 1241-1245.

[112] Minonishi, Y., Ishioka, S., Koiwa, M. & Morozumi, S. (1981). The core structure of a 1/3<$\bar{1}\bar{1}$23> screw dislocation in h.c.p. metals. *Philos. Mag. A*, **44**(6), p. 1225-1237.

[113] Minonishi, Y., Ishioka, S., Koiwa, M. & Morozumi, S. (1982). Motion of a 1/3<$\bar{1}\bar{1}$23>{11$\bar{2}$2} edge dislocation under applied shear stresses in an h.c.p. model crystal. *Philos. Mag. A*, **45**(5), p. 835-850.

[114] Minonishi, Y., Ishioka, S., Koiwa, M. & Morozumi, S. (1982). The core structures of a 1/3<$\bar{1}\bar{1}$23> screw dislocation in a model h.c.p. lattice. *Philos. Mag. A*, **46**(5), p. 761-770.

[115] Agnew, S. R. & Duygulu, O. (2005). Plastic anisotropy and the role of non-basal slip in magnesium alloy AZ31. *Inter. J. Plasticity*, **21**, p. 1161.

[116] Morozumi, S., Kikuchi, M. & Yoshinaga, H. (1976). Electron microscope observation in and around f11 0 2g twins in magnesium. *Trans. JIM*, **17**, p. 158.

Appendix A
Background on HCP Dislocations & Crystallography

A.1. HCP Crystallography

The FCC and HCP arrangement of atoms are the two most densely close-packed crystal structures adopted by pure elemental metals. Both structures have a 0.7405 atomic packing factor and coordination number of twelve, and differ only in the stacking sequence of the close packed plane (see Figure A.1). Consider a two close-packed layers of hard spheres stacked together. The second/upper layer spheres, layer B, will fit above some of the interstices of the first/lower layer, layer A. The third layer can either be identical to the first layer, layer A, or fit above the other first layer interstices not occupied by the second layer, layer C. As a result HCP and FCC structures have the stacking sequence ABABAB and ABCABC respectively.

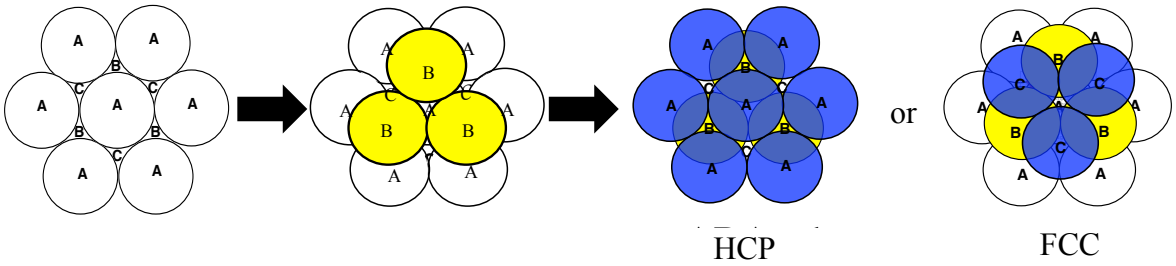

Figure A.1: Difference in stacking sequence for the HCP and FCC phases [104].

Hexagonal crystal lattices are generally defined with a four-axis system, known as the Miller-Bravais notation. Similar rules apply as in the cubic case (**x**, **y**, and **z**), but the coordinate axes are defined as the three independent hexagonal basal directions, $\mathbf{a}_1$, $\mathbf{a}_2$, $\mathbf{a}_3$, (instead of **x** and **y**) and the vertical prism direction, **c** (instead of **z**). Planes are represented by the indices, (*hkil*), where *i* is a redundant index and equals $-(h + k)$. Similarly, HCP directions are indicated by [*uvtw*], where *t* is the redundant index and equals $-(u + v)$. The Miller indices for planes and directions in cubic lattices are represented as (HKL) and [UVW], respectively. Below are some useful equations for hexagonal systems.

The conversion of a plane (*hkil*) to a direction representing the plane normal, [*uvtw*] [98].

$$[uvtw] = [hki\left(\frac{c^2}{a^2}\right)l] \tag{A.1}$$

Interplanar spacing, d_{hkil}, for HCP lattices [99].

$$\frac{1}{d_{hkil}^2} = \frac{4}{3}\left(\frac{h^2 + hk + k^2}{a}\right) + \frac{l^2}{c^2} \tag{A.2}$$

The conversion of three-index notation [UVW] to four-index notation [*uvtw*] [98].

$$[u,t,v,w] = [\frac{1}{3}(2\mathrm{U} - \mathrm{V}), \frac{1}{3}(2\mathrm{V} - \mathrm{U}), -(u+v), \mathrm{W}] \tag{A.3}$$

The conversion of four-index notation, [*uvtw*], to three-index notation, [UVW] [98].

$$[\mathrm{U},\mathrm{V},\mathrm{W}] = [(2u+v),(u+2v),w] \tag{A.4}$$

The angle, φ, between two HCP planes, $(h_1k_1i_1l_1)$ and $(h_2k_2i_2l_2)$ [99].

$$\cos\varphi = \frac{h_1h_2 + k_1k_2 + \frac{1}{2}(h_1k_2+h_2k_1) + \frac{3a^2}{4c^2}l_1l_2}{\sqrt{(h_1^2 + k_1^2 + h_1k_1 + \frac{3a^2}{4c^2}l_1^2)(h_2^2 + k_2^2 + h_2k_2 + \frac{3a^2}{4c^2}l_2^2)}} \tag{A.5}$$

The angle, ψ, between two HCP directions, $[u_1v_1t_1w_1]$ and $[u_2v_2t_2w_2]$ [99].

$$\cos\psi = \frac{u_1u_2 + v_1v_2 - \frac{1}{2}(u_1v_2 + v_1u_2) + \frac{c^2}{a^2}w_1w_2}{\sqrt{(u_1^2 + v_1^2 - u_1v_1 + \frac{c^2}{a^2}w_1^2)(u_2^2 + v_2^2 - u_2v_2 + \frac{c^2}{a^2}w_2^2)}} \tag{A.6}$$

For the HCP crystal structure, the most densely packed lattice planes (in order) are the basal plane, (0001), the three prism planes, $\{01\bar{1}0\}$, and the six pyramidal planes, $\{01\bar{1}1\}$ [1]. The close-packed directions are the $\langle 11\bar{2}0\rangle$, which are also the three $\mathbf{a}_1$, $\mathbf{a}_2$, and $\mathbf{a}_3$ axes of the hexagonal unit cell. The magnitude of these translation vectors, i.e. the shortest distance between two atom centers in a close-packed plane, is $(a/3)\langle 11\bar{2}0\rangle$ [1]. Figure A.2(a), shows the atom positions in the general HCP unit cell, and Figure A.2(b), shows the pure Ti HCP unit cell with the densely packed lattice planes and lattice parameters. For clarification, the (0001) and (0002) planes are both considered to be the "basal" plane in HCP materials. Some authors refer to the (0002) plane as the basal plane because the (0001) reflection is forbidden in HCP diffraction patterns.

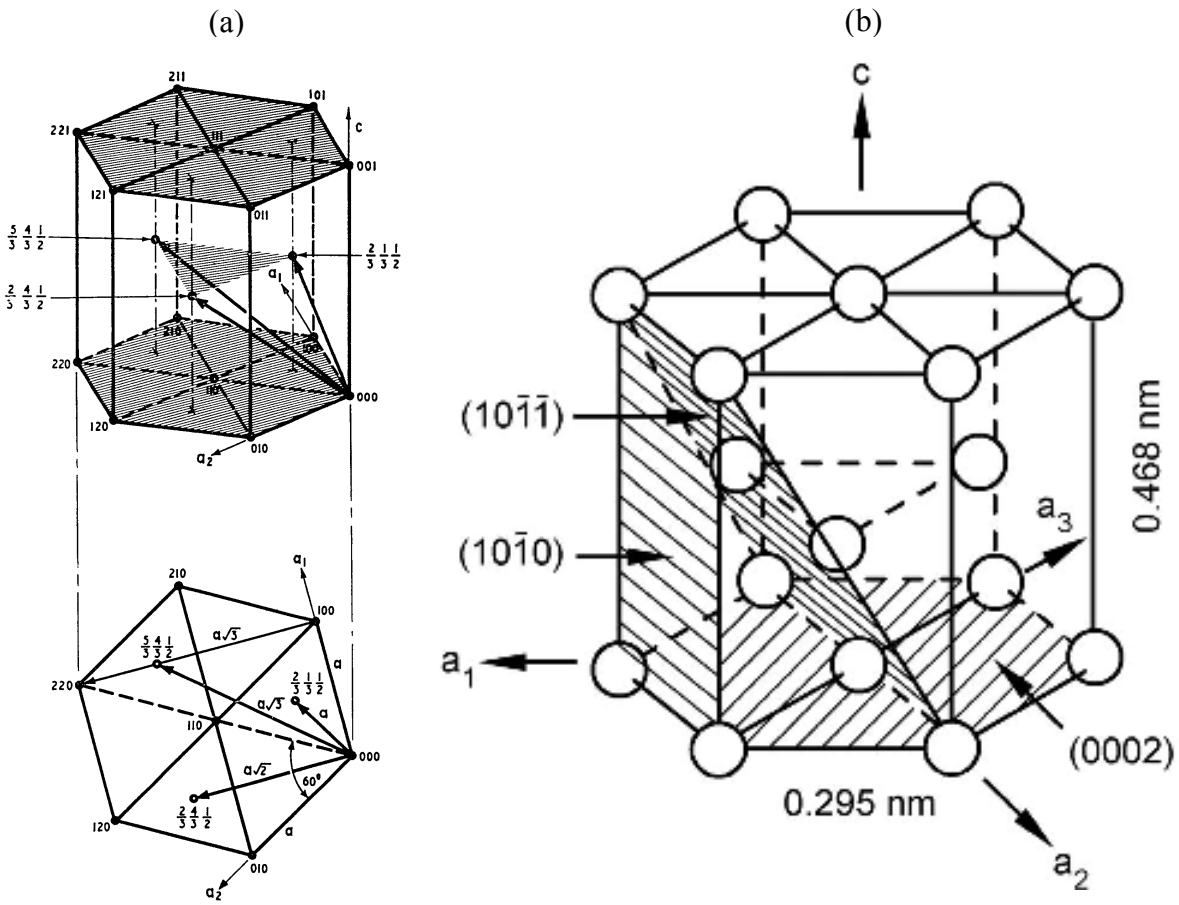

Figure A.2: (a) Atom positions [100] and (b) important slip planes [1] and in the HCP unit cell.

Ti, Zr, Mg, and Be all have stable HCP crystal structures at lower temperatures, known as the α-phase, and at higher temperatures, Ti, Zr, and Be undergo a phase transformation to a BCC crystal structure, β-phase. Mg retains its HCP structure until its melting temperature. The c/a ratios for these materials are all smaller than the ideal ratio of 1.633 for HCP materials [1].

Table A.1: Structural and physical properties of a few pure HCP metals [1,93,99–102].

	Ti	**Zr**	**Mg**	**Be**
Atomic Number	22	40	12	4
Electron Configuration	[Ar]3$d^2$4s^2	[Kr]5$s^2$4d^2	[Ne]3s^2	[He]2s^2
Melting Temperature (°C)	1670	1855	632	1287
α(HCP)→β(BCC) Transition (°C)	882°C	863°C	-	1250°C
Solid Density (g/cm^3)	4.54	6.45	1.74	1.85
Lattice Parameter "a" (Å)	2.950	3.231	3.203	2.281
Lattice Parameter "c" (Å)	4.683	5.147	5.200	3.576
c/a Ratio	1.587	1.593	1.623	1.568
Atomic Radius (Å)	1.475	1.616	1.602	1.141

The HCP unit cell is not a primitive unit cell, and the red lines in Figure A.3 indicate the primitive trigonal unit cell within the hexagonal cell, where a = b ≠ c, α = β = 90°, and γ = 120° [103].

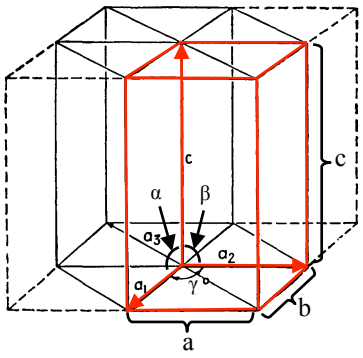

Figure A.3: Primitive trigonal unit cell (in red) within the non-primitive hexagonal unit cell [100].

There are six atoms within the HCP unit cell and only two in the primitive trigonal. Octahedral voids are defined as sites that are equidistant from six atoms. All of which are found on C layer sites in the HCP crystal structure. Tetrahedral voids are equidistant from four atoms and are located above and below each atom. There are two octahedral sites, (⅓,⅔,¼), (⅓,⅔,¾), and four tetrahedral sites, (⅔,⅓,⅛), (⅔,⅛,⅞), (0,0,⅜), and (0,0,⅝), in the primitive cell [94]. Resulting in one octahedral void per atom and two tetrahedral voids per atom.

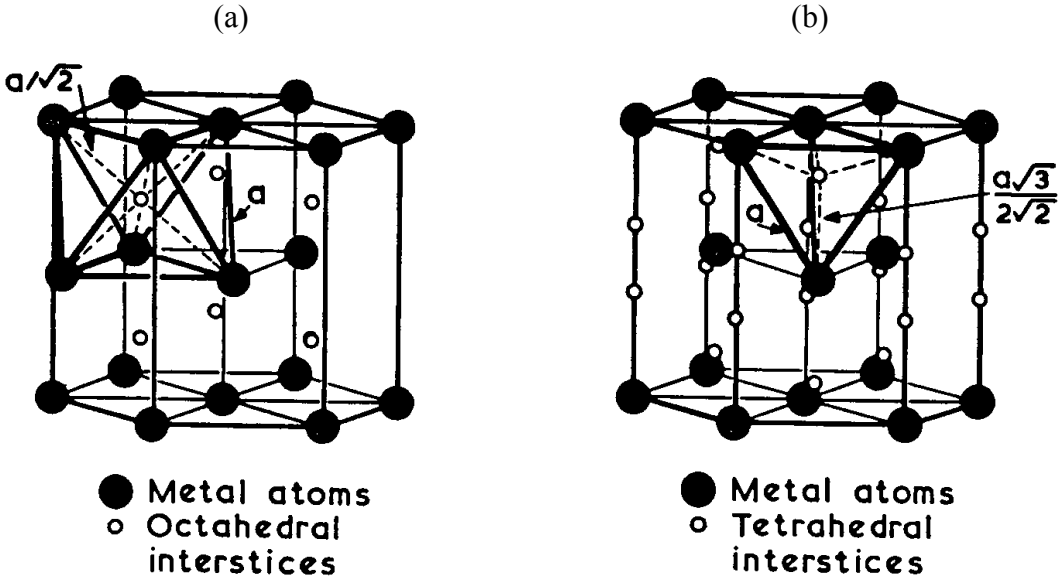

Figure A.4: Octahedral and Tetrahedral positions within the HCP unit cell [100].

Table A.2: Octahedral and tetrahedral hole sizes for a few pure HCP metals [94].

	Octahedral Hole Radius (Å)	**Tetrahedral Hole Radius (Å)**
Ti	0.611	0.331
Zr	0.669	0.363
Mg	0.663	0.360
Be	0.472	0.256

The octahedral voids in the HCP structure are larger than the tetrahedral voids, and as a result, interstitial solutes tend to reside in octahedral sites. Interstitial solutes in octahedral positions are considered to be α-phase stabilizers. However, the small size of hydrogen also allows it to fit nicely in the tetrahedral voids of BCC β-Ti, which could explain why hydrogen is a β-phase stabilizer for Ti [94].

Table A.3: Neutral atomic radii for a few interstitial solute species [94].

Neutral Atomic Radius of Interstitial Species (Å)	
Oxygen	0.60
Nitrogen	0.71
Carbon	0.77
Hydrogen	0.46

It is no surprise that octahedral interstitials alter the lattice parameters. In fact, both **a** and **c** increase, though the interstitial effect on **c** is greater. Therefore the c/a ratio generally increases with increasing interstitial content [94]. The lattice strain induced by interstitials will interact with strain fields associated with dislocations, thereby altering the dislocation-mediated deformation mechanisms observed in commercially pure HCP metals.

A.2. Dislocations in HCP Metals

There are three families of slip directions and five possible slip plane families for perfect dislocations in HCP metals. $\vec{\mathbf{a}}$ type dislocations have a Burgers vector of $(a/3)\langle 11\bar{2}0\rangle$ and can slip on the basal, (0001), first order prism, $\{01\bar{1}0\}$, and first order pyramidal, $\{01\bar{1}1\}$, planes. It is the consensus that $\vec{\mathbf{a}}$ type slip plays the most important role in the plastic deformation of HCP metals [105]. $\vec{\mathbf{c}}+\vec{\mathbf{a}}$ type dislocations have a Burgers vector of $(a/3)\langle 11\bar{2}3\rangle$ and tend to slip on the first $\{01\bar{1}1\}$ and second $\{11\bar{2}2\}$ order pyramidal planes. It is possible for these dislocations to lie in the $\{01\bar{1}0\}$ planes, though the energy required for slip is quite high. The $\vec{\mathbf{c}}+\vec{\mathbf{a}}$ Burgers vector is simply the sum of the $\vec{\mathbf{c}}$ and $\vec{\mathbf{a}}$ Burgers vectors, $(a/3)\langle 11\bar{2}(3c/a)\rangle=(c)[0001]+(a/3)\langle 11\bar{2}0\rangle$. As indicated in Table A.4, the number of $\vec{\mathbf{c}}+\vec{\mathbf{a}}$ independent slip systems is unclear since an independent slip system must generate from an independent source. There is no definitive experimental evidence on $\vec{\mathbf{c}}+\vec{\mathbf{a}}$ dislocation source mechanisms [106]. Finally, $\vec{\mathbf{c}}$ type dislocations have a Burgers vector of $(c)[0001]$ and can slip on the first $\{01\bar{1}0\}$ and second $\{11\bar{2}0\}$ order prism planes. $\vec{\mathbf{c}}$ type dislocations are essentially sessile, they do not glide, since the required activation energy for slip is very large.

Table 4: Possible slip systems for perfect dislocations in an HCP lattice [100].

Slip System	Burgers Vector Type	Burgers Vector / Slip Direction	Slip Plane		Number of Slip Systems	
					Total	Independent
1	$\vec{a}$	⅓<11$\bar{2}$0>	Basal	(0001)	3	2
2	$\vec{a}$	⅓<11$\bar{2}$0>	1st order prism	{10$\bar{1}$0}	3	2
3	$\vec{a}$	⅓<11$\bar{2}$0>	1st order pyramidal	{10$\bar{1}$1}	6	4
4	$\vec{c}+\vec{a}$	⅓<11$\bar{2}$3>	1st order pyramidal	{10$\bar{1}$1}	6	?
5	$\vec{c}+\vec{a}$	⅓<11$\bar{2}$3>	2nd order pyramidal	{11$\bar{2}$2}	6	?
6	$\vec{c}$	<0001>	1st order prism	{10$\bar{1}$0}	3	2
7	$\vec{c}$	<0001>	2nd order prism	{11$\bar{2}$0}	3	2

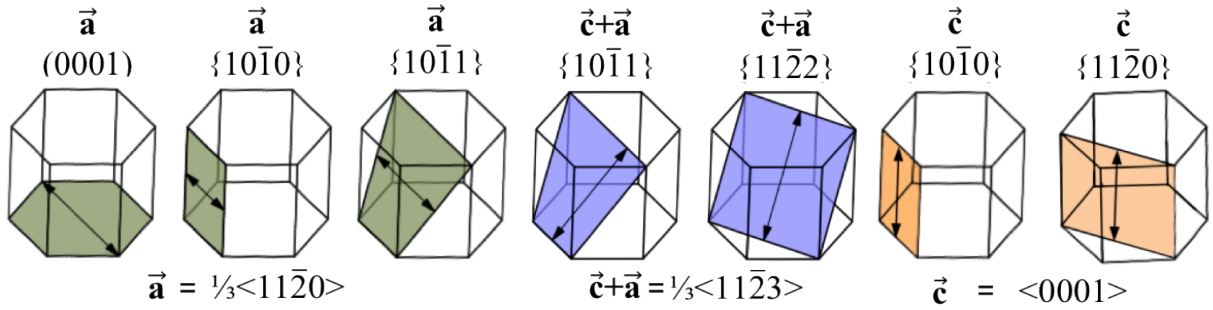

Figure A.10: Visual representation of the possible slip systems for perfect dislocations in an HCP lattice [98].

A.2.1. $\vec{a}$ Type Dislocation Slip and Dissociations in HCP Metals

Since the basal plane is the most close-packed plane in HCP materials dislocations on prism planes cannot spread their cores as much as dislocations on basal planes, it would appear as if $\vec{a}$ type basal slip is the most preferred slip system. However, this is not the case for Ti and Zr. In fact, several computational studies have shown that the narrow core on the prism plane is actually more energetically favorable than a dissociated core on the basal plane for these metals [86].

According to the PN-model, the larger the dislocation core, the lower the PN-stress required for dislocation slip. Therefore, the probable $\vec{a}$ type dissociations for a given HCP metal will help explain why some HCP metals prefer $\vec{a}$ type prism slip to $\vec{a}$ type basal slip. A perfect ⅓<11$\bar{2}$0> dislocation dissociating into Shockley partials can produce one of three kinds of basal stacking faults.

$$\frac{1}{3}[11\bar{2}0] \rightarrow \frac{1}{3}[10\bar{1}0] + \frac{1}{3}[01\bar{1}0] \tag{A.7}$$

The resulting faults are either intrinsic (I_1 or I_2) or extrinsic (E), all of which introduce a thin layer of FCC stacking (ABC) and have characteristic stacking-fault energies, γ_{I1}, γ_{I2}, γ_E [86]. I_1 is formed when a basal layer is removed, which produces a very high-energy fault. This energy is

reduced when a ⅓<10$\bar{1}$0> partial dislocation slips above the fault. I_2 forms by ⅓<10$\bar{1}$0> slip on the basal plane in a perfect crystal, and E is produced by inserting a basal plane [86].

ABABABABAB… → ABAB**B**ABAB… → AB**ABC**BCB… (I_1)
ABABABABAB… → AB**ABC**ACAC… (I_2)
ABABABABAB… → AB**ABC**ABAB… (E)

The stacking fault energy is primarily determined by changes in the second-neighbor sequence. There is only one change in I_1, where former A layers become C layers, two changes in I_2, A to C and B to A, and three changes in E, A to C to B and B to A. Therefore, E should have the highest γ since it causes the most changes in the stacking sequence. To a first approximation, $\gamma_E \approx 1.5\gamma_{I2} \approx 3\gamma_{I1}$ [86].

Stacking faults can also form when vacancies accumulate in a basal plane, assumed in an A layer. As a consequence, two B layers will come into contact, forming a very unstable stacking sequence surrounded by a ½[0001] partial loop. This high-energy situation is avoided by forming sessile Frank loops bounding a stacking fault, depicted in Figure A.11. Two mechanisms are possible. In the first situation, an adjacent B layer can move into C positions, forming the extrinsic stacking fault E. This is the same as two ⅓<10$\bar{1}$0> Shockley partials of opposite signs gliding above and below the missing A layer, resulting in a sessile Frank ½[0001] partial surrounding the extrinsic stacking fault [86].

$$\frac{1}{2}[0001] + \frac{1}{3}[1\bar{1}00] + \frac{1}{3}[\bar{1}100] \rightarrow \frac{1}{2}[0001] \tag{A.8}$$

The second mechanism is the same as the I_1 stacking fault formation. A single ⅓<10$\bar{1}$0> Shockley partial glides above the missing A layer, shifting B atoms to C sites, and A atoms to B sites. This creates the low-energy intrinsic stacking fault I_1 encircled by a ⅙<$\bar{2}$203> sessile Frank partial [86]. This type of sessile Frank loop is more likely to occur since γ_E is approximately three times larger than γ_{I1}, and E-type loops can transform into the I_1-type loops with the same equation A.9 reaction.

$$\frac{1}{3}[\bar{1}100] + \frac{1}{2}[0001] \rightarrow \frac{1}{6}[\bar{2}203] \tag{A.9}$$

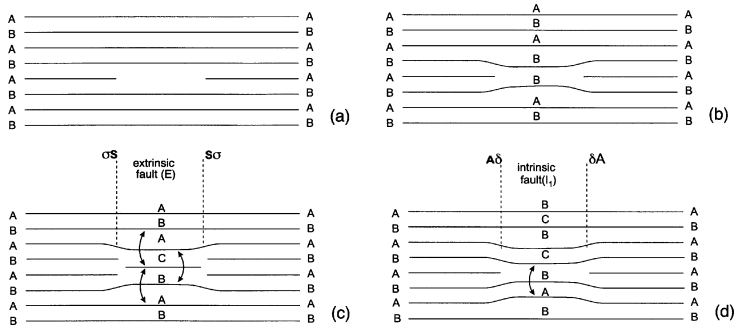

Figure 5.8: Formation of Frank sessile dislocation loops as a consequence of vacancy clustering [86].

There is no experimental evidence of stacking faults in HCP metals on non-basal, non-close packed, planes. However, using computational modeling, it has been hypothesized that stable stacking faults may exist on the $\{10\bar{1}0\}$, $\{11\bar{2}2\}$, and $\{10\bar{1}1\}$ planes [86]. According to Vitek *et. al*. (1991) [105], metastable faults due to $\vec{\mathbf{a}}$ type dissociations could form on the basal or prism planes. Which plane the dissociation occurs on depends on the ratio of prism and basal stacking fault energies (γ_p / γ_b) and the magnitude of **b** for the prism partials that are perpendicular to the $\vec{\mathbf{a}}$ direction ($b^p_{\perp \mathbf{a}}$). This turns out to be the edge component of the partials for an $\vec{\mathbf{a}}$ type screw dislocation dissociation. The edge component on the basal plane is fixed and equal to $1/6<0\bar{1}10>$, but the prism plane edge component is (x/6)[0001], where x varies for each HCP metal and decreases with decreasing c/a ratio. Given the same stacking fault energy, the energy gained by dissociation increases as $b^p_{\perp \mathbf{a}}$ decreases. Therefore prism splitting could be favorable even if $\gamma_p > \gamma_b$ [105]. The following $\vec{\mathbf{a}}$ type prism dissociation was proposed by Vitek *et. al.* (1991):

$$\tfrac{1}{3}<11\bar{2}0> = \tfrac{1}{6}<11\bar{2}x> + \tfrac{1}{6}<11\bar{2}\bar{x}> \tag{A.10}$$

Conrad (1981) [94] also presents some possible dislocation dissociations that form stacking faults to account for $\vec{\mathbf{a}}$ type prism slip in Ti and Zr. $\{10\bar{1}0\}$ $\tfrac{1}{3}<11\bar{2}0>$ screw dislocations may dissociate into three partials, D_1, D_2, and D_3, simultaneously on the $\{10\bar{1}0\}$ and (0001) planes by the following reactions [94]:

$$\mathbf{b} = \tfrac{1}{3}<11\bar{2}0> \rightarrow \mathbf{b}/3 + (\mathbf{b}/6 + \mathbf{H}) + (\mathbf{b}/2 - \mathbf{H}) \tag{A.11}$$

$$\mathbf{b} = \tfrac{1}{3}<11\bar{2}0> \rightarrow \mathbf{b}/3 + (\mathbf{b}/2 + \mathbf{H'}) + (\mathbf{b}/6 - \mathbf{H'}) \tag{A.12}$$

or on the $\{10\bar{1}0\}$ and $\{10\bar{1}1\}$ planes by the reaction:

$$\mathbf{b} = \tfrac{1}{3}<11\bar{2}0> \rightarrow \mathbf{b}/3 + (\mathbf{b}/2 + \mathbf{H''}) + (\mathbf{b}/6 - \mathbf{H''}) \tag{A.13}$$

Where **H**, **H'**, and **H"** are Burgers vectors of the edge components of the partials. **H** and **H'** lie in the (0001) plane and **H"** lies in the $\{10\bar{1}1\}$ planes [94]. Illustrated in Figure A.12, D_1 has Burgers vector **b**/3 and is situation on the $\{10\bar{1}0\}$ plane, D_2 lies at the intersection of either the $\{10\bar{1}0\}$ and (0001) or $\{10\bar{1}0\}$ and $\{10\bar{1}1\}$ planes, and D_3 has the opposite edge component of D_2 and resides in (0001) or $\{10\bar{1}1\}$ planes.

(a) (b) (c)

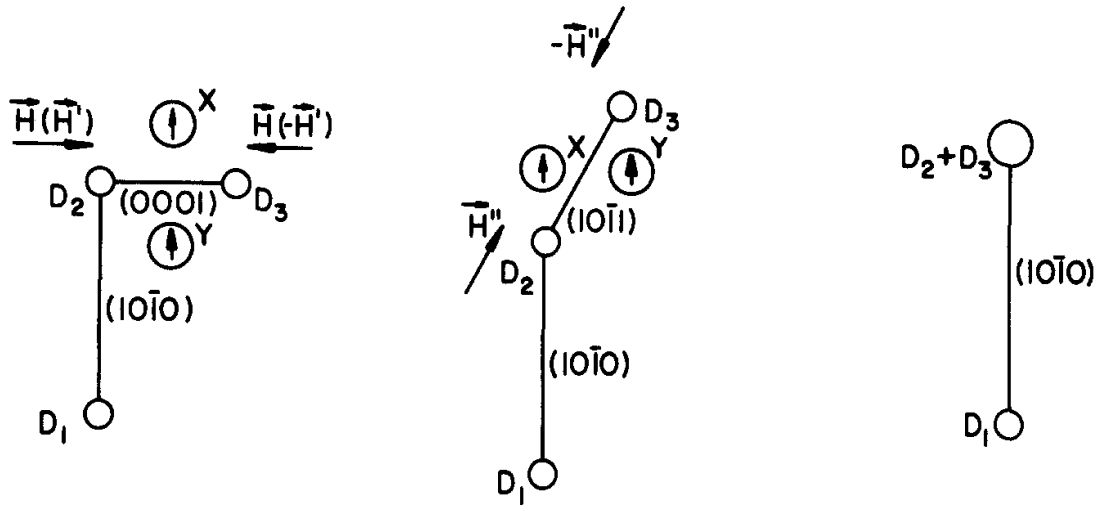

Figure A.12: (a) Sessile dissociation on the {10$\bar{1}$0} and (0001) planes, (b) sessile dissociation on the {10$\bar{1}$0} and {10$\bar{1}$1} planes, (c) glissile splitting on the {10$\bar{1}$0} planes. X and Y refer to interstitial atoms preventing a sessile-to-glissile transformation shown in c, discussed in more detail later [94].

The stacking fault between D_1 and D_2 have a similar {112} plane stacking sequence as seen in BCC metals, and is only relevant since BCC is the stable crystal structure for Ti and Zr at high temperatures [86]. The basal stacking fault produced between D_2 and D_3, shown in Figure A.12(a), is the standard I_1 fault found in other HCP metals. Before further slip can occur, the sessile partials must recombine into a glissile configuration, Figure A.12(c) according to the reaction:

$$\mathbf{b} \rightarrow \mathbf{b}/3 + 2\mathbf{b}/3 \qquad \text{(A.14)}$$

Atomistic and experimental studies both agree that basal splitting is strongly favored over prism splitting in Mg. This is primarily due to the prism fault energy being much larger than the basal, $\gamma_p >> \gamma_b$. Additionally, the required critical resolved shear stress, τ_{CRSS}, for non-basal slip is one to two orders of magnitude higher than basal slip [86]. Partials on the prism plane are believed to have comparable energies to $\vec{\mathbf{c}}+\vec{\mathbf{a}}$ type dislocations (104). If basal slip is not possible due to an **a** loading axis, prism and pyramidal slip will occur equally frequently.

Vitek *et. al*. (1991) suggests that $\vec{\mathbf{a}}$ type prism splitting is favorable for Be since the partials have no components parallel to the [0001] direction (104). However, this does not agree with experimental observations, and like Mg, Be has a very high τ_{CRSS} for non-basal slip [86]. It is hypothesized that the electronic structure of Be could lower the basal stacking fault energy when considered.

For Ti and Zr, the τ_{CRSS} for basal slip ($\approx$100 MNm^{-2}) is expected to be larger than the τ_{CRSS} for prism slip ($\geq$10 MNm^{-2}) [86]. This suggests that the basal stacking fault energy is quite large in these metals. For pure Ti, prism splitting was concluded to be favorable since the calculated $b^{p}_{\perp \mathbf{a}}$ was much smaller for prism splitting than basal [105]. Additionally, $\gamma_p < \gamma_b$ according Legrand *et. al.* (1984) [107–108]. It is generally believed that interatomic forces hinder basal stacking fault formation, which prevents reaction A.7 from occurring [86]. Regardless, for $\vec{\mathbf{a}}$ type dislocations in Ti, prism slip and splitting is most favorable, followed by basal slip.

A.2.2. $\vec{c}+\vec{a}$ Type Dislocation Slip and Dissociations in HCP Metals

The Von Mises criterion requires that each grain in a polycrystalline metal have five independent slip systems to accommodate the shape changes imposed by neighboring grains during plastic deformation [86]. $\vec{\mathbf{a}}$ type basal and prism slip only provide two independent each, making secondary deformation modes, such as deformation twinning and/or $\vec{\mathbf{c}}+\vec{\mathbf{a}}$ slip along the pyramidal planes, critical for HCP ductility. $\vec{\mathbf{c}}+\vec{\mathbf{a}}$ slip is especially important since it can induce strain along both the **a** and **c** HCP axes, and may contribute more independent slip systems [94]. It is unclear exactly how many independent slip systems $\vec{\mathbf{c}}+\vec{\mathbf{a}}$ type pyramidal slip contributes since an independent slip system must have its own independent dislocation source [100]. When an HCP metal is compressed or pulled along the c axis, only $\vec{\mathbf{c}}+\vec{\mathbf{a}}$ type dislocations are active because the Schmidt factor for both $\vec{\mathbf{a}}$ and $\vec{\mathbf{c}}$ type dislocations are zero. Additionally, the $\{10\bar{1}0\}$ and (0001) glide planes cannot be activated as they are parallel and perpendicular to the stress axis respectfully. $\vec{\mathbf{c}}+\vec{\mathbf{a}}$ dislocation slip along the $\{11\bar{2}2\}$ planes is most likely since it results in a higher Schmidt factor than the $\{10\bar{1}1\}$ planes [1]. However, there is debate on whether the critical resolved shear stress for $\vec{\mathbf{c}}+\vec{\mathbf{a}}$ slip is primarily dependent on dislocation mobility or on the source mechanism for generating $\vec{\mathbf{c}}+\vec{\mathbf{a}}$ dislocations [106].

Grain boundaries are potential $\vec{\mathbf{c}}+\vec{\mathbf{a}}$ $\{10\bar{1}1\}$ slip initiation sites. The screw segments of the dislocation, having higher mobility, were able to cross slip from one $\{10\bar{1}1\}$ plane to another, which allowed for successive $\vec{\mathbf{c}}+\vec{\mathbf{a}}$ to nucleate [106, 109]. Though it is unclear on whether this source produces a perfect $\vec{\mathbf{c}}+\vec{\mathbf{a}}$ dislocation, or a partial dislocations separated by a stacking fault. Several TEM studies support $\vec{\mathbf{c}}+\vec{\mathbf{a}}$ dislocation generation at twin boundaries. Minonishi *et al.* (1982, 1985) effectively showed that in Ti, $\vec{\mathbf{c}}+\vec{\mathbf{a}}$ generation occurs at both $\{10\bar{1}1\}$ and $\{11\bar{2}2\}$ incoherent twin boundaries [110–111]. Interestingly, $\vec{\mathbf{c}}+\vec{\mathbf{a}}$ dislocations are not typically found without nearby $\vec{\mathbf{a}}$ and $\vec{\mathbf{c}}$ dislocations. This suggests that a possible source mechanism for $\vec{\mathbf{c}}+\vec{\mathbf{a}}$ dislocations is an interaction between $\vec{\mathbf{a}}$ and $\vec{\mathbf{c}}$ dislocations. It is proposed that a glissile $\vec{\mathbf{a}}$ dislocation could combine with a sessile $\vec{\mathbf{c}}$ dislocation to create a $\vec{\mathbf{c}}+\vec{\mathbf{a}}$ dislocation on a prism plane. $\vec{\mathbf{c}}+\vec{\mathbf{a}}$ dislocations can technically exist on prism planes, though they are likely to cross slip onto a pyramidal plane due to the high energy barrier for $\vec{\mathbf{c}}+\vec{\mathbf{a}}$ prism glide [106]. The point of cross slip, intersection of two planes, can be thought of as "pinning" points for the glissile portion of the $\vec{\mathbf{c}}+\vec{\mathbf{a}}$ dislocation on the pyramidal plane. Generating an effective "Frank-Reed source," common to FCC metals. This source mechanism is feasible for all HCP metals. Forming attractive junctions between $\vec{\mathbf{a}}$ and $\vec{\mathbf{c}}$ dislocations on the prism plane is energetically favorable for HCP metals that have a preference for $\vec{\mathbf{a}}$ type prism slip, i.e. Ti and Zr. For Mg and Be, preferential $\vec{\mathbf{a}}$ type basal slip, the basal $\vec{\mathbf{a}}$ dislocation must first cross slip onto the prism plane. This reasonably suggests that the attractive forces between basal $\vec{\mathbf{a}}$ and prism $\vec{\mathbf{c}}$ dislocations is large enough to pull the $\vec{\mathbf{a}}$ dislocation out of the basal plane [106]. $\vec{\mathbf{c}}+\vec{\mathbf{a}}$ dislocations may

decompose back into separate $\vec{\mathbf{c}}$ and $\vec{\mathbf{a}}$ dislocations for Mg, but this is energetically unfavorable in Be [102, 106]. Since this source mechanism requires $\vec{\mathbf{a}}$ and $\vec{\mathbf{c}}$ dislocation interactions and subsequent cross-slip, $\vec{\mathbf{c}}+\vec{\mathbf{a}}$ dislocations generated this way would not contribute any new independent slip systems. This may support why deformation twinning and $\vec{\mathbf{c}}+\vec{\mathbf{a}}$ are often observed simultaneously for c-axis loading.

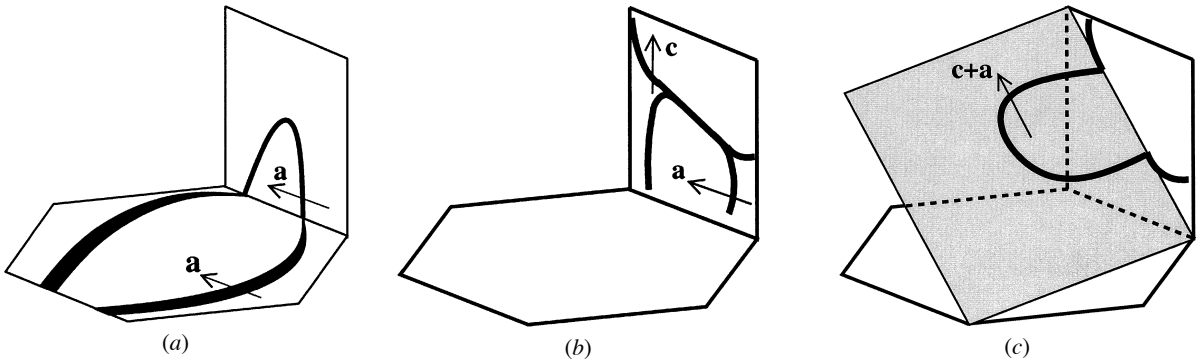

Figure A.13: $\vec{\mathbf{c}}+\vec{\mathbf{a}}$ dislocation source mechanism. (a) $\vec{\mathbf{a}}$ cross slip to (0001), (b) formation of $\vec{\mathbf{c}}+\vec{\mathbf{a}}$ attractive junction, and (c) $\vec{\mathbf{c}}+\vec{\mathbf{a}}$ cross slip to pyramidal plane [106].

There is little experimental data on the $\vec{\mathbf{c}}+\vec{\mathbf{a}}$ core structure and mobility. Using a Lennard-Jones 12:6 potential, Minoishi *et. al.* (1981, 1982) found that ⅓<11$\bar{2}$3> edge dislocations glide on {11$\bar{2}$2} planes for both c-axis tension and compression. However, ⅓<11$\bar{2}$3> screw dislocations in Ti were found to glide on {11$\bar{2}$2} planes for c-axis compression and on {10$\bar{1}$1} planes for c-axis tension [112–114, 98]. This is likely due to the relative ease of cross slip for screw dislocations as compared to edge dislocations. It has been observed that the screw components of perfect $\vec{\mathbf{c}}+\vec{\mathbf{a}}$ dislocations are stable, while the edge components are often unstable [106]. Therefore, $\vec{\mathbf{c}}+\vec{\mathbf{a}}$ edge dislocation cores tend to spread more than those with screw orientation. Additionally, the atomically rough pyramidal planes and large $\mathbf{b}$ = ⅓<11$\bar{2}$3> suggest that $\vec{\mathbf{c}}+\vec{\mathbf{a}}$ dislocations may dissociate into partials with nonplanar core structures [86]. Though planar dissociations are possible [106]. This edge instability and correlation between $\vec{\mathbf{c}}+\vec{\mathbf{a}}$ slip and deformation twinning has led to extensive computational studies on $\vec{\mathbf{c}}+\vec{\mathbf{a}}$ {11$\bar{2}$2} edge dislocations. The most basic $\vec{\mathbf{c}}+\vec{\mathbf{a}}$ edge dislocation dissociation on the {11$\bar{2}$2} plane is co-linear, and is given by the following reaction [102, 106]:

$$1/3[11\bar{2}3] \rightarrow \alpha\,/3[11\bar{2}3] + (1-\alpha)/3\,[11\bar{2}3] + SF(11\bar{2}\bar{2}) \qquad (A.15)$$

Where $\alpha \approx 0.5$ for a symmetric dissociation. This mechanism forms glissile partials separated by a stacking fault on the {11$\bar{2}$2} plane. This stacking fault has comparable energy to the {11$\bar{2}$2} twin boundary for Mg, Ti, and Zr [106]. Another theory suggests that $\vec{\mathbf{c}}+\vec{\mathbf{a}}$ edge dislocations, originally on the {11$\bar{2}$2} plane, undergo a nonplanar sessile dissociation, forming a {11$\bar{2}$1} twin embryo [106].

$$1/3[11\bar{2}3] \rightarrow 1/9[\bar{1}\bar{1}26] + 1/9[44\bar{8}3] \qquad (A.16)$$

The 1/9[44$\bar{8}$3] partial can dissociate even further to form a basal plane stacking fault associated with the 1/3[10$\bar{1}$0] partial, as shown in Figure A.14. Where $\mathbf{p}_1$ = 1/9[$\bar{1}\bar{1}$26], $\mathbf{p}_2$ = 1/9[14$\bar{5}$3], and $\mathbf{p}_3$ = 1/3[10$\bar{1}$0].

$$1/3[11\bar{2}3] \rightarrow 1/9[\bar{1}\bar{1}26] + 1/9[14\bar{5}3] + 1/3[10\bar{1}0] + SF(0001) \quad \text{(A.17)}$$

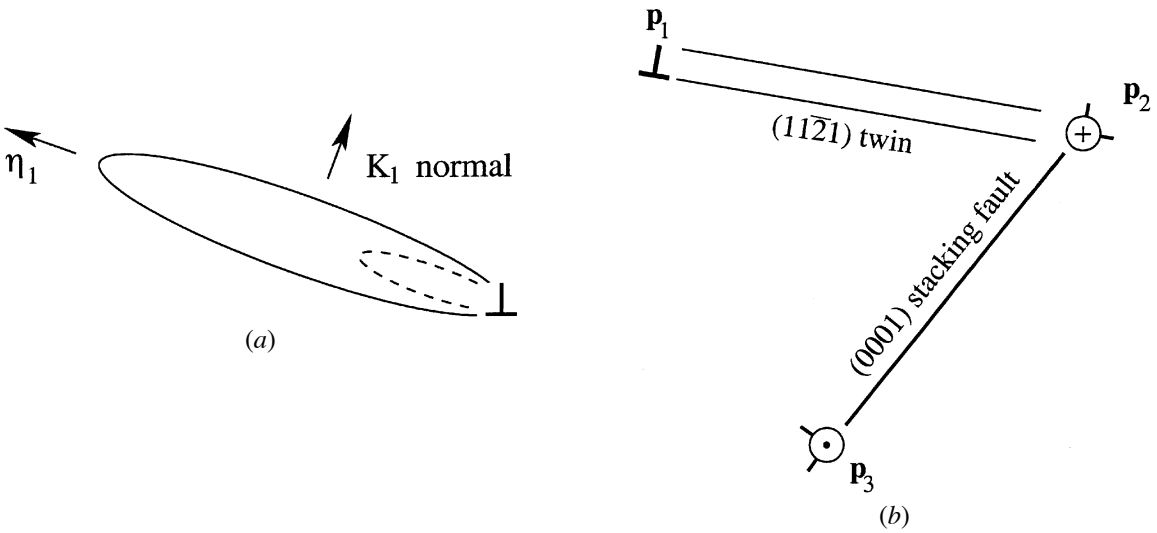

Figure A.14: Heterogeneous twin nucleation. (a) twin embryo, (b) twin generation due to nonplanar $\vec{\mathbf{c}}+\vec{\mathbf{a}}$ edge dissociation [106].

This sessile dissociation/twin nucleation mechanism corresponds to {11 $\bar{2}$ 1} twinning observations in Ti and Zr. However, it would not likely occur in Mg or Be since {11$\bar{2}$1} twins are not found in these materials. The coplanar dissociation associated with reaction A.15 supports the observed $\vec{\mathbf{c}}+\vec{\mathbf{a}}$ slip modes seen in Mg and Be [106].

According to atomistic simulations, $\vec{\mathbf{c}}+\vec{\mathbf{a}}$ screw dislocations can also dissociate according to reaction A.15 on the {11$\bar{2}$2} planes as well as the {10$\bar{1}$1} planes. This suggests that stable stacking faults may exist on the {10$\bar{1}$1} planes when $\alpha \leq 0.5$. Though additional work is needed since present calculations do not allow for complex atom rearrangements within the slip planes. The potential for $\vec{\mathbf{c}}+\vec{\mathbf{a}}$ screw dislocation core spreading on multiple slip planes indicate the likelihood of cross slip [106]. Cross slip is a thermally activated process, and if the proposed stacking faults on the {11$\bar{2}$2} and {10$\bar{1}$1} planes have comparable energies, then the preferential plane for $\vec{\mathbf{c}}+\vec{\mathbf{a}}$ dissociation may also have a strong temperature dependence. It would then be expected that non-basal $\vec{\mathbf{c}}+\vec{\mathbf{a}}$ slip modes are a function of temperature. It has been observed that $\vec{\mathbf{c}}+\vec{\mathbf{a}}$ slip can accommodate shear ahead of a propagating twin at low temperatures. As temperature is raised, $\vec{\mathbf{c}}+\vec{\mathbf{a}}$ slip becomes more abundant, particularly with c-axis compression [94].

A.2.3. $\vec{c}$ Type Dislocation Slip Systems in HCP Metals

The third slip vector, $\vec{\mathbf{c}}$, has a Burgers vector of [0001] and can theoretically glide along the $\{10\bar{1}0\}$ and $\{11\bar{2}0\}$ planes. However, the high general stacking fault energy required for $\vec{\mathbf{c}}$ dislocation slip essentially renders it sessile. Consequentially, experimental observations of prismatic $\vec{\mathbf{c}}$ slip are rare [101]. Conrad (1981) reports its occurrence in polycrystalline CP Ti at 475K [94]. Additionally, a large number of $\vec{\mathbf{c}}$ dislocations were observed in Mg around grain boundaries in studies conducted by Morozumi *et al*. (1976) [116], and Angew *et al*. (2005) [115].